Numerical Modeling of Degas in EV Battery Cooling Plates: A Multiphase CFD Study

Mattia Derobertis

Thermal Energy and Process Engineering, TEPE4-1001, 2025

Master Thesis

AAU Energy
Aalborg University
http://www.aau.dk

AALBORG UNIVERSITY
STUDENT REPORT

Title:
Numerical Modeling of Degas in EV Battery Cooling Plates: A Multiphase CFD Study

Theme:
Master Thesis

Project Period:
Spring 2025

Project Group:
TEPE4-1001

Participants:
Mattia Derobertis

Supervisors:
Anna Lyhne Jensen
Lu Naixian

Number of Pages: 72

Date of Completion:
May 28th - 2025

Abstract:

Efficient thermal management in electric vehicles (EVs) is critical to battery performance and safety. Liquid-cooled battery plates are commonly used, but the presence of trapped air bubbles during coolant filling can degrade heat transfer and lead to localized overheating. This study presents a numerical framework for simulating the degassing process in EV battery cooling plates using the Volume of Fluid (VOF) method in STAR-CCM+. The model is validated against experimental data with image-based bubble detection, resulting in a correlation of 75% in the number of bubbles and 99% of total remaining air in the system. A comparison of three turbulence models (URANS, LES, DES) showed consistent air entrapment predictions, with LES providing the highest resolution of turbulent structures. Additionally, velocity magnitude was identified as an effective single-phase indicator for predicting regions prone to air retention, reducing computational cost of more than 90% in early-stage design evaluation. Design modifications informed by simulation results demonstrated improved degassing performance. The proposed framework enables reliable analysis of air removal in battery cooling systems and supports the optimization of geometry without extensive physical testing.

Preface

The following thesis has been written by the 4th semester M.Sc. group, TEPE4-1001, at the Department of Energy of Aalborg University, as a master thesis in collaboration with Volvo Cars in Göteborg. The thesis has been supervised by Associate Professor, Anna Lyhne Jensen from Aalborg University and Senior CAE Engineer, Lu Naixian at Propulsion and Energy, Volvo Cars. A special thanks also goes to Test Engineer Håkan Nilsson at Volvo Cars for the support for the experimental part of this work, and the entirety of the battery thermal simulation team at Propulsion and Energy, Volvo Cars.

Reading Guide

The citations have been done using the APA method, where citations will be shown as Author(s) (year). The citations follow their references in the bibliography located at the end of the thesis. Chapters, sections, figures, tables and equations are labeled and these will also be referenced when mentioned in the text. The numbering of these labels is in chronological order and chapter-wise. Throughout the report, some symbols and abbreviations may have different subscripts, however, these differences can be found in the Nomenclature.

Mattia Derobertis
mderob23@student.aau.dk

Signature: 

Summary

The growing demand for sustainable transportation has led to a rapid increase in the adoption of electric vehicles (EVs). Ensuring the reliability, safety, and longevity of EV battery systems is critical to this transition, with thermal management playing a central role. Liquid-cooled battery plates are widely used in commercial EVs due to their high thermal performance. However, the presence of trapped air bubbles during the coolant filling process can lead to reduced heat transfer, temperature non-uniformities, and accelerated battery degradation. This thesis focuses on the simulation and analysis of the degassing process within EV battery cooling plates, aiming to provide a predictive and design-supportive computational framework.

The study employs the Volume of Fluid (VOF) method in STAR-CCM+ to model the multiphase flow of air and coolant during degassing. Several assumptions, including predefined initial air distributions, were made to reduce computational complexity while preserving physical accuracy. The simulation domain was constructed based on an industrial cooling plate geometry, with refinement strategies implemented to capture the coolant-air interface accurately. A mesh convergence study was conducted, and turbulence was modeled using three approaches: Unsteady Reynolds-Averaged Navier-Stokes (URANS), Large Eddy Simulation (LES), and Detached Eddy Simulation (DES). Among these, LES demonstrated the best resolution of turbulent structures with an acceptable computational cost.

To validate the model, experimental data was acquired from a transparent prototype using high-speed imaging and custom image-processing algorithms to detect air bubbles. The simulation showed good agreement with experimental results in terms of bubble size, distribution, and air volume at the end of the degassing process. The gas-liquid ratio (GLR) was used as a convergence metric to determine the end-state of the simulation. Figure 1 shows an example frame from the test video with image processing and a scatter plot o comparison between the bubbles positions and sizes during the quasi-steady state of the flow in the test and simulations.

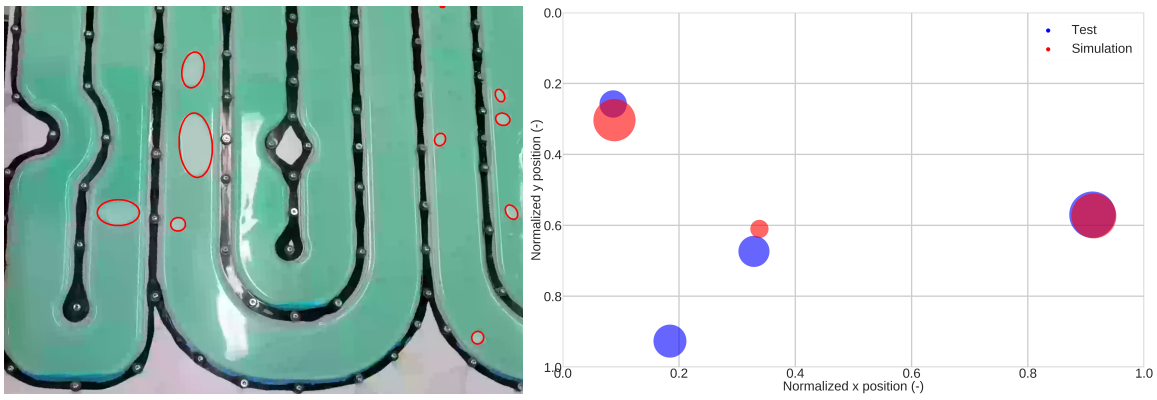

(a) Result of bubble detection on an example frame of the test data during transient phase.

(b) Scatter plot of detected bubbles positions sized by bubble diameter in the test and simulation results.

Figure 1: Overview of test data and validation.

An important aspect of this work was the evaluation of single-phase indicators as tools

for rapid design screening. Among velocity magnitude, vorticity, pressure gradients, Q-criterion, and λ_2 criterion, the velocity magnitude consistently correlated with bubble entrapment locations observed in multiphase simulations, as shown in Figure 2. This suggests that single-phase simulations may be used to identify critical areas in early-stage design, reducing computational effort of over 90%.

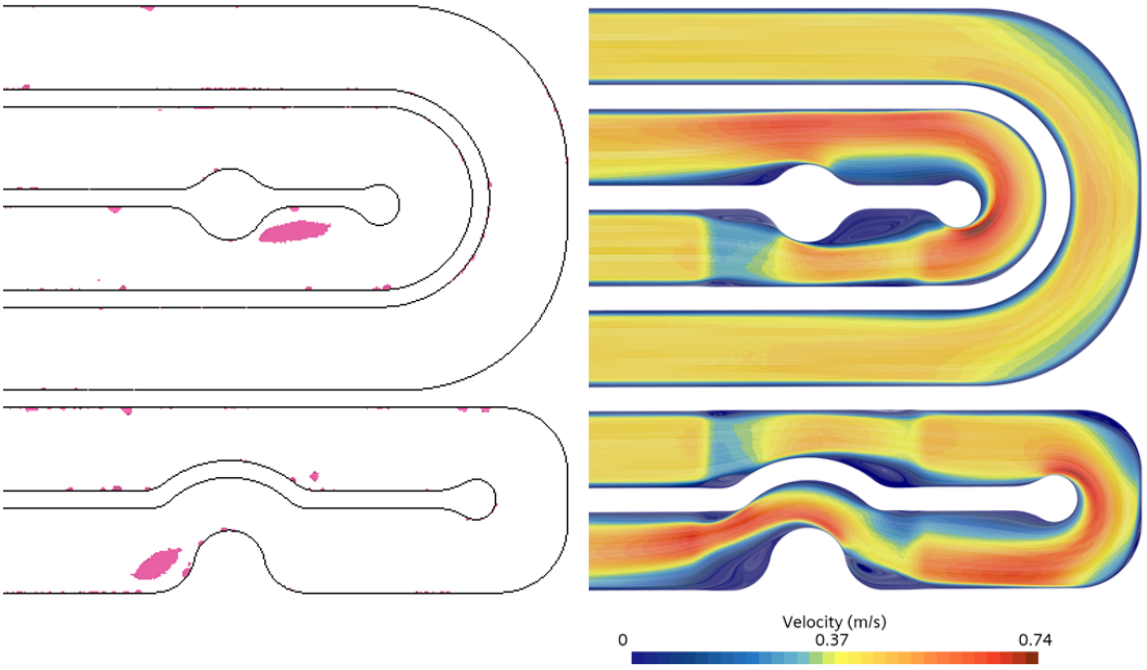

(a) Air pockets in the multiphase simulation, shown through a threshold in air volume fraction.

(b) LIC of velocity in a section in the vertical direction, colored by velocity magnitude, in the single phase simulation.

Figure 2: Comparison between multiphase and single-phase simulations.

The validated simulation framework was applied to two additional geometries: an improved version of the base cooling plate and a novel conceptual design. In both cases, the model successfully identified air entrapment zones and demonstrated how design changes could mitigate degassing issues. The improved geometry, in particular, showed a substantial reduction of 70% in residual air volume, validating the close relationship between geometric design choices and residual air.

Overall, this thesis presents a reliable and efficient approach for modeling degassing in EV battery cooling plates. The results show that CFD simulations, when combined with physical validation and post-processing, can effectively guide design improvements and reduce reliance on expensive prototyping.

Nomenclature

Standard SI-Units are used throughout.

Table 1: General Abbreviations

Abbreviation	Description
AMR	Adaptive Mesh Refinement
BTMS	Battery Thermal Management System
CFD	Computational Fluid Dynamics
CSF	Continuum Surface Force
DEM	Discrete Element Method
DES	Detached Eddy Simulation
DNS	Direct Numerical Simulation
DOE	Design of Experiments
EB-RSM	Elliptic Blending Reynolds Stress Model
GLR	Gas–Liquid mass ratio
HRIC	High-Resolution Interface Capturing
LES	Large Eddy Simulation
PCM	Phase Change Material
RANS	Reynolds-Averaged Navier–Stokes
RSM	Reynolds Stress Model
SIMPLE	Semi-Implicit Method for Pressure Linked Equations
URANS	Unsteady Reynolds-Averaged Navier–Stokes
VOF	Volume of Fluid
WALE	Wall-Adapting Local Eddy-viscosity

Table 2: Subscripts

Subscript	Description
0	Reference condition
f	Coolant phase (fluid)
g	Gas phase (air)
i	Cartesian component index (x, y, z)
t	Turbulent quantity
g	Gas phase
l	Liquid phase
sgs	Subgrid-scale (LES)

Table 3: Symbols (General)

Symbol	Description	Unit
d	Characteristic length (channel width)	m
Re	Reynolds number	—
Re_r	Relative Reynolds number	—
GLR	Gas–Liquid mass ratio	—
α	Volume fraction of coolant	—
u_i	Velocity component in direction i	m/s
p	Static pressure	Pa
ρ	Mixture density	$\mathrm{kg/m^3}$
ρ_p	Particle density	$\mathrm{kg/m^3}$
ρ_g	Gas density	$\mathrm{kg/m^3}$
μ	Dynamic viscosity	Pa·s
μ_t	Turbulent (eddy) viscosity	Pa·s
f_{st}	Surface tension force per volume	$\mathrm{N/m^3}$
g_i	Gravitational acceleration component	$\mathrm{m/s^2}$
k	Turbulent kinetic energy	$\mathrm{m^2/s^2}$
ϵ	Turbulent dissipation rate	$\mathrm{m^2/s^3}$
u_{bulk}	Bulk velocity	m/s
m_g	Mass of gas	kg
m_l	Mass of liquid	kg
μ_{sgs}	Subgrid-scale eddy viscosity	Pa·s
Δ	Grid filter width	m
P_k	Production of turbulent kinetic energy	$\mathrm{kg/(m{\cdot}s^3)}$
σ_k	Turbulent Prandtl number for k	–
σ_ϵ	Turbulent Prandtl number for ϵ	–
C_μ, C_T, C_{DES}	Turbulence model constants	–
ϕ	Blending function in EB-RSM	–
S	Strain rate magnitude	1/s
T	Turbulent time scale	s
T_e	Large-eddy turnover time	s
y^+	Non-dimensional wall distance	–

Table 4: Greek Symbols

Greek Symbol	**Description**	**Unit**
σ	Surface tension coefficient	N/m
ν	Kinematic viscosity	m^2/s
τ_{ij}	Stress tensor	Pa
ϵ_g	Gas phase volume fraction	—
α_i	Volume fraction of phase i	–
ϵ	Turbulent dissipation rate	m^2/s^3
ϵ_g	Gas volume fraction	–
μ	Dynamic viscosity	Pa·s
ν	Kinematic viscosity	m^2/s
ρ_i	Density of phase i	kg/m^3

Contents

List of Figures

List of Tables

Chapter 1

Introduction

1.1 Decarbonization of the Transportation Sector

The transportation sector is one of the largest contributors to global CO_2 emissions, primarily due to the widespread use of internal combustion engine (ICE) vehicles.

The Fit-for-55 regulation introduces progressive emissions reduction targets in the European Union for cars and vans. This includes a 100% reduction target for 2035 for new ICE vehicles, banning their sale and only selling Electric vehicles (EVs) (European Council, 2022).

EVs present a promising alternative, particularly when powered by renewable energy sources. Unlike ICE vehicles, EVs produce no tailpipe emissions, and their overall carbon footprint can be significantly reduced when charged with electricity from solar, wind, or hydroelectric power.

Neugebauer et al. (2022) compared the emissions of the entire life cycle of ICE cars and electric cars, considering different configurations of electricity generation, concluding that with average use of the vehicle, electric cars allow reducing the total CO_2 emissions after a reasonable amount of years of use, when the electricity used in the EV is not generated completely by carbon combustion. In the case of a use of solely renewable sources, and average use of the vehicle, the total CO_2 emissions of the EV were calculated to be 45% of the ICE vehicle. This study also underlines the importance of the durability of the battery component of EV for a further reduction of emissions.

However, the transition to EVs presents engineering challenges, particularly in battery performance, safety, and thermal management. One critical aspect is the design of efficient battery cooling systems, which ensure reliable operation and longevity of EV batteries.

1.2 EV Battery Cooling

Lithium-ion batteries are the dominant energy storage technology for EVs due to their high energy density, efficiency, and relatively long lifespan (Nilsson and Ahlberg Tidblad, 2024). However, they are highly temperature-sensitive, requiring precise thermal management to ensure safe and efficient operation (Deng et al., 2018). Figure 1.1 illustrates the placement of the battery and related components, such as the cooling plate, inside a car.

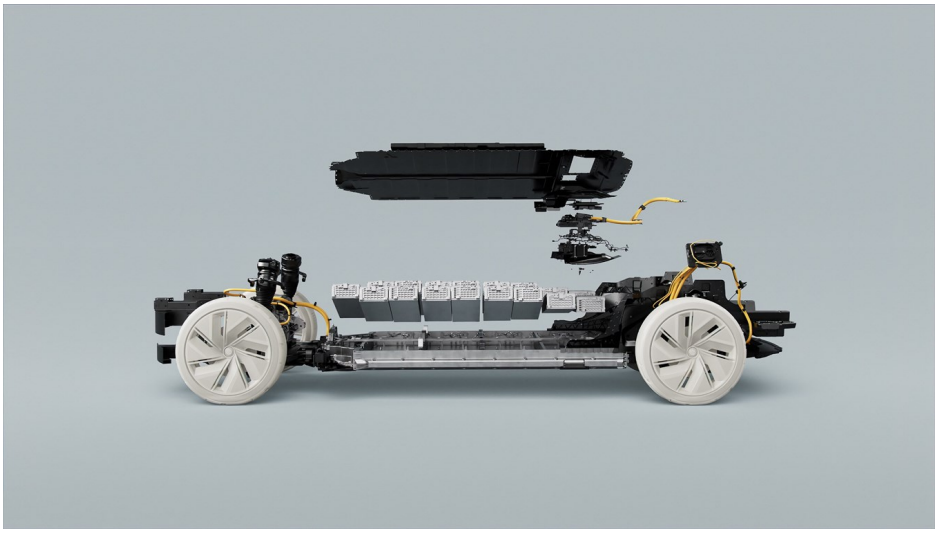

Figure 1.1: Exploded view of the battery components in a car (Volvo Cars, 2022).

1.2.1 Impact of Temperature on Battery Performance and Safety

Due to their material properties, lithium-ion batteries operate optimally within a narrow temperature range of 20–40°C (Yan et al., 2016). Deviations from this range can lead to several performance and safety issues:

- **High temperatures ($> 40^{\circ}$C):** Excessive heat accelerates capacity fade, increases internal resistance, and promotes side reactions within the electrolyte, leading to gas generation and potential swelling of battery cells (Oh et al., 2014). If the temperature widely exceeds its working range, the risk of thermal runaway increases significantly (Sun et al., 2016). This phenomenon, often triggered by internal short circuits or excessive current flow, can cause the uncontrolled release of energy, resulting in fire, smoke, and harmful gas emissions (Nilsson and Ahlberg Tidblad, 2024).
- **Low temperatures ($< 0^{\circ}$ C):** Cold conditions reduce the battery's ionic conductivity, leading to power loss and capacity fade. At extreme cold temperatures, lithium plating may occur, which can permanently damage the battery and increase the risk of short circuits (Luo et al., 2023).
- **Temperature non-uniformity:** Even if the overall battery pack is within the optimal range, localized hotspots can form due to uneven cooling. This leads to accelerated degradation of specific cells, reducing the overall lifespan of the battery pack and increasing the likelihood of early failure (Liu et al., 2017).

To address these challenges, battery thermal management systems (BTMS) are essential for maintaining an optimal and uniform temperature distribution within the battery pack.

1.2.2 Battery Thermal Management Systems (BTMS)

A BTMS is designed to regulate battery temperature, ensuring safe operation and prolonging battery life. Various cooling strategies exist as reviewed by Ubale and Ubale (2022), including:

- **Air cooling:** Uses forced or natural convection to dissipate heat. This method is simple and low-cost but has poor heat transfer efficiency and struggles to maintain uniform temperatures, making it unsuitable for high-power applications (Sun and Dixon, 2014).
- **Liquid cooling:** Uses coolant flowing through channels to absorb and transfer heat away from the battery pack. Liquid cooling is the most efficient method due to its high heat capacity and superior heat transfer properties (Gu et al., 2025).
- **Phase change material (PCM) cooling:** Utilizes materials that absorb heat during phase transition (e.g., from solid to liquid) to regulate temperature. While effective for passive cooling, PCMs have limited thermal conductivity and may require additional heat dissipation mechanisms (Wang et al., 2018).
- **Refrigerant-based cooling:** Similar to automotive air conditioning systems, this method directly cools the battery using refrigerants. While highly efficient, it requires complex infrastructure and increases system cost (Yao et al., 2021).

Among these methods, liquid cooling is the most widely used solution in modern EVs due to its ability to maintain uniform temperatures while handling high thermal loads efficiently.

1.2.3 Liquid Cooling Systems in EV Batteries

Liquid cooling systems circulate a coolant, typically a water-glycol mixture or a dielectric fluid, through channels embedded in battery packs. These systems remove excess heat by:

1. Conducting heat from the battery cells to the coolant through direct contact with cooling plates or tubes.
2. Convecting heat away as the coolant flows through the circuit.
3. Dissipating heat externally via a radiator or heat exchanger.

1.2.4 Design Challenges in Liquid Cooling Plates

Although liquid cooling is an effective method for battery thermal management, designing an efficient cooling plate involves balancing multiple, often competing, objectives. Engineers must address several key challenges to ensure performance, safety, and manufacturability:

- **Heat transfer efficiency:** The cooling plate must provide sufficient surface contact and convective heat transfer to maintain all battery cells within the desired temperature range. This requires optimizing channel geometry to ensure uniform coolant distribution across the entire battery pack.
- **Pressure drop:** Excessive pressure losses in the cooling channel network increase the load on pumps, raising energy consumption and system complexity. Designers must minimize hydraulic resistance without sacrificing thermal performance.

- **Coolant velocity and erosion risk:** While higher velocities improve convective heat transfer, they can also induce erosion, especially near sharp turns or abrupt cross-sectional changes. Maintaining moderate flow speeds helps avoid long-term damage to the system.
- **Coolant volume and packaging:** Larger fluid volumes may improve thermal capacity but increase system weight and volume. In EVs, space constraints and the need for compact packaging require minimizing coolant volume without compromising performance.
- **Air entrapment and degassing:** Air bubbles trapped during filling or operation degrade thermal performance and create localized hotspots. The cooling plate must be designed to facilitate passive or active degassing.

To address these multi-objective design considerations, engineers increasingly rely on simulation-based optimization. Computational Fluid Dynamics (CFD) tools such as Simcenter STAR-CCM+ can simulate the thermal and hydraulic behavior of different cooling plate designs under realistic conditions. These tools support:

- **Design of Experiments (DOE)** to explore the effect of geometric parameters on performance.
- **Multi-objective optimization** (e.g., using Pareto front analysis) to identify trade-offs between competing goals like thermal uniformity and pressure drop.
- **Sensitivity analysis** to determine which geometric features most influence performance.

However, while numerical optimization can suggest high-performing solutions, many of these designs may not be manufacturable at scale. For instance, complex channel geometries or extremely tight tolerances might improve heat transfer but exceed practical limits of current production methods such as stamping, extrusion, or brazing.

Specifically, this study focuses on degassing, trapped air bubbles within the cooling circuit can reduce heat transfer efficiency and lead to temperature non-uniformity. This is why degassing plays a crucial role in ensuring optimal thermal management.

1.3 Degassing in Battery Cooling Plates

Battery cooling plates are designed to efficiently transfer heat away from lithium-ion cells, ensuring safe operation and longevity of electric vehicle (EV) batteries. However, during the filling and operation of liquid cooling systems, air pockets can become trapped in the coolant flow. These air bubbles significantly impact the cooling efficiency and system performance.

While air bubbles do not pose a direct safety risk, they cause non-uniform cooling and localized overheating, potentially leading to accelerated degradation of certain battery cells. Proper degassing is therefore essential to maintain the performance and reliability of the thermal management system.

1.3.1 Issues with Air Bubbles in the Cooling Plate

The presence of air bubbles in cooling plates leads to several performance issues, including:

- **Reduced heat transfer efficiency:** Air has a much lower thermal conductivity ($\approx$ 0.026 W/m·K) compared to liquid coolants such as water-glycol mixtures ($\approx$ 0.5 W/m·K). Even small air pockets act as thermal insulation barriers, reducing the rate of heat dissipation from the battery to the coolant.
- **Localized overheating and temperature non-uniformity:** Air bubbles disrupt the smooth flow of coolant, leading to hot spots where heat is not effectively removed. This accelerates degradation in specific battery cells and can shorten the lifespan of the battery pack.
- **System maintenance and reliability concerns:** Air trapped inside the system may gradually accumulate over time, requiring periodic maintenance or air-bleeding procedures. If degassing is not performed effectively, the system may experience performance degradation and increased operating costs.

These issues highlight the necessity of efficient degassing techniques to ensure optimal cooling performance. The next section discusses different strategies for removing trapped air from the system.

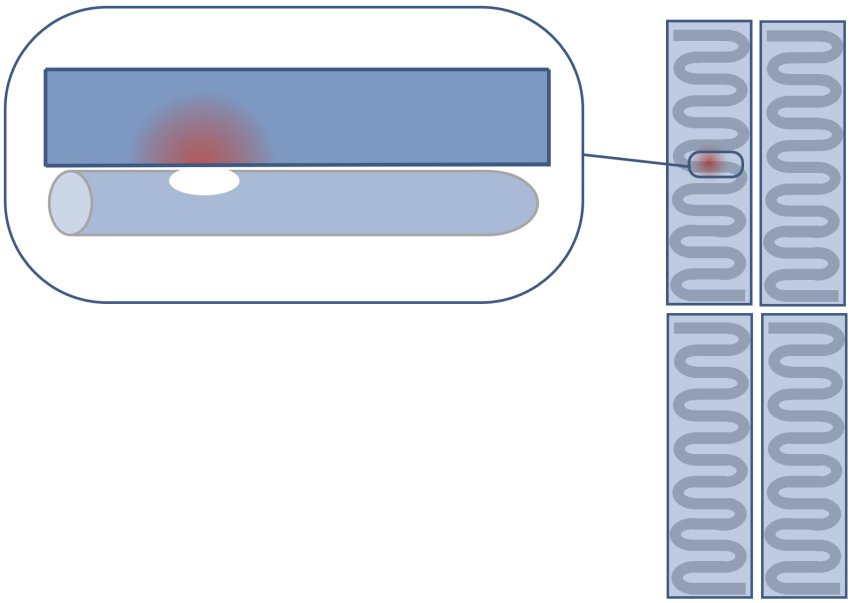

Figure 1.2: Illustration of air pockets affecting heat transfer in battery cooling plates.

1.3.2 Strategies for Degassing

To ensure complete removal of air pockets from the cooling system, various degassing strategies can be employed. These can be broadly classified into passive and active degassing methods.

Passive Degassing

Passive degassing relies on the natural movement of air bubbles to remove them from the system without external intervention. These methods include:

- **Air bleeding valves:** Small air vents placed at high points in the cooling system allow trapped air to escape automatically as coolant flows through the system.
- **Gravity-based degassing:** By designing the cooling plate geometry with upward-sloping channels, air bubbles are naturally directed toward exit points where they can be vented out.
- **Settling chambers:** Some designs incorporate expansion tanks or reservoirs where air bubbles can accumulate and be removed from the circuit (Tao et al., 2022).

Passive degassing is effective for long-term operation, but may not be sufficient for removing all air pockets during the initial filling process.

Active Degassing

Active degassing techniques involve external intervention to forcefully remove air pockets from the cooling circuit. These include:

- **Vacuum degassing:** Before the coolant is introduced, the entire system is placed under vacuum to remove trapped gases. This method is highly effective but requires additional vacuum equipment.
- **High-flow degassing:** Coolant is pumped rapidly through the system to flush out air pockets. The high velocity of the liquid increases shear forces, dislodging bubbles and carrying them toward exit points.
- **Ultrasonic degassing:** High-frequency vibrations are applied to break up air pockets and promote their removal (Eskin, 2015). This technique is used in specialized applications, but is less common in automotive cooling systems.
- **Gas-separating membranes:** Some advanced cooling systems use porous membranes that allow air to escape while retaining liquid coolant (Chen et al., 2023).

Among these methods, high-flow degassing is the focus of this study, as it provides a practical and efficient approach to ensuring air-free coolant circulation.

1.3.3 Experimental Challenges

It is important to acknowledge that the trajectory of air movement within the cooling plate, and thus its degassing process, is significantly influenced by its path. Hence, it is crucial to design the geometry of the cooling plate with careful consideration of the degassing operation. To accomplish this, a method of analysis of the proposed design iterations is required, this can be done through experiments or numerical modeling.

The experimental study of degassing in battery cooling plates presents significant experimental challenges. The primary issue is that air pockets are difficult to measure and can

be located in any point of the cooling plate, requiring the production of transparent prototypes for direct observation. Furthermore, the interface between coolant and air pockets is highly dynamic, involving bubble detachment, coalescence, and turbulent mixing, increasing the difficulty of the detection and analysis of them. Considering these factors, it is clear that testing multiple geometries experimentally is costly and time-consuming, making numerical simulations a valuable alternative.

Computational Fluid Dynamics (CFD) provides a powerful tool to analyze air removal mechanisms, optimize cooling plate designs, and reduce reliance on physical prototypes.

1.4 Numerical Modeling of Degassing

The degas process is a complex fluid dynamics problem characterized by multiphase, multi-species and turbulent flow. Simulating it requires accurate description of all these aspects and consequently involves the issue of facing high computational costs.

1.4.1 Multiphase Flow Modeling Approaches

Several numerical techniques exist for modeling multiphase flows, each with advantages and limitations:

- **Volume of Fluid (VOF) Method:** Tracks a sharp interface between immiscible fluids (coolant and air). It is suitable for flows with a sharp interface between the phases, accurately characterize the moving interface of bubbles merging and separating. This method is computationally efficient compared to other interface-tracking methods (Mulbah et al., 2022).
- **Mixture Model:** Assumes interpenetrating phases with a shared velocity field. The mixture model is suitable for small dispersed bubbles but lacks interface resolution. It is less accurate for large bubbles or free-surface flows like degassing. (Mikko et al., 1996).
- **Eulerian-Lagrangian (CFD-DEM) Model:** Represents air bubbles as discrete particles (using the Discrete Element Method, DEM). The CFD-DEM coupling allows detailed tracking of bubble motion. It is computationally expensive for large-scale systems (Norouzi et al., 2016).

Considering the displacement of substantial air pockets by the coolant in the process of degassing, the Volume of Fluid (VOF) method emerges as the most suitable choice. This method is capable of accurately delineating the air-liquid interface while minimizing computational resource demands. Additionally, degassing encompasses the coalescence of bubbles and their partial disruption, wherein fragments may be transported by the primary flow. This underscores the requirement for a model that precisely evaluates the interface between phases and accommodates morphological changes in the bubbles without imposing excessive computational burdens.

1.4.2 The Volume of Fluid (VOF) Method

The VOF method is a surface-tracking technique that models the interface between immiscible fluids, originally formulated by Hirt and Nichols (1981). It introduces a volume fraction function, α, defined as:

- $\alpha = 1 \Rightarrow$ the cell is fully occupied by the liquid (coolant).
- $\alpha = 0 \Rightarrow$ the cell contains only air.
- $0 < \alpha < 1 \Rightarrow$ the cell contains an interface between coolant and air.

The evolution of α is governed by the advection equation:

$$\frac{\partial \alpha}{\partial t} + \nabla \cdot (\alpha \mathbf{u}) = 0 \tag{1.1}$$

where $\mathbf{u}$ is the velocity field of the fluid. Figure 1.3 shows how in the VOF method, the fraction of each phase is tracked in each cell of the domain.

To maintain a sharp interface, numerical schemes such as geometric reconstruction (PLIC) or compressive volume fraction methods are applied.

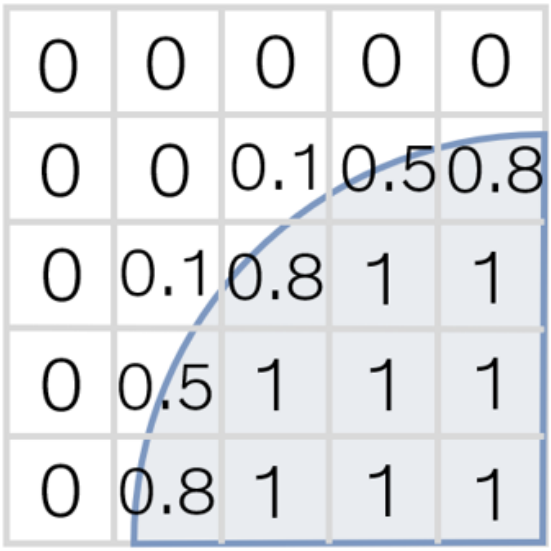

Figure 1.3: Illustration of the VOF method tracking the coolant-air interface.

1.4.3 VOF in the Literature

The Volume of Fluid (VOF) method has been widely adopted in the literature for the analysis of multiphase flows relevant to cooling systems in electric vehicles. For instance, Tao et al. (2022) employed the VOF approach to simulate the filling and subsequent de-aeration of a battery electric vehicle (BEV) cooling circuit. Their work focused on assessing the de-aeration capabilities of the system, particularly the function of a degas bottle designed to accumulate and remove air bubbles from the circuit. The system of study in this work does not involve the usage of a degas bottle. Similarly, Shirsikar et al. (2021) conducted

a numerical study aimed at the geometric optimization of a cooling system incorporating a degas bottle for engine thermal management. Their simulation results were validated against experimental data obtained using a transparent physical prototype, demonstrating good agreement and confirming the model's reliability. In this work, testing on a transparent physical prototype is used as well to validate the model. Another related study by Brahmasani et al. (2014) explored a comparable system equipped with a secondary de-aeration loop. This investigation centered on the effects of different configurations of a multi-position valve and their influence on the overall air removal performance of the system. This approach is not implemented in the current study as a significant change in the current BTSM technology in use is not involved in this work.

Beyond applications in vehicle cooling systems, the VOF method is also extensively utilized to model bubble dynamics in general multiphase flows. As reviewed in Mulbah et al. (2022), VOF proves to be a robust and practical choice for simulating flows involving immiscible fluids where significant interfacial deformation and complex bubble geometries occur. These characteristics make the method particularly attractive for industrial applications that demand accurate tracking of phase boundaries under dynamic conditions.

1.4.4 Challenges in Computational Modeling

Despite its advantages, VOF-based degassing simulations are computationally demanding due to its requirement of high resolution in terms of mesh. Accurately capturing the air-liquid interface requires fine mesh grids, as the smallest scale of bubbles represented is dependent on the mesh cells size as well as their accurate movement in the fluid phase. Another requirement that represents a challenge when using this modeling approach is requirement of small time steps for stability and characterization of the movement of the interphase. This imply a higher computational cost of transient simulations.

1.4.5 Strategies for Reducing Computational Cost

To ensure feasibility while maintaining accuracy, the following methods can be considered:

- **Single-Phase Indicators for Air Entrapment Areas:** Instead of fully resolving the air-liquid interface in all cases, single-phase simulations with scalar indicators may be used to estimate air removal efficiency.
- **Adaptive Mesh Refinement (AMR):** Adaptive mesh refinement enhances VOF by introducing refinement varying in time grid levels within the original grid to capture localized flow characteristics more accurately. The integration of the VOF method with adaptive mesh refinement enables precise representation of the gas–liquid interface while reducing the overall number of grid cells.
- **Steady-State Approximations:** Steady-state simulations can approximate air removal efficiency, avoiding the high cost of transient simulations. This approach is generally not recommended for multiphase flows simulations.
- **2D Modeling for Preliminary Studies:** Simulating a 2D slice of the cooling plate allows faster simulations and insights before moving to full 3D cases, depending on the specific geometry.

Chapter 2

Problem Statement

The rise in electric vehicle demand has heightened the importance of lithium-ion battery performance and safety. Battery thermal management systems (BTMSs) are essential for regulating temperatures, preventing thermal runaway, and extending battery life. Liquid cooling is the most common BTMS technique; however, air bubbles trapped in cooling plates can significantly hinder heat transfer, resulting in uneven cooling, decreased efficiency, and potential early battery deterioration. The process of removing these air pockets, known as degassing, is therefore essential. However, due to the high cost of producing a new transparent component for each design iteration, experimental observation of the degassing process is limited. As a result, numerical modeling presents a compelling alternative, allowing for controlled investigations and design optimization. This leads to the following problem statement.

How can numerical modeling effectively simulate the degassing process in EV battery cooling plates, while ensuring accurate representation of multiphase flow dynamics, minimizing computational costs, and maintaining predictive reliability for practical applications?

This study seeks to develop a simulation framework that can accurately and efficiently capture the degassing process within battery cooling channels. By employing the VOF method within a CFD framework, focusing on the behavior of trapped air and its displacement by coolant flow, this work aims to provide a predictive tool that supports cooling system design and performance improvement.

2.1 Methodology

To address the research question, a computational fluid dynamics (CFD) approach will be employed, centered around the Volume of Fluid (VOF) method for multiphase flow modeling. The methodology includes:

- **Numerical Modeling:** The degassing process will be simulated using Computational Fluid Dynamics (CFD) with the Volume of Fluid (VOF) method applied to resolve the coolant-air interface. The simulations will be performed with the commercial software STAR-CCM+.
- **Experimenting:** A transparent physical prototype will be utilized to conduct testing on the degassing process.
- **Model Validation:** The developed model will be validated against the experimental data.
- **Simulation Performance Improvement Analysis:** Various methodologies to diminish computational expenses without compromising the integrity of the results will be explored.

2.2 Assumptions and Simplifications

To ensure the computational feasibility of the problem while maintaining its relevance to physical phenomena, the following assumptions will be adopted:

- **Purely Liquid Inlet:** The ingress of air during the degassing phase is assumed to be negligible. This assumption reduces computational complexity and facilitates a clearer analysis of the degassed final state.
- **Uniform Velocity Inlet:** A uniform velocity profile is presumed at the system's inlet, a simplification that is considered not to significantly affect the final results.
- **Filling Process Omitted:** To considerably reduce computational demands, the process of filling is not simulated. Instead, an initial condition field profile is preassigned to establish the volume fraction at the onset of the simulation.
- **Isothermal conditions:** Thermal effects within the simulations are neglected, under the assumption of a constant fluid temperature. This method streamlines the analysis and focuses specifically on the mechanisms of degassing.

Chapter 3

Numerical Methods

This chapter details the methodology for the numerical simulations performed in this study, such as: the governing equations for the two-phase flow model, the simulation set up, and the grid convergence analysis.

3.1 Dimensionless Numbers

Throughout this study, dimensionless numbers are utilized to normalize specific parameters, thereby enhancing the reproducibility of the results while preserving the confidentiality of sensitive information. The Reynolds number, Re, quantifies the ratio of inertial forces to viscous forces, as shown below:

$$\mathrm{Re} = \frac{\rho d u_{bulk}}{\mu} \tag{3.1}$$

where ρ is the coolant density, d is the cooling plate channel width, u_{bulk} is the bulk velocity and μ is the dynamic viscosity of the liquid.

The gas-to-liquid mass ratio (GLR) is defined as the ration between mass of gas and mass of liquid in the system:

$$\mathrm{GLR} = \frac{m_g}{m_l} \tag{3.2}$$

where m_g is the total amount of gas in the system and m_l is the total amount of liquid in the system. It is useful to identify the extent of trapped air in the system at the end of the degassing process. Furthermore, if its value stops varying it indicates the end of the process, allowing the analysis of the remaining air pockets trapped in the system.

3.2 Governing Equations

This section outlines the fundamental equations governing the multiphase, turbulent flow in the cooling plate during the degassing process. The numerical model solves the incompressible Navier–Stokes equations, augmented with a turbulence model, surface tension force, and a volume fraction transport equation for interface tracking.

3.2.1 Continuity and Momentum Equations

The flow is considered incompressible, and both air and coolant are treated as Newtonian fluids. The mass and momentum conservation equations take the form:

$$\nabla \cdot \mathbf{u} = 0 \tag{3.3}$$

$$\rho\left(\frac{\partial \mathbf{u}}{\partial t}+\mathbf{u}\cdot\nabla\mathbf{u}\right)=-\nabla p+\nabla\cdot\left[\mu\left(\nabla\mathbf{u}+\nabla\mathbf{u}^{T}\right)\right]+\mathbf{f}_{st}+\rho\mathbf{g} \tag{3.4}$$

where $\mathbf{u}$ is the velocity field, p is pressure, ρ is the local density, μ is the dynamic viscosity, $\mathbf{f}_{st}$ represents the surface tension force, and $\mathbf{g}$ is the gravitational acceleration. The fluid properties ρ and μ are computed as weighted averages based on the volume fraction α, as already introduced in Section 1.4.2 via the VOF method.

3.2.2 Turbulence Modeling

The primary focus of this research is the presence of residual bubbles within the cooling plates. While a steady-state simulation would be possibly sufficient, in the context of use of the Volume of Fluid (VOF) method, it is not advisable to perform steady state simulations, furthermore this option has been removed in StarCCM+. Necessitating a choice between Large Eddy Simulation (LES), Detached Eddy Simulation (DES) and Unsteady Reynolds-Averaged Navier-Stokes (URANS) for turbulence modeling.

In this work, the three mentioned turbulence modeling approaches have been employed to analyze the difference in computational times and results and identify which one is the most appropriate for the studied application.

3.2.3 Unsteady Reynolds-Averaged Navier-Stokes

An accurate representation of complex flow structures during the degassing process, requires a robust turbulence model. In the context of URANS, this study employs the standard k-ϵ two-equation model, enhanced by the Lag Elliptic Blending (Lag EB) approach, to improve predictions in non-equilibrium and near-wall flow regimes.

The Lag EB model extends the original Elliptic Blending Reynolds Stress Model (EB-RSM), as simplified by Manceau (2002), making it more computationally suitable for industrial applications. It incorporates a stress-strain lag formulation introduced by Revell et al. (2006), which accounts for the delayed response of Reynolds stresses to abrupt changes in the mean strain rate. This formulation is particularly critical in scenarios involving significant flow curvature, rotation, or separation. The turbulence model solves transport equations for the turbulent kinetic energy k and its dissipation rate ϵ:

$$\frac{\partial(\rho k)}{\partial t}+\nabla\cdot(\rho k\mathbf{u})=\nabla\cdot\left[\left(\mu+\frac{\mu_t}{\sigma_k}\right)\nabla k\right]+P_k-\rho\epsilon \tag{3.5}$$

$$\frac{\partial(\rho \epsilon)}{\partial t}+\nabla\cdot(\rho \epsilon\mathbf{u})=\nabla\cdot\left[\left(\mu+\frac{\mu_t}{\sigma_\epsilon}\right)\nabla \epsilon\right]+C_{1\epsilon}\frac{\epsilon}{k}P_k-C_{2\epsilon}\rho\frac{\epsilon^2}{k} \tag{3.6}$$

where:

- ρ is the fluid density,
- μ is the molecular dynamic viscosity,
- μ_t is the turbulent (eddy) viscosity,
- P_k is the production rate of turbulent kinetic energy,

- σ_k, σ_ϵ, $C_{1\epsilon}$, and $C_{2\epsilon}$ are model constants.

The turbulent viscosity μ_t is defined as:

$$\mu_t = \rho C_\mu \phi k \cdot \min\left(T, \frac{C_T}{\sqrt{3} C_\mu \phi S}\right) \tag{3.7}$$

where:

- C_μ, C_T are model coefficients,
- ϕ is a blending function accounting for near-wall effects and anisotropy,
- S is the magnitude of the strain rate tensor,
- T is the turbulent timescale.

The turbulent timescale T is given by:

$$T = \sqrt{T_e^2 + C_t^2 \frac{\nu}{\epsilon}} \tag{3.8}$$

where $T_e = \frac{k}{\epsilon}$ is the large-eddy turnover time, C_t is a model constant, and ν is the kinematic viscosity.

The Lag EB model enhances the predictive capability in flows where the alignment between the Reynolds stress tensor and the strain rate tensor is delayed—often observed in transient or separated flows. By incorporating anisotropic stress behavior and curvature correction implicitly, this model improves accuracy without requiring the full complexity of Reynolds Stress Models (RSM).

This turbulence approach is particularly appropriate for modeling coolant injection and the associated degassing phenomena, where high shear, unsteady recirculation, and anisotropic turbulence are expected to play a significant role in bubble dynamics and air displacement.

3.2.4 Large Eddy Simulation (LES)

Large Eddy Simulation (LES) resolves the large-scale, energy-containing turbulent structures directly, while modeling only the small-scale dissipative motions using a subgrid-scale (SGS) model. This approach provides improved accuracy over RANS in capturing unsteady flow phenomena and interface dynamics (Nicoud and Ducros, 1999) , particularly in multiphase flows involving bubble breakup and coalescence.

In this study, the Wall-Adapting Local Eddy-viscosity (WALE) model is employed for subgrid-scale turbulence modeling. The subgrid-scale eddy viscosity μ_{sgs} in the WALE model is given by:

$$\mu_{sgs} = \rho (C_w \Delta)^2 \frac{(S_{ij}^d S_{ij}^d)^{3/2}}{(\bar{S}_{ij}\bar{S}_{ij})^{5/2} + (S_{ij}^d S_{ij}^d)^{5/4}} \tag{3.9}$$

where:

- C_w is the WALE model constant,
- Δ is the local grid filter width,
- $\bar{S}_{ij}$ is the resolved strain rate tensor,
- S^d_{ij} is the traceless symmetric part of the square of the velocity gradient tensor.

LES with WALE is particularly suited for predicting transient bubble interactions, turbulence-induced detachment, and interface wrinkling in coolant flow through complex channel geometries. However, it can be computationally expensive as it requires fine mesh resolution across the domain, particularly near walls and interfaces.

3.2.5 Detached Eddy Simulation (DES)

Detached Eddy Simulation (DES) is a hybrid turbulence modeling approach that combines the benefits of Reynolds-Averaged Navier-Stokes (RANS) and Large Eddy Simulation (LES). In near-wall regions and attached boundary layers, DES behaves like a RANS model, while in separated regions or far from walls, it transitions to LES, enabling the resolution of large unsteady turbulent structures (Spalart et al., 1997).

In this study, the DES approach is based on the k-ϵ Elliptic Blending (EB) RANS model as its base. The eddy-viscosity is modified through a length scale substitution, allowing the model to switch from RANS to LES behavior depending on the local flow field and grid resolution.

The key modification lies in the turbulence length scale l, which is adapted as:

$$l_{DES} = \min(l_{RANS}, C_{DES}\Delta) \tag{3.10}$$

where:

- l_{RANS} is the turbulence length scale from the RANS model,
- Δ is the local grid spacing, the filter width,
- C_{DES} is a model constant.

This formulation ensures that DES behaves like RANS in finely resolved near-wall regions and transitions to LES in separated zones where the grid can resolve turbulent eddies.

In some cases, DES offers a favorable compromise between accuracy and computational cost, making it well-suited for industrial applications involving complex flow separations and transient air-liquid interactions, such as those observed during the degassing process in battery cooling plates.

3.2.6 Multiphase Interaction and Interface Capturing

The Volume of Fluid (VOF) method, previously introduced, is used here to simulate the interaction between immiscible phases, specifically, coolant and trapped air, within the cooling plate. Implemented via an interface-capturing approach, the method tracks the

distribution and movement of the phase interface across a fixed Eulerian mesh. This approach assumes sufficient mesh resolution to accurately resolve both the position and shape of the interfacial region (Fujimoto et al., 2007).

Each computational cell contains a phase volume fraction α_i, which represents the fraction of the volume occupied by phase i:

$$\alpha_i = \frac{V_i}{V_{\text{cell}}} \tag{3.11}$$

where V_i is the volume of phase i within the cell and V_{cell} is the total volume of the cell. For a two-phase system, such as air and coolant, the sum of volume fractions satisfies:

$$\sum_{i=1}^{2} \alpha_i = 1 \tag{3.12}$$

The physical properties such as density ρ and dynamic viscosity μ in each cell are calculated as volume-fraction-weighted averages of the constituent fluids:

$$\rho = \alpha_1 \rho_1 + \alpha_2 \rho_2, \quad \mu = \alpha_1 \mu_1 + \alpha_2 \mu_2 \tag{3.13}$$

The transport of the phase is governed by the phase mass conservation equation (Hirt and Nichols, 1981):

$$\frac{\partial}{\partial t} \int_V \alpha_i \, dV + \oint_A \alpha_i \mathbf{v} \cdot d\mathbf{a} = \int_V \left(S_{\alpha_i} - \frac{\alpha_i}{\rho_i} \frac{D\rho_i}{Dt} \right) dV - \int_V \frac{1}{\rho_i} \nabla \cdot (\alpha_i \rho_i \mathbf{v}_{d,i}) \, dV \tag{3.14}$$

where: $\mathbf{a}$ is the surface area vector, $\mathbf{v}$ is the mixture (mass-averaged) velocity, $\mathbf{v}_{d,i}$ is the diffusion (drift) velocity of phase i, S_{α_i} is a user-defined source term of phase α_i, $\frac{D\rho_i}{Dt}$ is the material (or Lagrangian) derivative of the phase density ρ_i.

In STAR-CCM+, the High-Resolution Interface Capturing (HRIC) scheme blends upwind and downwind differencing based on local flow conditions and phase gradients to accurately capture interface motion and deformation (Muzaferija and Peri'c, 1999). To reduce numerical smearing, the advection equation is typically solved only for the primary phase; the volume fraction of the secondary phase is implicitly set to satisfy the closure condition.

This method is especially suitable for modeling systems where the interface between fluids remains sharp and large-scale mixing is absent, such as the degassing process in EV battery cooling plates. It provides a balance between computational efficiency and physical fidelity, allowing for accurate prediction of bubble displacement, coalescence, and removal within complex flow passages.

3.2.7 Surface Tension Force

Surface tension plays a crucial role in multiphase flow, especially when bubbles are small and curved interfaces dominate local dynamics. Surface tension is crucial for maintaining the stability of phase interfaces. It induces pressure gradients to arise across these interfaces, resulting in differences between the internal and external pressures. The surface

tension force $\mathbf{f}_{st}$ is implemented using the Continuum Surface Force (CSF) model proposed by Brackbill et al. (1992):

$$\mathbf{f}_{st} = \sigma \kappa \nabla \alpha \tag{3.15}$$

where σ is the surface tension coefficient, κ is the curvature of the interface computed as:

$$\kappa = -\nabla \cdot \left(\frac{\nabla \alpha}{|\nabla \alpha|} \right) \tag{3.16}$$

and α is the volume fraction of the coolant phase. This force is added as a volumetric term in the momentum equation and is essential to capture bubble deformation, coalescence, and detachment behavior during coolant flow.

3.3 Simulation Setup

The computational domain consists of an electric vehicle battery cooling plate featuring a single coolant inlet and outlet, with internal flow passages.

The integral geometry of the cooling plate is not shown for confidentiality reasons, a small part of it is shown as in Figure 3.1, highlighting the flow directions in the passages shown, where the green arrows indicate the passage closest to the inlet and the red arrow indicates the passage closest to the outlet.

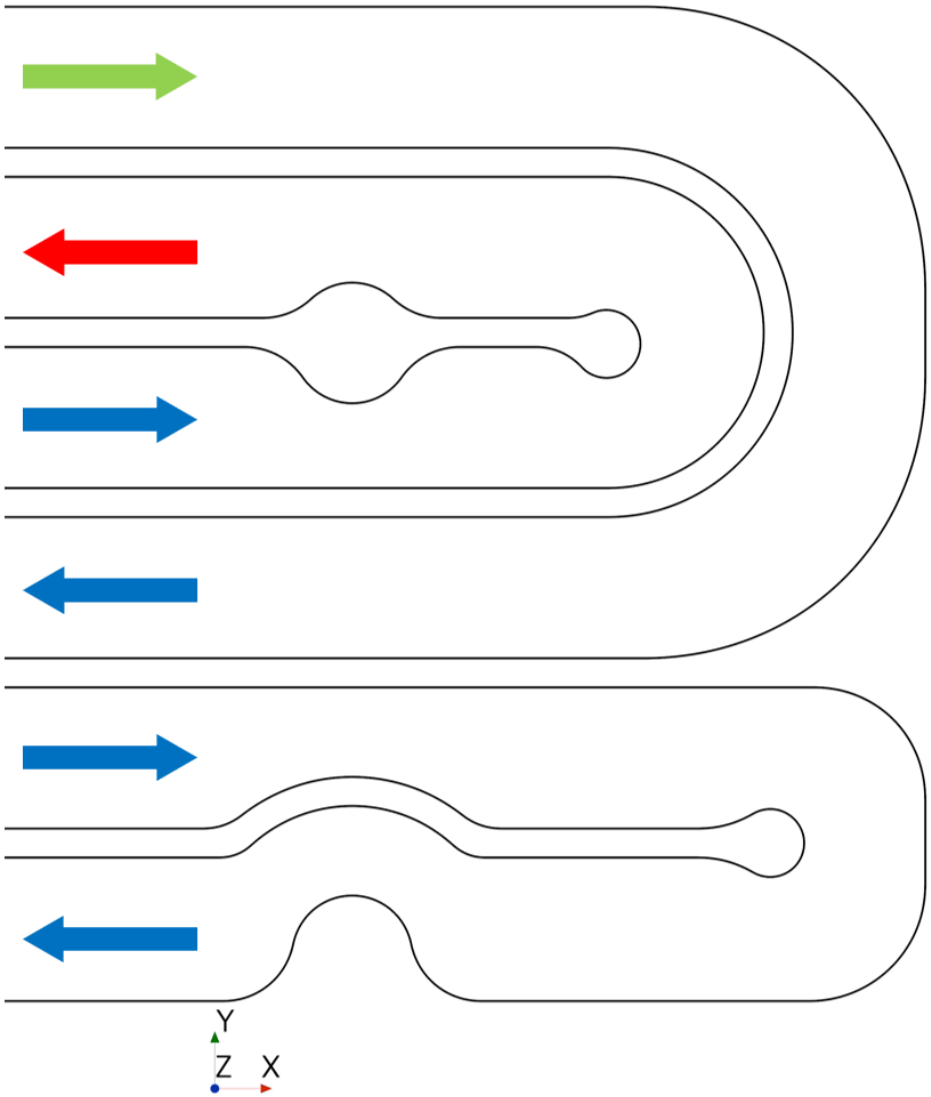

Figure 3.1: Portion of geometry of the cooling plate with flow direction in the different channels.

3.3.1 Boundary Conditions

Boundary conditions are set to replicate the high-flow degassing process observed in experimental setups. The applied conditions are:

- **Inlet:** A velocity inlet condition is applied, with the flow rate corresponding to a specified Reynolds number, equal to 1000, calculated using the inlet diameter as characteristic linear dimension. The inflow consists entirely of liquid coolant, with turbulence quantities such as intensity and viscosity ratio set based on experimental or empirical estimations.
- **Outlet:** A pressure outlet condition is imposed, with a fixed split ratio that allows both liquid and air phases to exit the domain without artificial constraints.
- **Walls:** No-slip boundary conditions are applied to all walls. A specified static contact angle is used to model the wettability of the channel material, influencing wall adhesion and bubble dynamics.

Table 3.1: Boundary conditions applied to the simulation domain.

Field	Inlet	Outlet	Walls
α (Volume Fraction)	Dirichlet	Neumann	Neumann
u (Velocity)	Dirichlet	Neumann	No-slip
p (Pressure)	Dirichlet	Neumann	Neumann

3.3.2 Initial Condition

Ideally, the simulation would begin with a fully air-filled cooling plate and simulate the complete filling process with coolant. However, this approach is computationally prohibitive due to the extended physical time required to simulate slow filling and the associated small time steps for interface tracking. To circumvent this, a practical initialization strategy is adopted.

The domain is initialized with air and coolant at rest, hence, with a zero-velocity field. The coolant occupies most of the volume, while discrete air bubbles are randomly distributed throughout the channel to mimic their expected configuration at the final stages of the real-world filling process. Figure 3.2 illustrates the initialized domain.

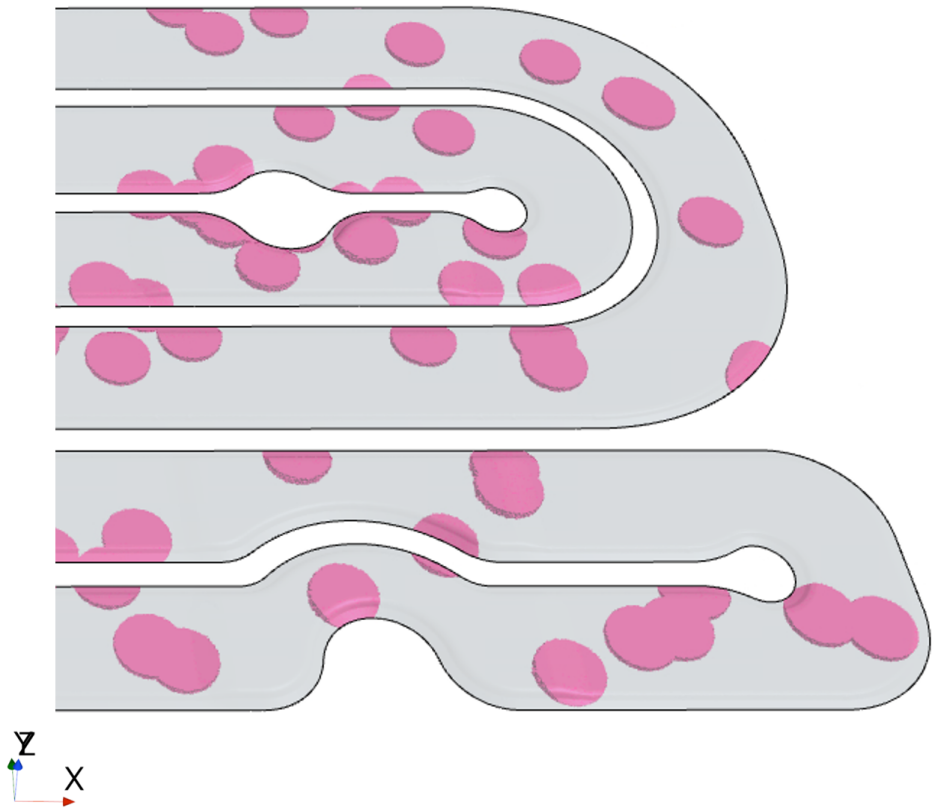

Figure 3.2: Initial distribution of air bubbles within the coolant domain. Air pockets are randomly placed to emulate late-stage filling conditions.

This initialization is achieved using a custom Java macro that generates spherical vol-

umes of pure air (volume fraction $\alpha = 1$) at random positions within the domain. This approximation reduces computational cost while still capturing the essential physics of bubble displacement and coalescence during the degassing process. Figure 3.3 illustrates the workflow of the custom code.

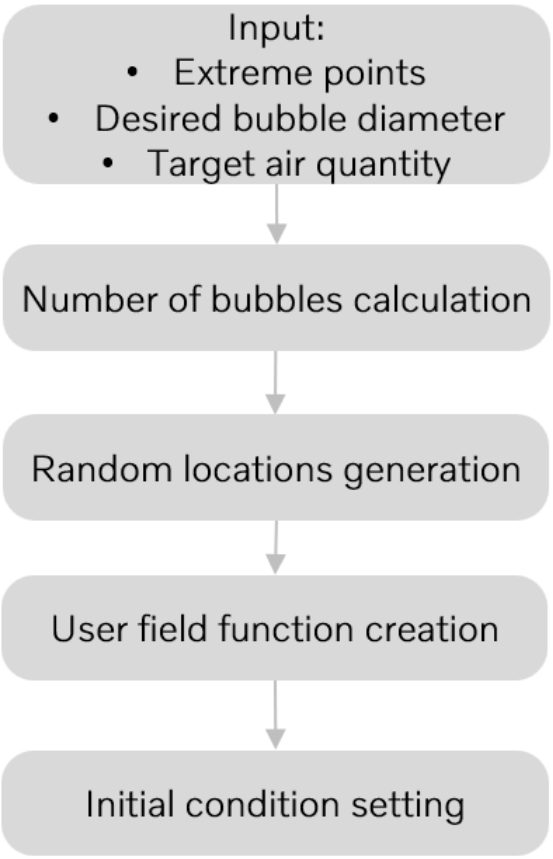

Figure 3.3: Workflow of the initial condition custom field function creation code.

The selection of the initial average air volume fraction within the domain was based on prior evaluations pertinent to this specific component. In addressing the uncertainty inherent in this estimation, the sensitivity of the results to variations in this parameter was examined.

Figure: 3.4 illustrates the difference in the results, in terms of air presence shown with a threshold on air fraction, on LES simulations with a different initial air fraction in the system.

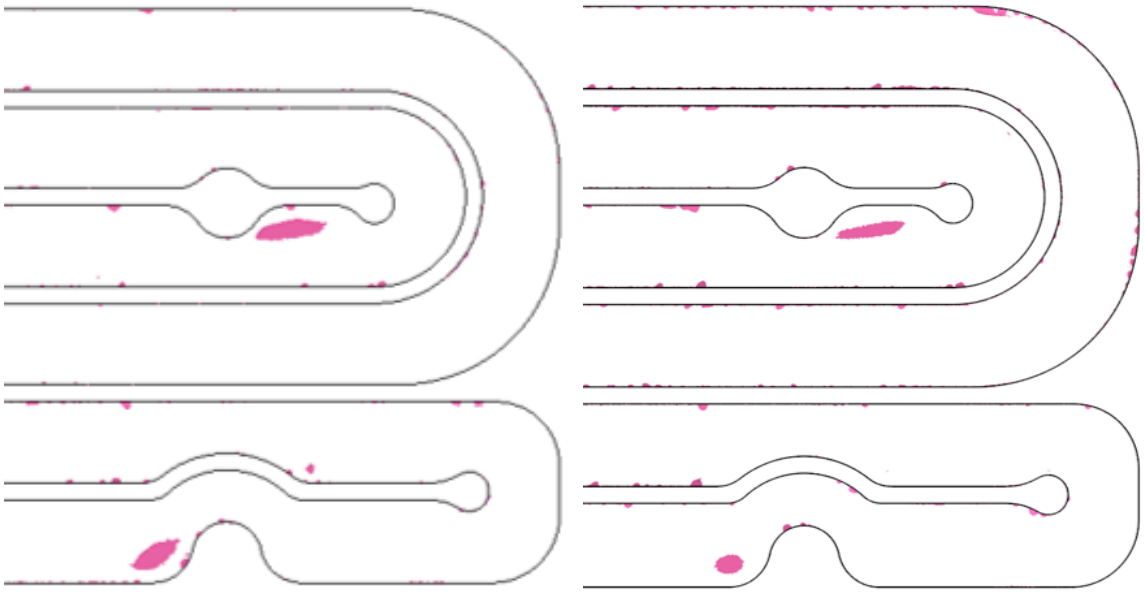

(a) 5% **(b)** 15%

Figure 3.4: Threshold of air fraction with different initial total fractions of air in the system.

It was found that, across the range of 0.05 to 0.15 in air volume fraction, the final outcomes consistently indicated air entrapment in similar locations, except for the inlet zone. In the inlet zone, given that the simulation begins with a fully liquid state, the quantity of air entrapped is statistically dependent on the stochastic nature of the proposed initial condition field for the volume fraction. The impact of this dependency on the results is minimal. Consequently, this study employed an initial average volume fraction of 0.05 for the domain, which mitigates computational complexity due to reduced turbulence compared to higher initial air quantities.

3.3.3 Solver and Temporal Settings

A segregated flow solver is used, with the pressure-velocity coupling handled through the SIMPLE algorithm for numerical stability. The Volume of Fluid (VOF) model with High-Resolution Interface Capturing (HRIC) is used for interface tracking between air and coolant. Gravity is included in the negative z-direction to capture buoyancy-driven bubble migration.

The simulations are conducted under unsteady flow conditions. The time step is selected based on the Courant number criteria to ensure stability and accurate interface tracking and on computational feasibility.

The implicit multistep approach is employed to execute a predetermined number of sub-steps in solving the volume fraction transport equation. This method facilitates a reduction in computational effort while preserving accuracy, particularly in scenarios where the resolution of the interphase between phases dictates the size of the simulation time-step. This is especially pertinent in applications where the overall flow velocity is low, as is the focus of the current study.

Table 3.2: Temporal Settings.

Parameter	Description
Time-step	0.0003 s
Volume Fraction Sub-steps	5
Temporal Discretization	1^{st} Order
Solution Algorithm	SIMPLE

3.3.4 Material Properties

The multiphase behavior is characterized utilizing the Volume of Fluid (VOF) methodology, involving two immiscible phases: air and coolant. The employed coolant consists of a water-glycol mixture, with its physical properties detailed in Table 3.3, alongside the properties of air utilized in the framework.

Table 3.3: Fluids properties for coolant and air.

Parameter	Coolant	Air	Unit
Dynamic viscosity (μ)	0.003802	6.57×10^{-5}	Pa·s
Density	1071.0	1.18415	kg/m^3

The properties used to characterize the phases' interaction and interaction with the walls are specified in Table 3.4.

Table 3.4: Multiphase properties for phases interaction.

Parameter	Value	Unit
Surface Tension	0.072	N/m
Contact Angle	90	deg

3.3.5 Meshing

To accurately resolve the coolant–air interface and flow near the channel walls, a polyhedral mesh is employed with local refinements in critical regions. This meshing strategy enhances computational efficiency while maintaining the fidelity required to resolve interface and wall-bounded flow behavior.

To capture boundary layer effects, prism layers are applied near all solid walls, allowing proper resolution of near-wall gradients and ensuring turbulence modeling accuracy.
Figures:3.5 and 3.6 show the top view of the mesh on the x-y plane, highlighting a higher density of mesh cells in thin areas to fully capture the complexity of the geometry.

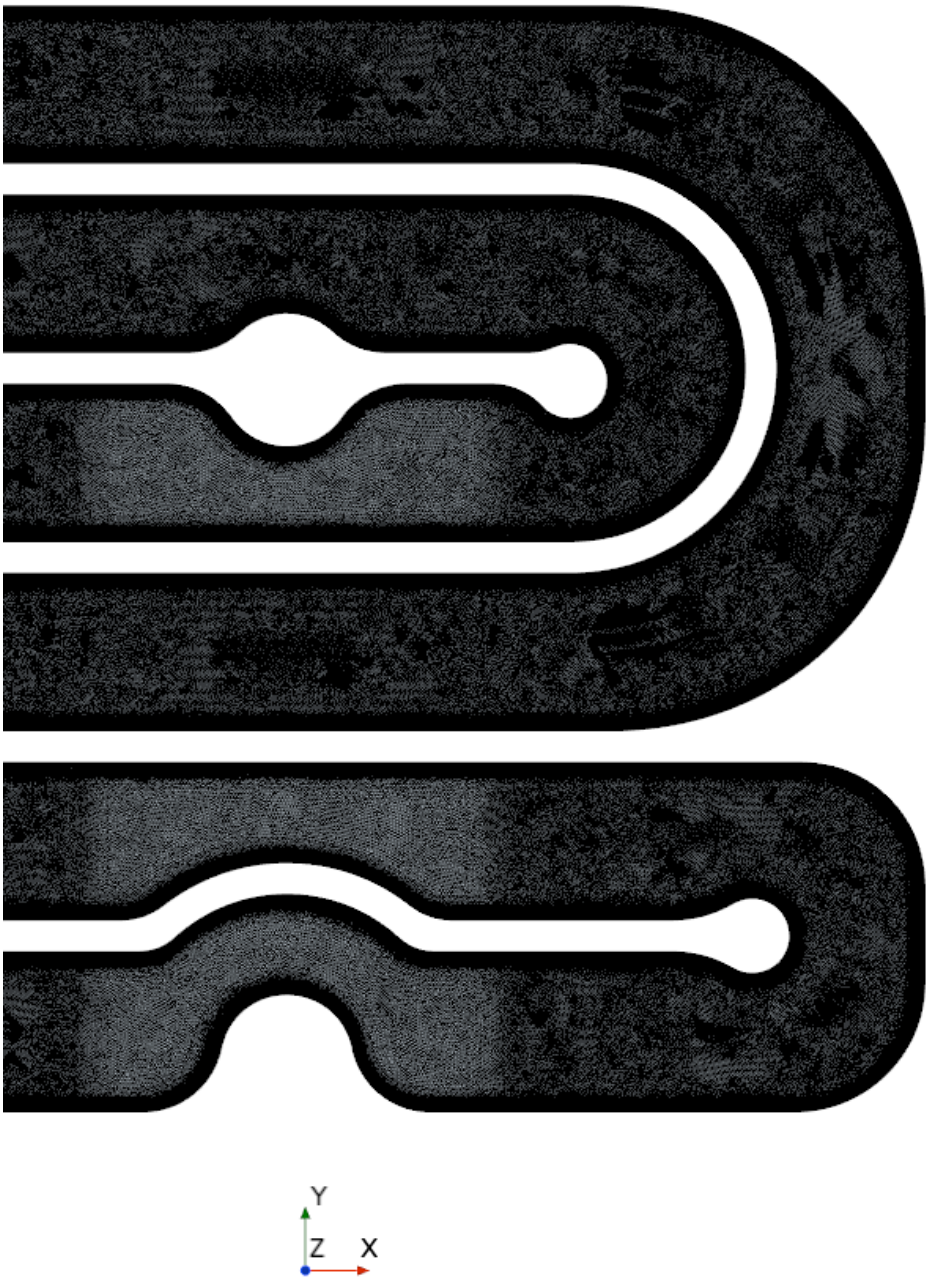

Figure 3.5: Top view of the mesh.

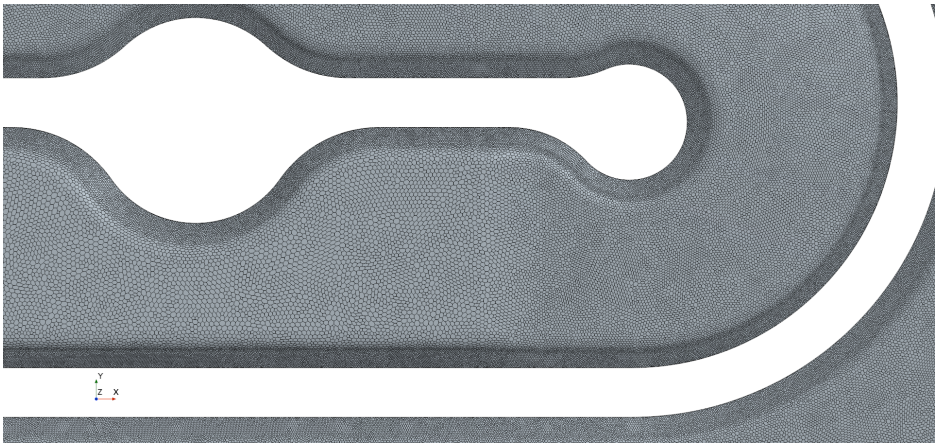

Figure 3.6: Close-up on the top view of the mesh.

A side view of the mesh on the x-z plane is not shown for confidentiality reasons. It should be specified the presence of variations in height within the geometry and a narrow margin at the periphery of the cooling plate. This boundary was meticulously processed using the ANSA software to ensure it is conducive to achieve high-quality meshing.

Figure 3.7 presents a lateral depiction of a mesh section on the x-z plane, highlighting the inclusion of prismatic cells, which are crucial for accurately resolving the boundary layer along the cooling plate walls. The geometry is segmented at the position corresponding to the outlet region.

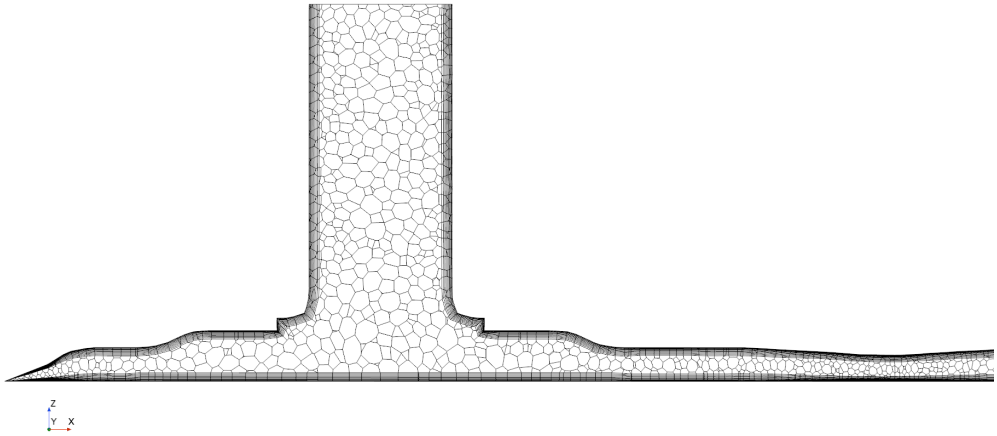

Figure 3.7: Section view of the mesh on the x-z plane on the outlet region.

A mesh independence study was conducted by analyzing the residual air volume at the end of the degassing process across different mesh densities. Convergence in air retention indicated mesh-independent behavior, ensuring numerical reliability. The final mesh utilized has a cell number of 40 millions.

The mesh quality is evaluated using the cell quality metric provided by STAR-CCM+, which combines Gauss and least-squares methods to assess cell gradients. Cell quality

values approach unity for ideal polyhedra and fall toward zero for distorted or degenerate elements. Cells with face quality below 1×10^{-5} are considered poor.

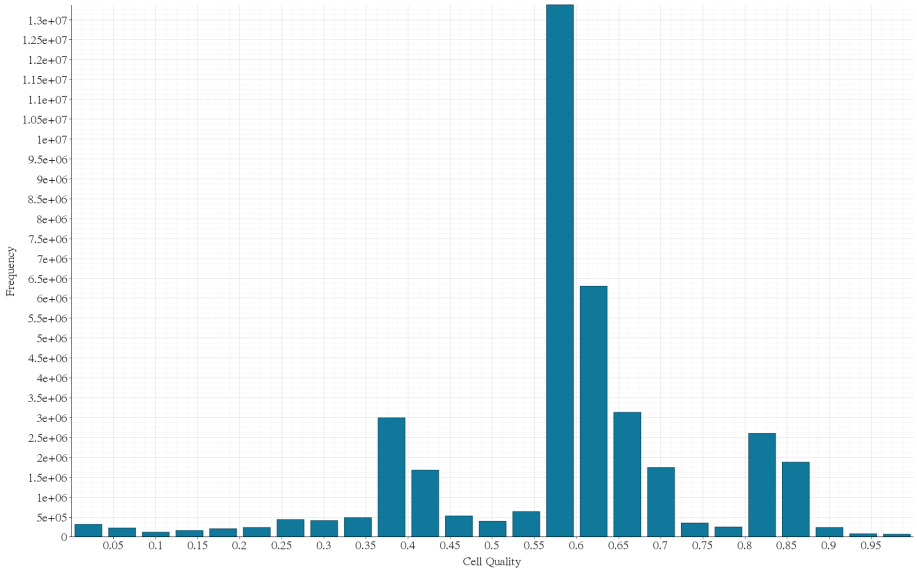

Figure 3.8: Histogram of cell quality metric across the domain.

Moreover, the evaluation of mesh skewness is conducted by examining the skewness angle, which is defined as the angle between the normal vector of the face and the vector that connects the centroids of adjacent cells. A skewness angle of zero indicates a perfectly orthogonal mesh. It is recommended to avoid skewness angles that exceed 85°.

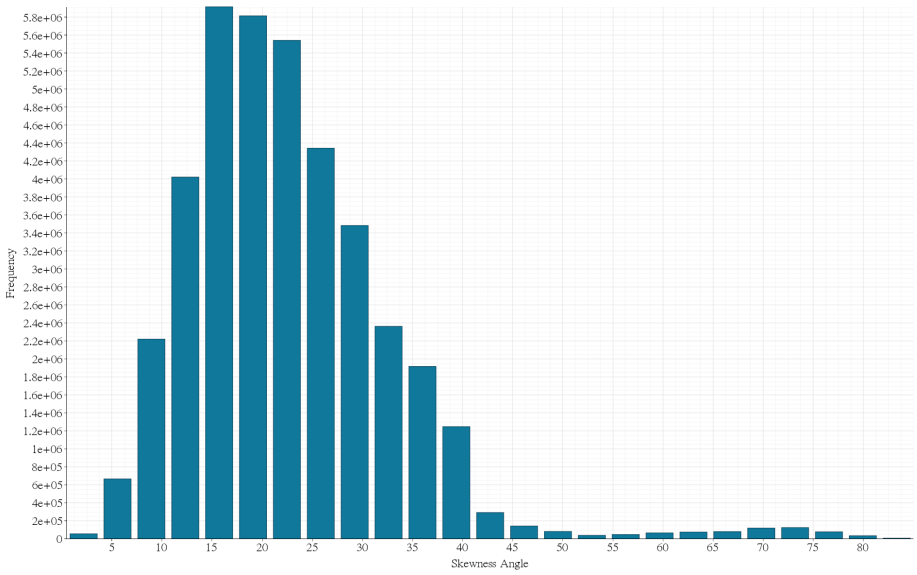

Figure 3.9: Skewness angle distribution.

Ensuring an accurate resolution of the boundary layer is of utmost importance, and this can be evaluated using the metric of y^+. It is characterized as the non-dimensional distance from a solid boundary to the initial grid point. The significance of the value of y^+ is particularly pronounced in scenarios involving wall-bounded turbulent flows. The y^+

parameter is mathematically delineated as:

$$y^+ = \frac{u_\tau \cdot y}{\nu} \tag{3.17}$$

where: u_τ represents the friction velocity at the wall, y denotes the distance from the wall to the first grid point, and ν signifies the kinematic viscosity of the fluid. Figure 3.10 shows the distribution of y^+ along the walls of the mesh.

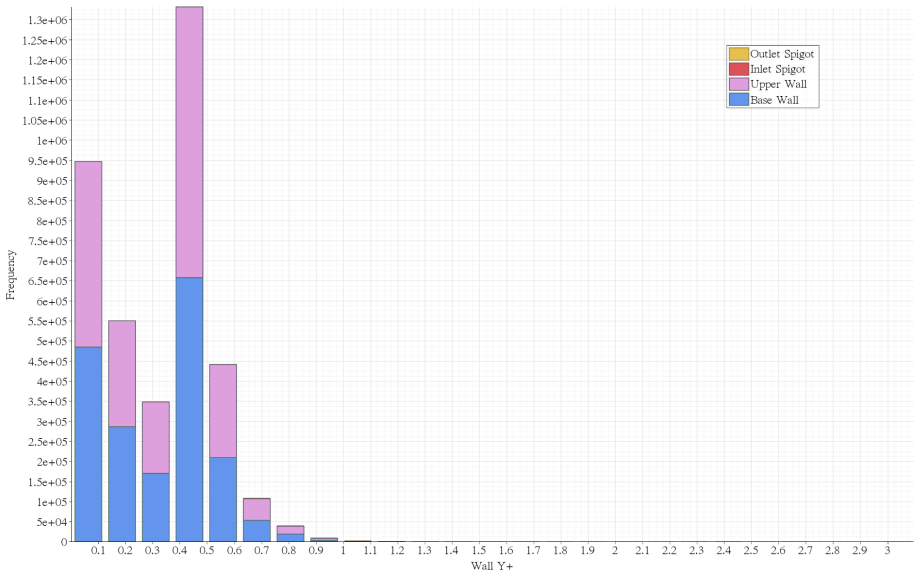

Figure 3.10: Wall-adjacent y^+ values.

3.4 End State Analysis

This study focuses on the quasi steady-state behavior of the system. Upon completion of the degassing operation, certain air pockets remain trapped within the system, which become the subject of analysis in this research. Acknowledging that the degassing process is not entirely efficient, it is thus crucial to establish a conclusive understanding of this procedure.

The method proposed for determining the final state of the flow is the Gas Liquid Ratio (GLR). When this value ceases to fluctuate over an extended period, it may be inferred that the quantity of air in the system will no longer decrease, implying that the air pockets will remain unremoved from the cooling plate. To identify this condition, a running average of the GLR was computed over a sliding window of size $N = 100$, as expressed in Equation 3.18:

$$\text{Running Average}_i = \frac{1}{N} \sum_{j=i-N+1}^{i} GLR_j, \tag{3.18}$$

where GLR_j is the gas-liquid ratio at the j-th time step, and N is the number of steps in the averaging window. The process is considered complete once the absolute change between successive running averages falls below a specified threshold, indicating that further re-

duction in air content is negligible.

Figure 3.11 illustrates the evolution of the process.It is important to highlight that the degassing process succeeds the filling process, which, as delineated in Section 3.3.2, involves the introduction of coolant into a cooling plate initially occupied solely by air. In this case, the filling process is not simulated; therefore, the time reported does not represent the filling time of the cooling plate, but rather the duration required to remove air from an initially low-air, fully filled system. It should also be noted that the initial condition of static flow may influence the length of the degassing phase.

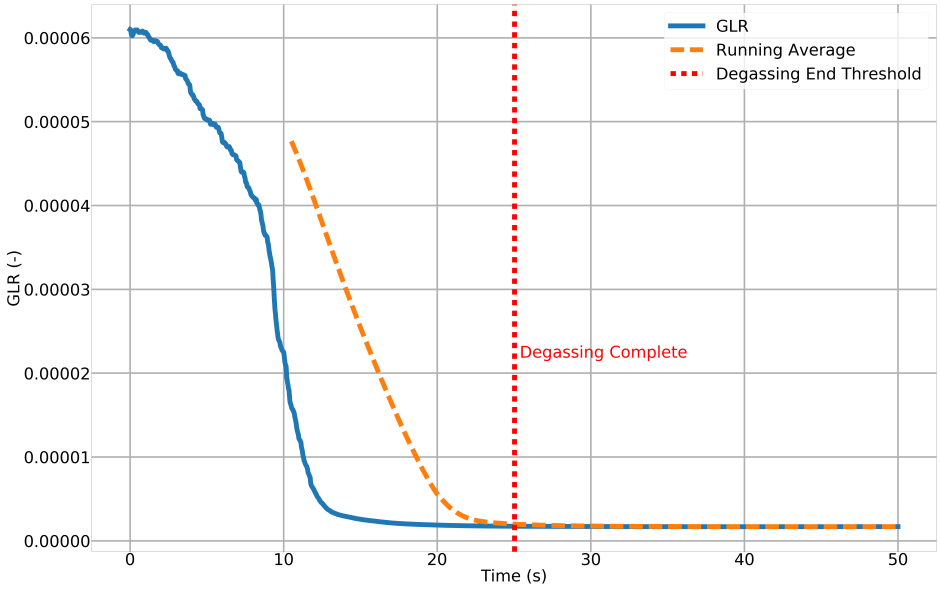

Figure 3.11: End-state detection using the running average of GLR. Degassing process is identified as completed at $t = 25.03\,\mathrm{s}$ based on a threshold of 10^{-9}.

Figure 3.11 presents the analysis conducted on the base case, LES simulation performed, with a coolant inlet flow rate equivalent to a Re of 1000. The analysis resulted in a conclusion of the degassing process after $t = 25.03\,\mathrm{s}$ seconds from the initial condition. The result was based on a threshold of 10^{-9} for the change of running average of GLR.

3.5 Grid Convergence Analysis

To ascertain the accuracy and dependability of the simulation outcomes, an analysis utilizing the Grid Convergence Index (GCI) was undertaken (Celik et al., 2008). This methodology assesses the discretization error by scrutinizing the results derived from three systematically refined mesh configurations. The respective total cell counts of these meshes were 10×10^6, 20×10^6, and 40×10^6, corresponding to the coarse, medium, and fine grid levels, doubling the total number of mesh cells as suggested by NASA (2021).

The refinement ratio between successive grids was set to $\sqrt[3]{2}$, as recommended in NASA (2021):

$$r = \left(\frac{\mathrm{N_{medium}}}{\mathrm{N_{coarse}}} \right)^{1/3} \tag{3.19}$$

where N represents the number of cells.

The parameter analyzed for the GCI study is the Gas Liquid Ratio (GLR) in the domain at the end state of the simulation, specified in Section:3.4.

Key quantities for the GCI analysis were calculated as follows:

- Apparent order of convergence:

$$P = \frac{1}{\ln(r)} \left| \ln\left(\frac{\epsilon_{32}}{\epsilon_{21}}\right) \right| \tag{3.20}$$

  where $\epsilon_{32} = \phi_3 - \phi_2$ and $\epsilon_{21} = \phi_2 - \phi_1$, with ϕ_i being the parameter of interest on the i-th grid.

- Extrapolated exact solution:

$$\phi_{\text{ext},21} = \frac{r^P \phi_1 - \phi_2}{r^P - 1} \tag{3.21}$$

- Approximate relative error:

$$e_{\text{app},21} = \frac{|\phi_1 - \phi_2|}{\phi_1} \tag{3.22}$$

- Grid Convergence Index (GCI):

$$\text{GCI}_{\text{fine},21} = \frac{F_s e_{\text{app},21}}{r^P - 1} \tag{3.23}$$

  where F_s is a safety factor, in this case 1.25 is used, as suggested by Celik et al. (2008).

The results of the GCI analysis are summarized in Table 3.5. The GLR showed consistent convergence across the meshes. The extrapolated solutions closely matched the fine mesh results, and the GCI values confirmed that the fine mesh provided grid-independent results.

Table 3.5: Grid Convergence Analysis for GLR.

Parameter	**Description**	**Value**			
r	Grid refinement ratio	$\sqrt[3]{2}$			
F_s	Safety factor	1.25			
		Coarse	Medium	Fine	Extrapolated
GLR	Gas to liquid ratio	2.9820e-06	2.0193e-06	1.8253e-06	1.7763e-06
P	Order of convergence	6.9320			
e_{app}^{21}	Approximate relative error	0.1063			
e_{ext}^{21}	Extrapolated relative error	0.0276			
GCI	Grid Convergence Index	0.0335			

The obtained results, with GCI values below 4%, demonstrate grid independence for the fine mesh, therefore, the final mesh utilized, as mentioned in Section 3.3.5, is the one with 40 million cells. Figure 3.12 illustrates the convergence of the GLR with increasing grid resolution.

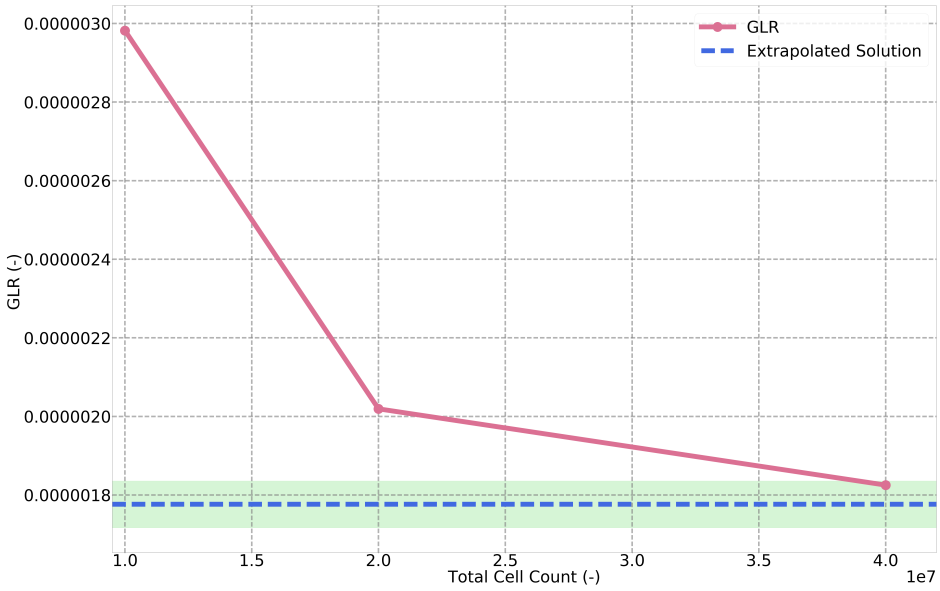

Figure 3.12: Convergence of GLR with increasing grid resolution.

3.6 Assessment of Resolved Turbulence Fraction in LES

In Large Eddy Simulation (LES), the turbulent flow field is decomposed into resolved large-scale motions and unresolved subgrid-scale (SGS) motions. The accuracy of an LES depends on the extent to which the turbulent kinetic energy (TKE) is captured by the resolved scales. A common criterion for an accurate LES is that at least 80–85% of the total TKE is resolved Lesieur and Metais (1996).

The resolved turbulence fraction, f_{resolved}, quantifies the proportion of TKE captured by the resolved scales and is defined as:

$$f_{\text{resolved}} = \frac{k_{\text{resolved}}}{k_{\text{resolved}} + k_{\text{sgs}}} \tag{3.24}$$

wherek_{resolved} is the resolved turbulent kinetic energy, and k_{sgs} is the subgrid-scale turbulent kinetic energy.

The resolved TKE is computed from the velocity fluctuations:

$$k_{\text{resolved}} = \frac{1}{2}\overline{u_i' u_i'} \tag{3.25}$$

Here, u_i' represents the fluctuating component of the velocity in the i-th direction, defined as:

$$u_i' = u_i - \overline{u_i} \tag{3.26}$$

where u_i is the instantaneous velocity and $\overline{u_i}$ is the time-averaged velocity component.

The SGS TKE, k_{sgs} is modeled as:

$$k_{SGS} = C_t \frac{\mu_t}{\rho} S \tag{3.27}$$

where k_{SGS} is the subgrid-scale turbulent kinetic energy, C_t is a model coefficient, μ_t is the turbulent eddy viscosity, ρ is the fluid density, and S is the magnitude of the mean strain rate tensor.

Figure 3.13 shows a histogram plot of the f_{resolved} in the domain, highlighting a high fraction of resolved eddies, underlining the accuracy of the results and the quality of the mesh used.

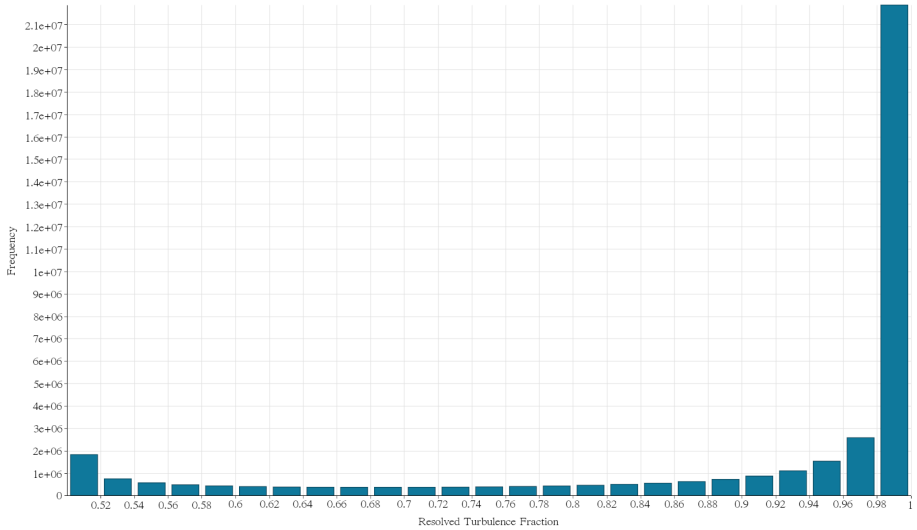

Figure 3.13: Histogram plot of resolved turbulence fraction (f_{resolved}) across the domain.

Regions where $f_{\text{resolved}} \geq 0.80$ indicate that the LES is resolving a sufficient portion of the turbulent energy, meeting the commonly accepted criterion for LES accuracy. Areas with lower values suggest that the mesh may be under-resolved, and additional refinement may be necessary to capture the relevant turbulent structures.

Evaluating the resolved turbulence fraction provides a quantitative measure of LES quality. The average f_{resolved} in the system resulted to be 0.82 indicating a sufficiently resolved portion of the turbulence in the flow.

Chapter 4

Validation

This chapter describes the experimental campaign carried out to validate the numerical model against physical observations, as well as the comparison with these observations. A transparent cooling-plate prototype was used to enable both qualitative and quantitative comparison of bubble dynamics.

4.1 Image Processing Methods for Bubble Detection

Optical imaging is widely used in experiments on gas-liquid flows, such as boiling heat transfer or liquid cooling, to measure bubble statistics (size, count, velocity) non-intrusively (Han et al., 2022). A typical processing pipeline involves separating moving bubbles from static backgrounds, segmenting them via thresholding, refining contours through edge detection, and applying morphological filters to enhance segmentation quality (Jensen et al., 2018), (Deng et al., 2022).

Classical image processing pipelines are commonly used for generating experimental reference data to validate CFD models, especially for air–liquid flows in cooling channels. Though machine learning methods are emerging (Zhou et al., 2023), traditional methods remain dominant due to their simplicity, transparency, and robustness in controlled lab setups.

4.2 Experimental Setup Description

Experiments were performed on a 1:1 transparent acrylic prototype replicating the geometry of the battery cooling plate model. Coolant (water–glycol mixture) was pumped in at controlled flow rates while video captured the motion and removal of air bubbles. Table 4.1 summarizes the main test parameters.

Table 4.1: Experimental setup specifications.

Parameter	**Value / Description**
Coolant Flow Rate Inlet Re	518
Transparent Prototype Material	Acrylic (PMMA)
Camera Model	GoPro Hero-7 Black
Frame Rate	24 fps
Resolution	1440 p (2560×1440 px)

In this application, the velocity of the bubbles is low, thus negating the necessity for a high-speed camera; consequently, utilizing a lower frame rate is advantageous to minimize the

data size.

The camera was mounted on a rigid tripod anchored to a pole to minimize vibration (Figure 4.1), and the prototype inlet was supplied with the minimum achievable air content to emulate degassing conditions. A reference background image (fully liquid flow domain) was recorded prior to the test to enable background subtraction during image processing.

Figure 4.1: GoPro Hero-7 camera mounted on a tripod.

4.3 Image Processing

A custom image processing pipeline was developed in Python to detect and size the air bubbles in each video frame. The workflow consists of the following steps:

1. **Grayscale conversion:** Each color frame is converted to grayscale.
2. **Image registration:** Key points on the cooling-plate geometry are detected, and each frame is aligned to the background reference to correct for camera motion.
3. **Background subtraction:** The registered frame is subtracted from the reference image to isolate bubbles.
4. **Thresholding and binarization:** A global threshold is applied to produce a binary mask of the bubbles.
5. **Masking of problematic areas:** A mask is applied on areas where the code would erroneously detect bubbles, such as light reflection areas.

6. **Morphological cleanup:** Small spurious regions are removed using opening and closing operations to improve bubble segmentation.

7. **Bubble detection and sizing:** Connected-component labeling identifies each bubble, and its equivalent diameter is calculated from the segmented area.

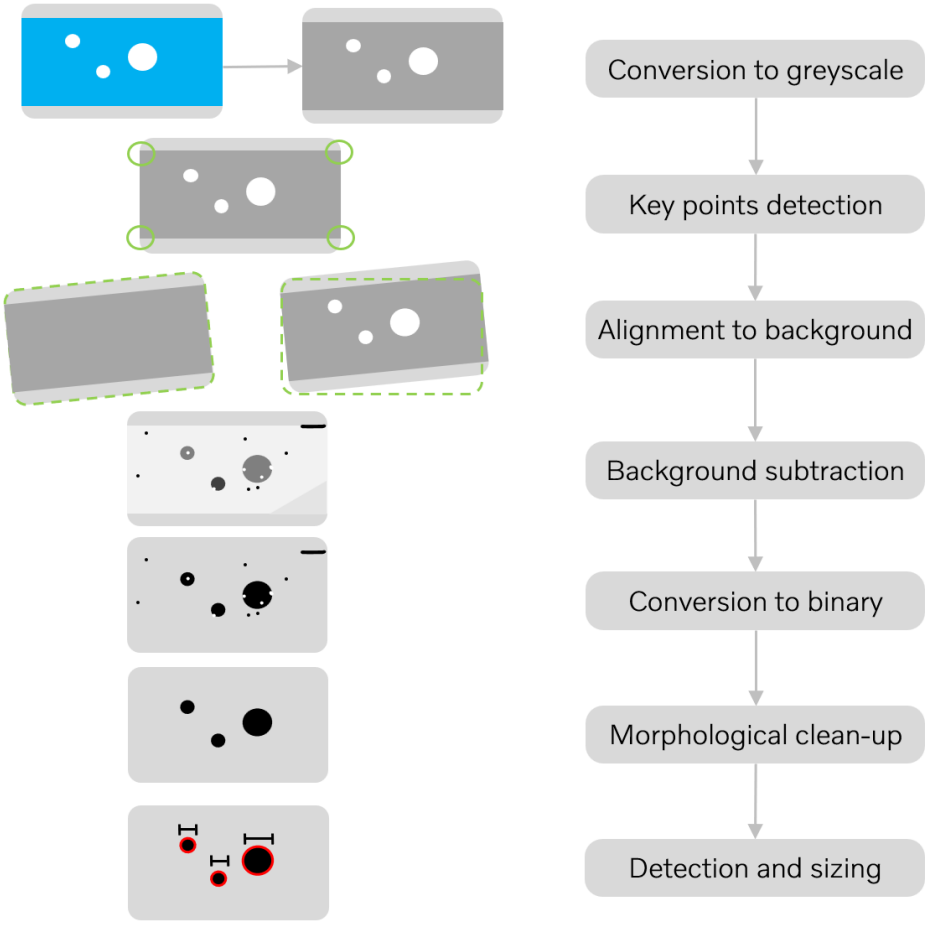

Figure 4.2: Workflow of the image processing code for image detection of each frame.

The background picture has been produced averaging the frames of a video with no ongoing flow and complete absence of bubbles. A condition of absence of air pockets has been realized by manually lifting the cooling plate on side to push the bubbles away of the area of study. This was necessary as considering the nature of the study, which focused on the analysis of air bubbles permanently trapped in the system, therefore imposing a difficulty in the removal of those to realize a feasible background picture.

Figure 4.3 shows the whole process of the bubble detection pipeline for a single frame of the experimental data, taken during the transient phase of the test. Figure 4.3a shows the image already converted to grayscale, aligned with the background following the structure key points, the problematic areas masked and the background subtracted. To take into account that the air pockets present a lighter color than the rest of the flow, the image is inverted. Figure 4.3b shows the result of imposing a grayscale value threshold to make the image binary. Figure 4.3c illustrates the change in bubble clarity after morphological

opening and closing. The morphological opening operation consists in erosion followed by dilatation to remove the smallest instances of air and, in this case, residuals of structure due to imperfect alignment of the image with the background. The morphological closing operation consists in dilatation followed by erosion to fill eventual gaps inside the bubbles. Figure 4.3d shows the corresponding ellipses to the detected bubbles on the colored image.

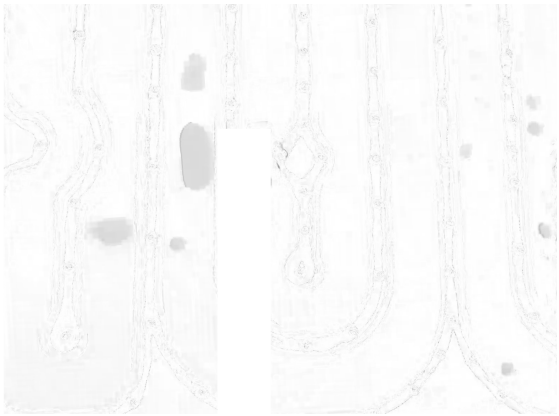

(a) Picture aligned, background subtracted and reflection masked.

(b) Binary picture through thresholding.

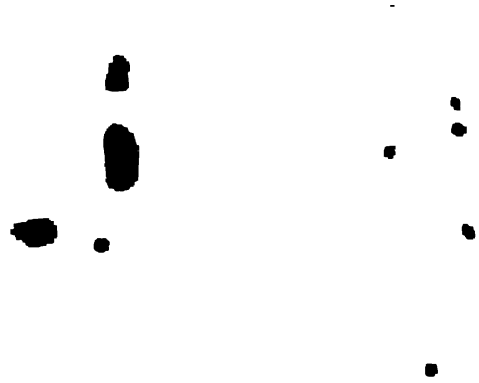

(c) Cleaned bubbles after morphological operations.

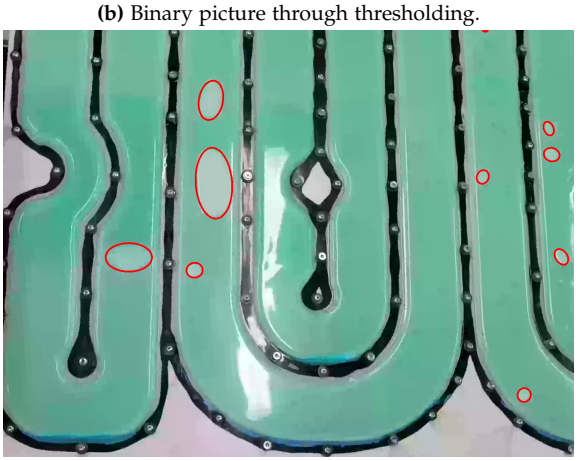

(d) Final result.

Figure 4.3: Overview of the image processing for bubble detection on a single frame.

Figure 4.4 shows the value of the pixels of: the gray scale of the original image, the gray scale of the average background and the image after subtraction of the background (labeled as "Subtracted" in the figure); highlighting the limited visibility of the bubbles in the experiment.

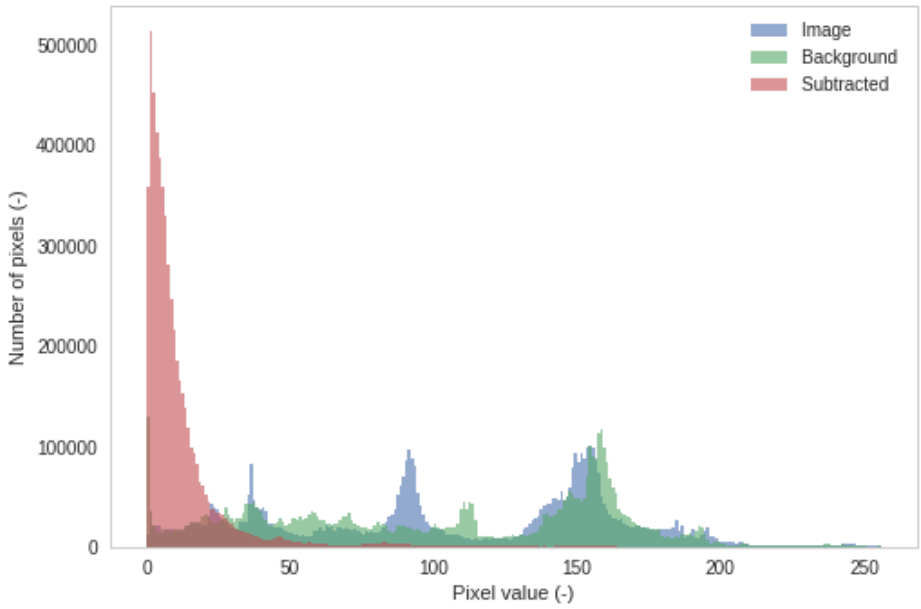

Figure 4.4: Intensity of gray in pixels before and after subtraction and of background.

Figure 4.5 presents the time averaged picture of the test, wherein detected bubbles are delineated during the quasi-steady state phase. For validation, areas exhibiting continuous non-stationary bubble flow, in addition to light reflections, have been obscured. These non-stationary bubbles can be seen in the form of extremely small bubbles creating a foam flow at the center at the bottom of the image. This masking was necessitated by the presence of a small, irreducible and unquantifiable amount of air at the flow inlet during testing, which were flowing continuously in the system without getting trapped. Given this study's emphasis on stationary bubbles retained within the systems, the analysis disregarded the transient bubbles in motion during the test. This was achieved by masking the areas where this bubbles were still recognizable in the time averaged image of the test.

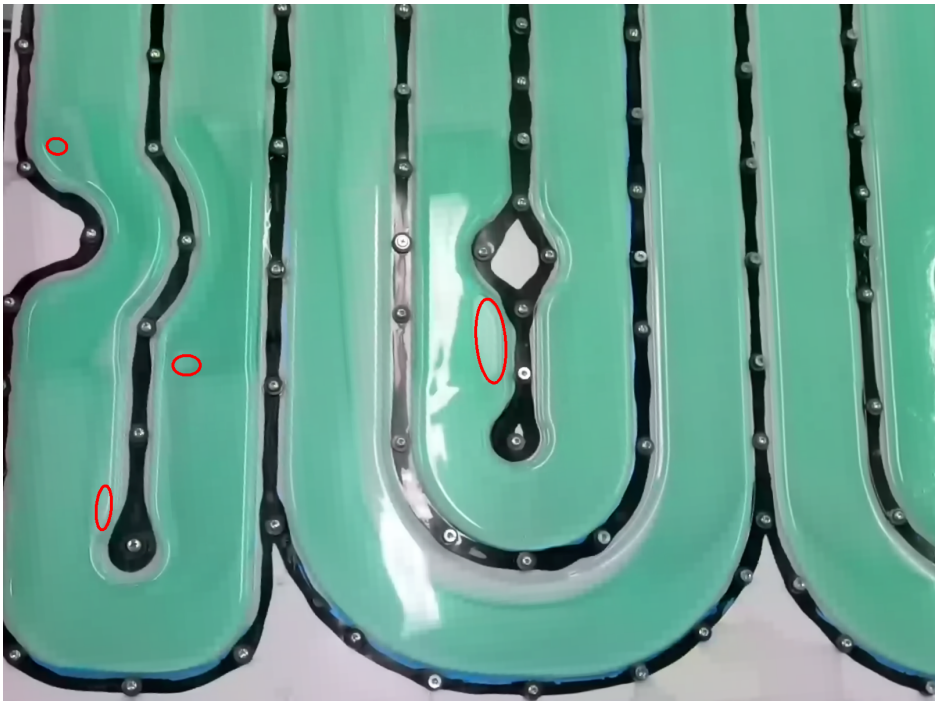

Figure 4.5: Image-processing result: detected bubbles (red outlines) overlaid on the time-averaged frame.

The experimental protocol began with the partial filling of the cooling plate, establishing the initial condition. This was succeeded by a transient phase in which most of the air within the cooling plate was expelled from the system. Subsequently, a quasi-steady state phase was observed, characterized by bubbles within the system becoming entrapped and remaining stationary, except for certain air introduced from the coolant pumping apparatus which continued to move through the domain. Only the quasi-steady state phase was employed for measurement to validate the simulation data.

Owing to preceding damage sustained by the transparent prototype employed in the experiment, it was not feasible to conduct multiple testing sessions, thus rendering it impractical to generate statistically independent data. The results are coherent with a prior test on the same component, suggesting consistency on the air pockets positions.

To quantitatively compare experiments and simulations, the metrics extracted from the processed images and CFD results of Bubble size distribution and positions were used. These metrics serve to assess the model's predictive capability in terms of final degassing efficiency.

4.4 Experimental Uncertainties and limitations

Several issues were faced during the testing of the degassing process:

- **Vibration in the test:** The test setup used is subject to vibration, which implies a slight movement of the camera during the data acquisition.
- **Light reflection in the test:** The transparent prototype employed in the test is strongly

reflective, and an optimal light condition was not realized during the test, resulting in light reflections visible in the data.

- **Limited resolution of the camera in the test:** The camera use to acquire the experimental data has a lower resolution than what would be ideal for this type of experimental application.
- **Single instance of test performed:** The transparent component employed in the test was damaged, making it impossible to repeat the test multiple times in order to acquire statistically independent data from initial condition and other factors.
- **Partially gaseous inlet:** It was impossible to remove the totality of air from the coolant circulation system, resulting in a non fully liquid inlet flow, with a non-quantifiable amount of air.

4.5 Simulation Results

A simulation replicating the test conditions was conducted to validate the model by assessing the quasi-steady state of flow concerning air pockets stagnating within the cooling plate channels. The experimental data is constrained by the two-dimensional nature of the video recordings, which precludes the acquisition of information regarding the total quantity of air in the system. Consequently, a comparative strategy involving the simulation was necessitated. The proposed method involved applying the same bubble detection algorithm utilized in the experimental data analysis to the simulation outcomes. This approach facilitates the acquisition of analogous information from both test and simulation, thereby enabling a comparison of the results.

In light of the transient characteristics inherent in the simulation and testing processes, temporally averaged imagery has been employed for validation purposes. Within the simulation context, visualization is performed using an air volume fraction threshold. The images generated during the simulation's quasi-steady state have undergone temporal averaging, with the resultant image presented in Figure 4.6.

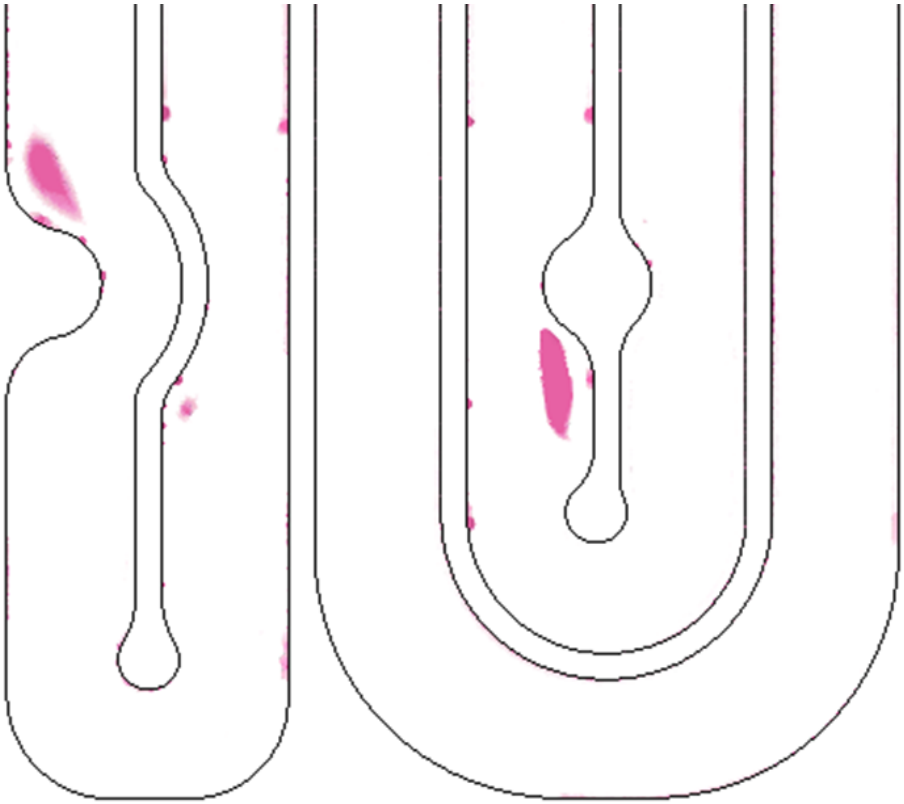

Figure 4.6: Time averaged threshold surface of air fraction in the system.

4.6 Comparison of results

To ease the identification of the bubbles, they have been numbered in Figure 4.7, that shows a numbering for the locations where the bubbles are trapped, both for the simulation and test. The figure also shows the flow direction in the passages.

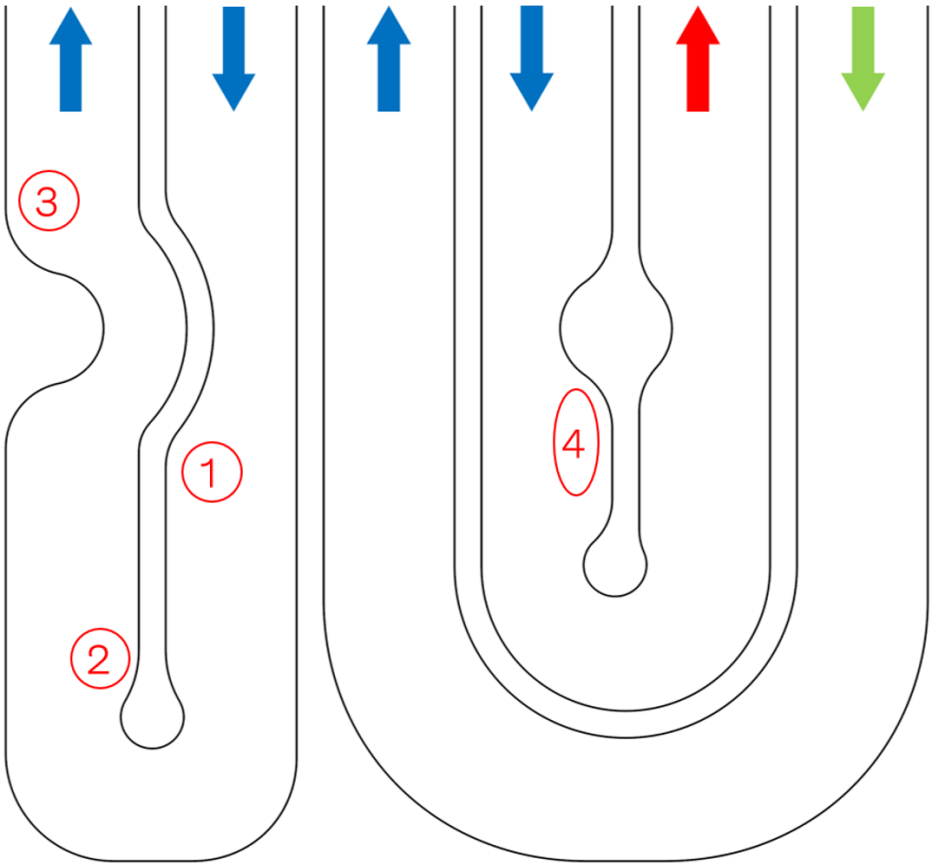

Figure 4.7: Numbers for identification of bubbles.

The dimensions of the resulting large bubbles have been evaluated. Figure 4.8 highlights a strong correlation between the experimental measurements and the simulation regarding the diameters of detected bubbles. The primary discrepancy observed is the absence of one bubble, the bubble numbered as number 4, in the simulation that was identified in the experimental data. This inconsistency is ascribed to the low resolution of the test data images, which leads to suboptimal detection of air.

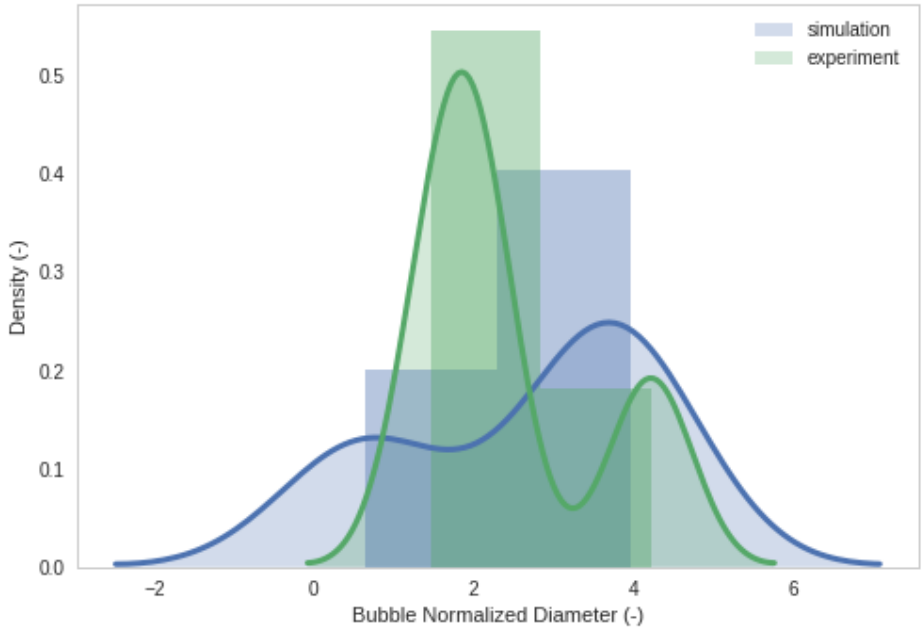

Figure 4.8: Density of normalized bubble diameters comparison in test and simulation results.

Besides the size of the bubbles, the positions of the identified bubbles constitute another critical aspect of analysis. Figure 4.9 illustrates both the position and the dimension of the detected air pockets, underscoring a substantial correlation between the experimental observations and simulation outcomes. The dimensions of the scatter points within the plot correspond to the size of the bubbles, expressed in terms of the calculated relative diameter. This metric is defined as the diameter of a hypothetical circular bubble possessing an equivalent total area to that of the actual bubble observed. It is noteworthy that the camera alignment during the test was not perfectly aligned with the cooling plate; thus, there exists some uncertainty in the positional results of the detected bubbles due to imperfect warping adaptation. The findings indicate that bubble number 4 was observed in almost identical positions and with comparable dimensions in both the simulation results and the experimental data; this bubble also exhibited the highest visibility during the experiment. Bubble number 3 was located in a similar position in both contexts, although it demonstrated a greater dimension in the simulation compared to the experimental observations. Conversely, bubble number 1 was found in a consistent position but displayed a larger diameter during the experimental test. Finally, as previously mentioned, bubble number 2 was identified in the experimental test but was absent in the simulation results.

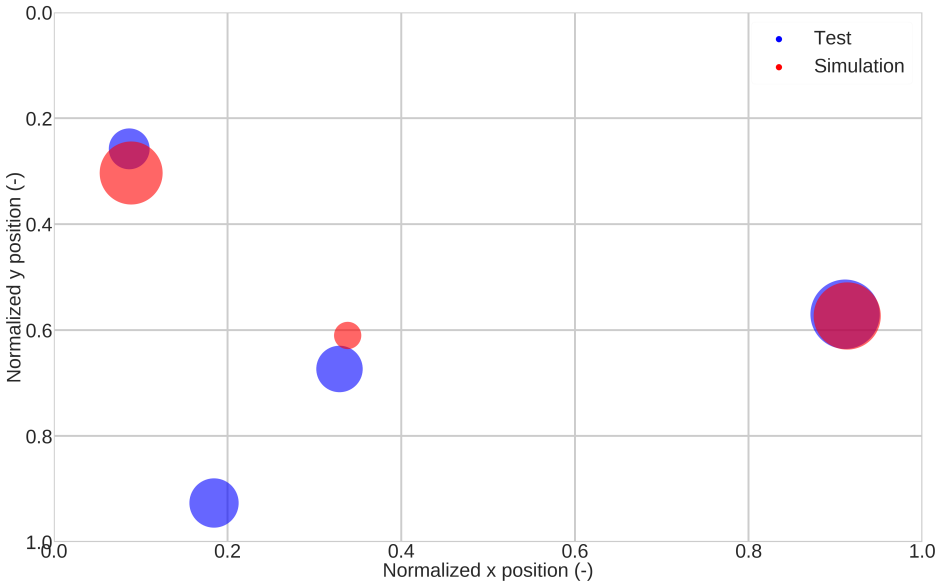

Figure 4.9: Scatter plot of detected bubbles positions sized by bubble diameter in the test and simulation results.

An additional parameter for comparison is the quantification of total air amount, derived from a two-dimensional estimation, thereby reflecting the area occupied by air within both the experimental and simulation datasets. This comparative analysis has been conducted by examining the ratio of the air-occupied area to the total study area. This analysis yielded a 0.567% of air in the experimental data and a 0.568% in the simulation results. These values strongly indicate a significant correlation in the assessment of air entrapment within the cooling plate.

The assessment of the experimental data against the simulation results indicates that the simulation model accurately represents the real scenario with sufficient precision, thereby warranting confidence in its use for further analysis.

Chapter 5

Simulation Performance Improvement Study Results

In this chapter the efforts on analysis of different simulation approaches for the identification of entrapment areas in cooling plates are illustrated. All the simulations have been performed on 640 cores on the same machine to correctly compare the resulting computational efforts.

This chapter employs a bubbles enumeration analogous to that utilized in Chapter 4 to facilitate an objective discussion of specific bubbles, as depicted in Figure 5.1 for enhanced accessibility. This figure also aids in elucidating the flow direction in the various passages.

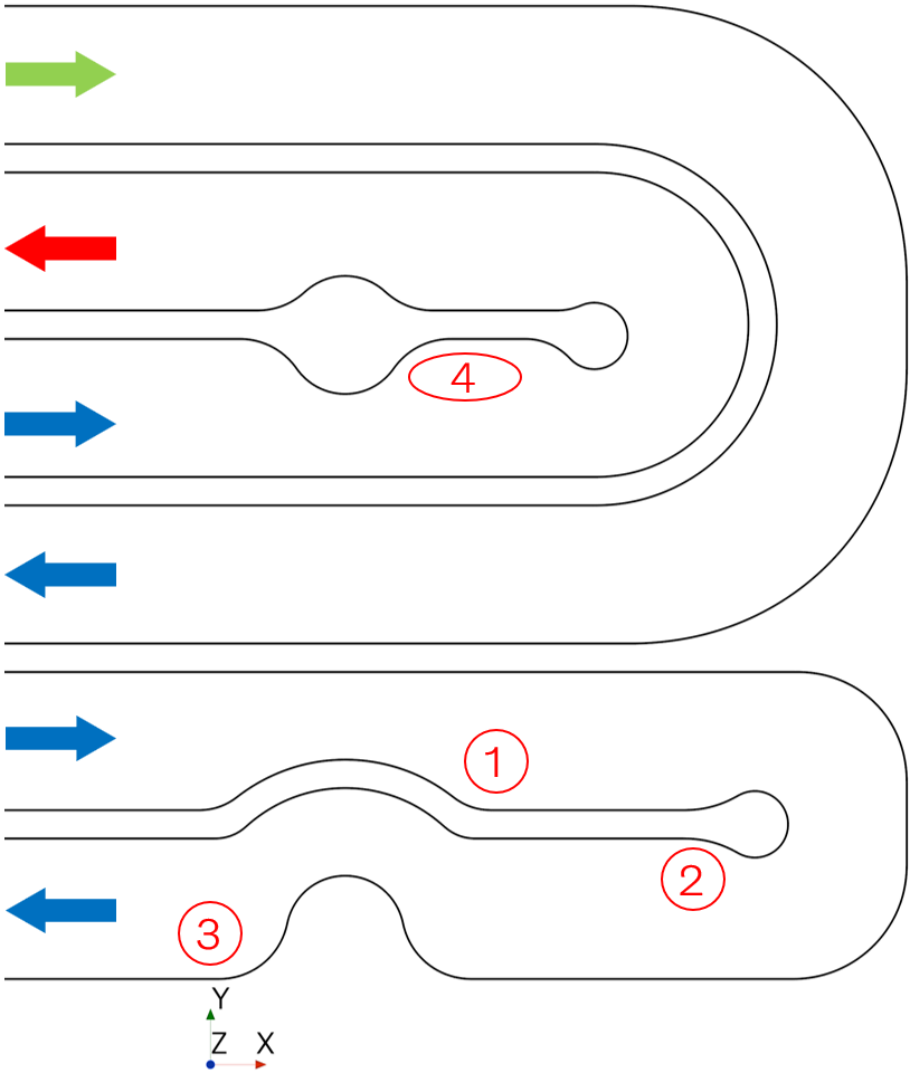

Figure 5.1: Numbers for identification of bubbles.

5.1 Turbulence modeling approach comparison

Different approaches for turbulence modeling have been proposed to analyze its impact on the results and computational effort as mentioned in Section: 3.2.2. Namely URANS, LES and DES simulations have been carried out.

URANS commonly requires a less refined mesh relative to LES, the present conditions, which demand a more detailed grid for the accurate resolution of phase interfaces, indicate—according to the analysis presented in Section: 3.3.5, particularly with respect to the y+ values along the walls, and further informed by the evaluation of the fraction of resolved turbulence in Section: 3.6—that the initially proposed mesh configuration is suitable for undertaking LES simulations.

All simulations were conducted utilizing a consistent mesh of 40 millions cells, in accordance with the details provided in 3.3.5. The equivalence of solution times across the three distinct turbulence modeling techniques was an unexpected outcome. This result primarily stems from the uniformity of the mesh employed, and also implies that the computational intensity was predominantly associated with the volume fraction solution.

Figure 5.2 illustrates the volume fraction of air above the cooling plate as determined by three distinct turbulence modeling techniques. The figure reveals consistent bubble entrapment locations across the models, indicating common shortcomings in this respect. The URANS model exhibits a slightly displaced position for bubble number 3, which is situated at a higher position along the y-axis in comparison to that observed in the LES and DES models. Moreover, bubble number 1 is observed to be larger in the URANS model than in the other simulations.

It is important to acknowledge that, given the dual nature of the Detached Eddy Simulation (DES) method—functioning as a Large Eddy Simulation (LES) when the mesh resolution is sufficiently fine, and as an Unsteady Reynolds-Averaged Navier-Stokes (URANS) method when the mesh is coarser—the DES predominantly operates as a LES within simulations where the mesh permits LES feasibility. Consequently, it yields results that closely correlate with those obtained via the LES approach.

Overall, the three approaches presents similar results, underlining the validity of all the three different approaches for the identification of bubbles entrapment areas in cooling plates geometries.

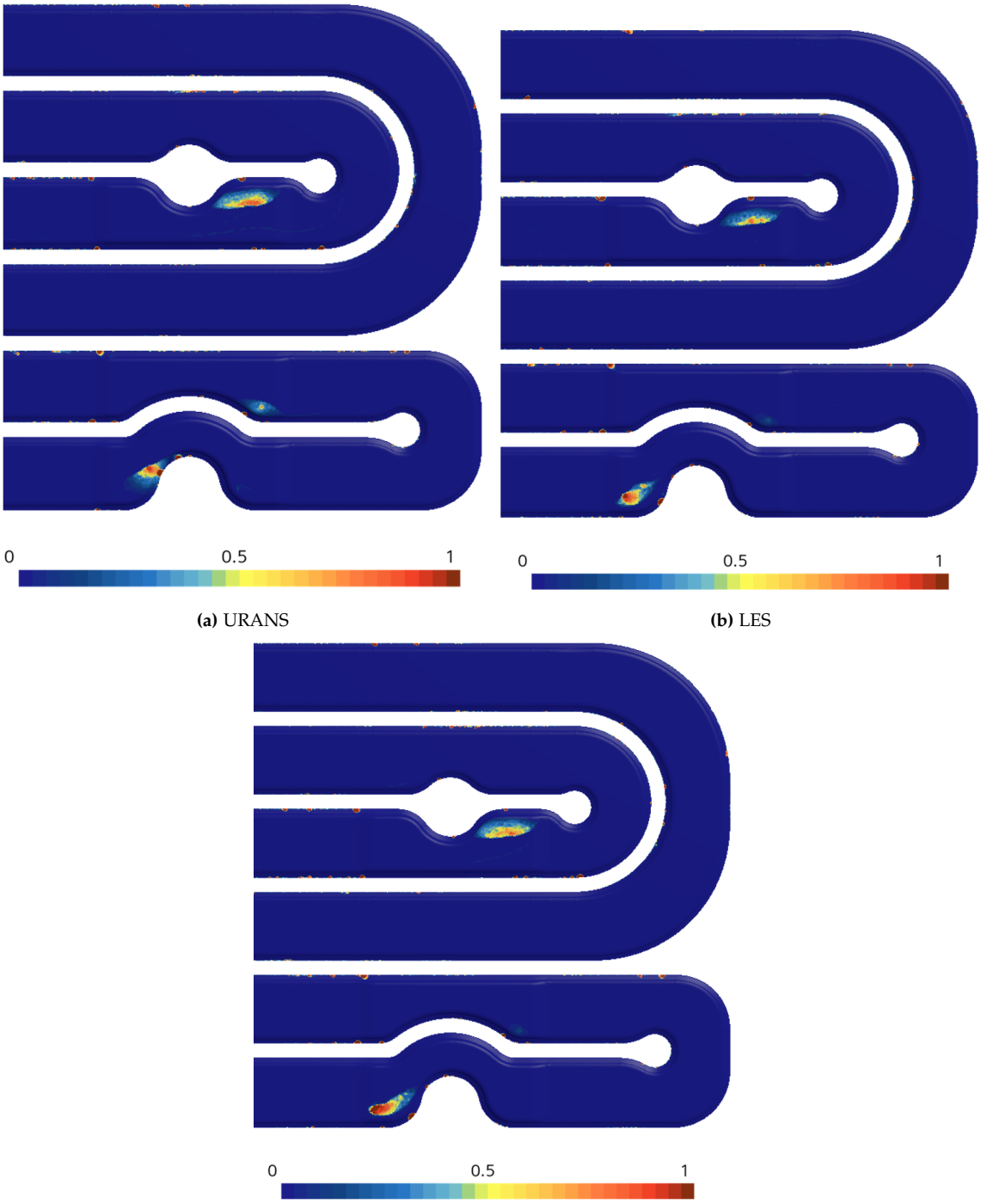

(a) URANS **(b)** LES

(c) DES

Figure 5.2: Top view of the cooling plate, colored by air volume fraction in different turbulence modeling approaches.

Figure 5.3 illustrates the resultant threshold of air volume fraction across the entire cooling plate, as determined by three distinct turbulence modeling approaches. This depiction elucidates the correlation between the comprehensive air distribution within the system and a top-down perspective.

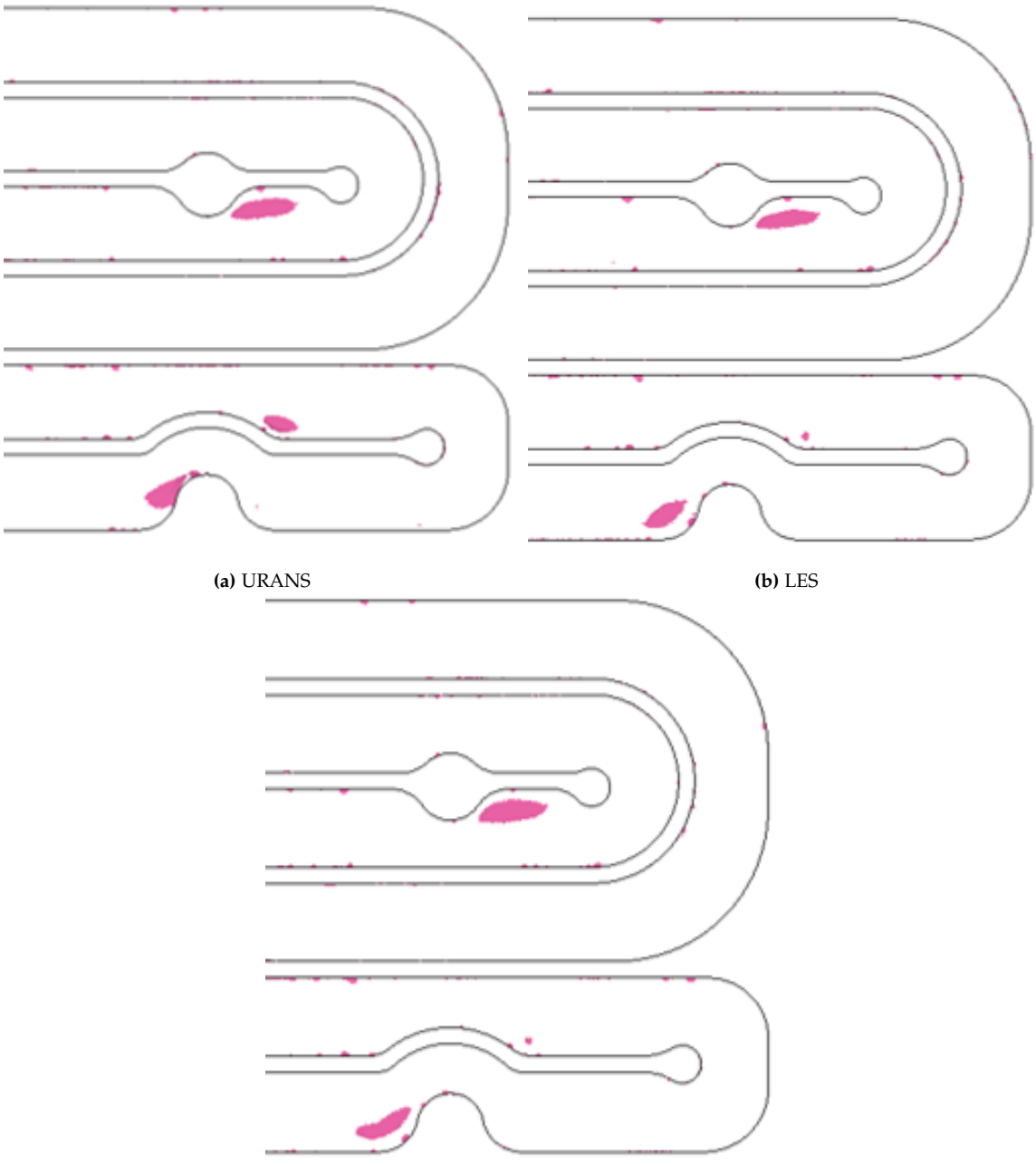

(a) URANS **(b)** LES

(c) DES

Figure 5.3: Top view of the cooling plate, highlighting the areas with air volume fraction higher than 0.1 in different turbulence modeling approaches.

In this particular application, the LES approach is posited as the most suitable choice due to its inherently superior accuracy relative to other alternatives, factoring in the absence of elevated computational expenses in comparison to expectations. It should be noted that in analogous applications, varying levels of turbulence may be present in the cooling plate, potentially rendering it less feasible to accurately execute an LES simulation with the same mesh as would be employed for URANS. Consequently, DES may generally represent a safer option for analyzing diverse geometries of cooling plates.

5.2 Adaptive Mesh Refinement (AMR)

Adaptive Mesh Refinement (AMR), when integrated, can enhance interface resolution while minimizing computational cost.

AMR dynamically adjusts the computational mesh during simulation to increase resolution in regions of interest, typically near the gas-liquid interface, while coarsening the mesh elsewhere. In VOF-based degassing models, AMR is particularly valuable for capturing complex interface dynamics such as bubble nucleation, coalescence, and breakup. The refinement strategy is often driven by gradients in the volume fraction field, ensuring that sharp interface features are retained without excessive grid density elsewhere (lin Yan et al., 2025).

The Free Surface Mesh Refinement (FSMR) approach is a specialized AMR criterion tailored for VOF simulations. It identifies interface cells based on the magnitude of the volume fraction gradient and refines the mesh downstream (and optionally upstream) of the predicted interface location. This anticipatory refinement ensures that as gas bubbles grow and migrate through the coolant, the interface remains sharply defined, avoiding numerical diffusion and maintaining mass conservation.

A sub-cycling time-stepping strategy is employed during AMR transport steps to handle high Courant numbers that might otherwise destabilize the solution. Interpolation methods are also crucial when transferring variables (pressure, velocity, volume fraction) between coarse and fine grids, with static pressure corrections and stencil-based velocity interpolation helping maintain numerical consistency (lin Yan et al., 2025).

Overall, integrating AMR with VOF allows for high-fidelity simulation of degassing phenomena in EV battery cooling plates, possibly without prohibitive computational overhead. This can enable better prediction of venting paths, coolant displacement, and potential thermal hotspots, insights critical to optimizing thermal design and enhancing safety.

5.2.1 Results

Table 5.1 summarizes the options selected for the adaptive mesh refinement workflow. For this simulation, a coarser base mesh has been utilized to then be automatically refined in the areas of interphase between the faces; the mesh used had a base mesh cells number of $10e6$, and turbulence modeled through URANS.

Table 5.1: Adaptive mesh refinement properties.

Parameter	Description
Adaptive Mesh Criterion	Free Surface
Max Refinement Level	2
Mesh adaptation frequency	10 time-steps

The duration necessary for the simulation to attain a quasi-steady state was consistent with prior results, $16h$, akin to simulations employing a fixed mesh configuration. This is

attributed to the requisite time for mesh refinement in correspondence with the dynamic free surface of the bubbles every few time steps.

Figure 5.4 presents a top view of the cooling plate, annotated by the air volume fraction, under the conditions of adaptive mesh refinement. It is evident from the illustration that bubbles manifest in locations closely mirroring those recorded in the baseline simulations, thus emphasizing identical geometric features as problematic regarding air entrapment. The interface in this simulation is notably more defined, as indicated by the increased air volume fraction within the bubbles and an abrupt transition at their boundaries. This enhanced definition of the interface is attributed to the employment of a finer mesh in these areas relative to the mesh employed in simulations with a constant mesh.

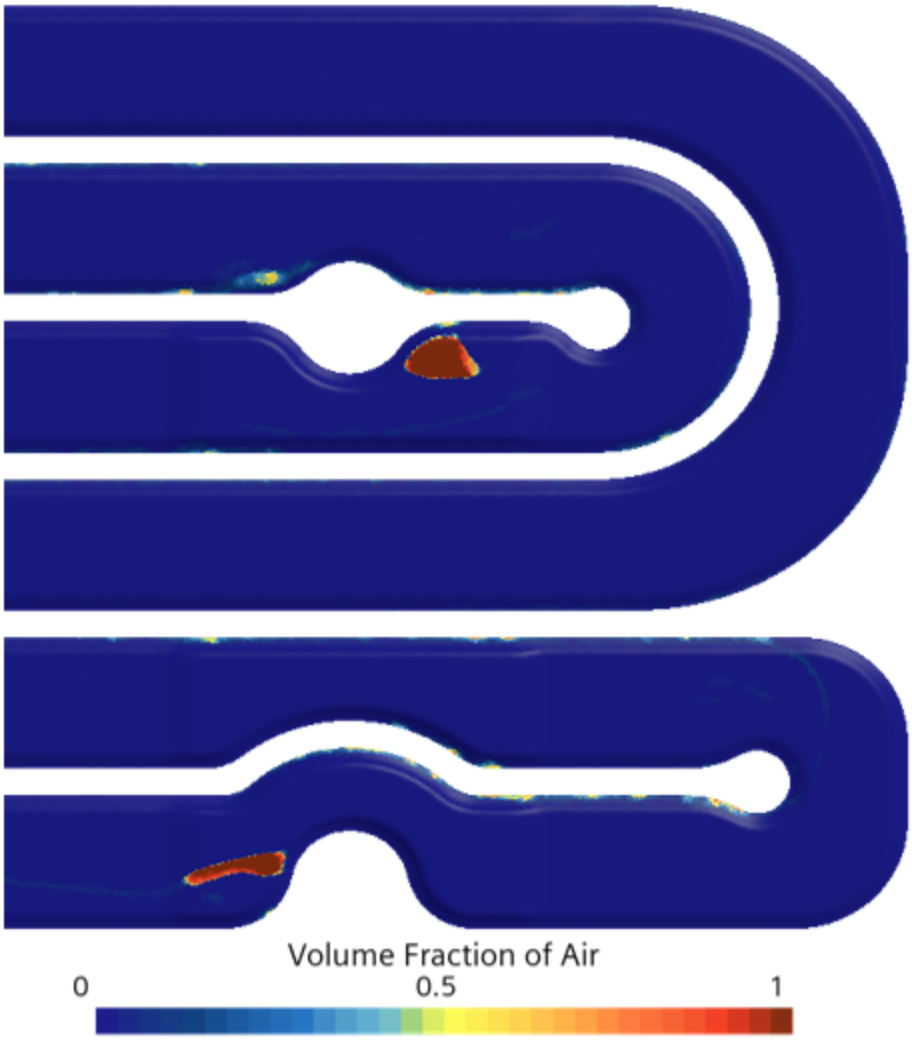

Figure 5.4: Top view of the cooling plate, colored by air volume fraction with AMR.

Figure 5.5 reports the same view as Figure 5.4 but in the base case of fixed mesh for easier comparison.

Figure 5.5: Top view of the cooling plate colored by air volume fraction with a fixed mesh.

Figure 5.6 presents a top view of the cooling plate, where coloration by air volume fraction is employed alongside a visible mesh to emphasize the refinement on the free surface at the interface between phases. The figure is magnified to enhance visualization.

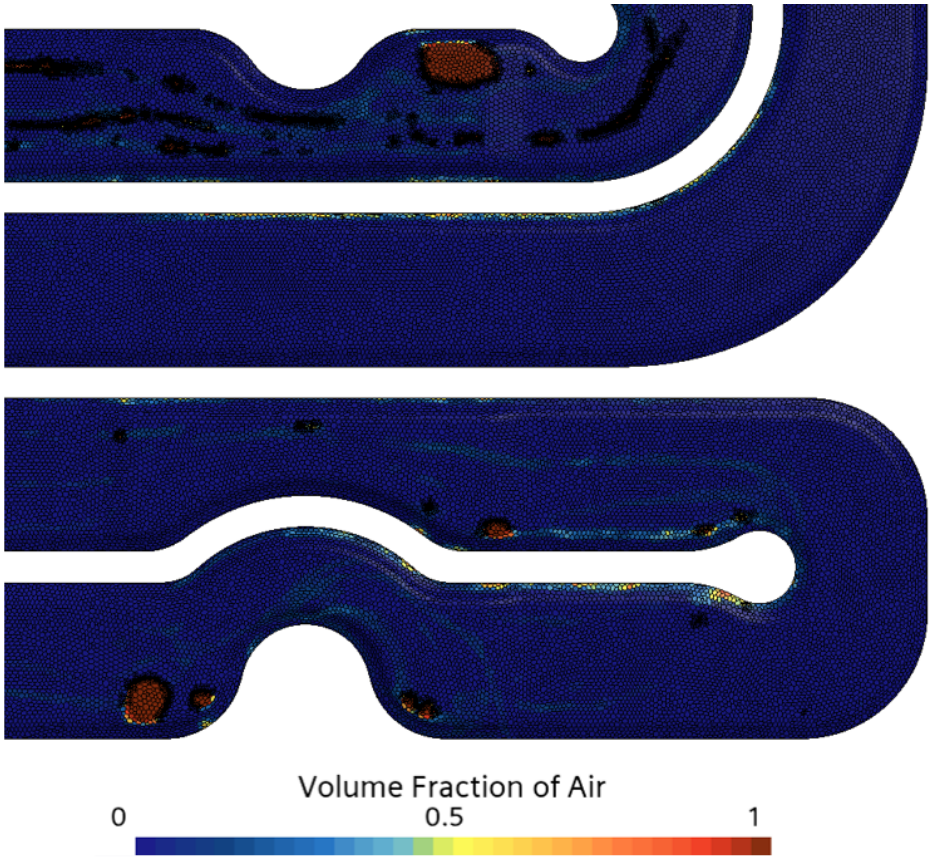

Figure 5.6: Top view of the cooling plate colored by air volume fraction during the purely transient phase, with visible mesh.

Given the enhanced sharpness of the interface achievable at an equivalent computational cost, it stands to reason that there are analogous applications where Adaptive Mesh Refinement (AMR) may serve as an optimal choice. This consideration is particularly relevant when acknowledging the dependency of computational efforts on the volume of air present within the system, as an increased number of cells arises from the presence of more bubbles and, consequently, a larger free surface area for refinement. Furthermore, the frequency of mesh adaptation significantly impacts computational efforts; in scenarios where bubbles exhibit relatively low dynamism, it is possible to employ a lower adaptation frequency (i.e., a greater number of time steps between successive adaptations), thereby substantially reducing computational demands.

In the context of this application, which concentrates on identifying problematic geometrical features during the design process, the findings of this study suggest that AMR does not confer a notable advantage, particularly when considering its associated drawbacks. The selection of an appropriate base mesh is critical to maintaining the stability of the simulation, as an excessively coarse base mesh can introduce challenges in resolving the primary phase flow, whereas an excessively fine mesh may result in undesirably high Courant numbers within the refined interface regions between faces.

5.3 Single Phase Simulation

In single-phase simulations, specific flow field characteristics may serve as predictors of areas where air bubble entrapment is probable. The identification of these regions is essential for comprehending the dynamics of bubble entrapment and provides an alternative method for efficiently identifying problematic areas in terms of time and cost when evaluating numerous design iterations. Moreover, any distinct indicator present in one-phase simulations could be employed as a parameter for assessment within the framework of multi-objective optimization of cooling plate designs, considering the presence of trapped air pockets in conjunction with other pertinent parameters, such as cooling power and pressure loss.

To analyze possible predictors of air entrapment areas, a single phase simulation has been performed on the same cooling plate with the same conditions but the total absence of air in the system.

This section discusses possible key indicators: velocity, vorticity, pressure, Q-criterion, and Lambda 2 criterion.

5.3.1 Velocity

Analyzing the velocity field provides insights into flow patterns that may lead to air entrapment. Low-velocity zones or recirculation areas can hinder bubble transport, causing them to become trapped.

Figure 5.7 shows a section of the cooling plate on the vertical direction z, highlighting streamlines in terms of linear integral convolution of velocity and colored by velocity magnitude. This type of visualization clearly highlights the recirculation areas, which result to be very strongly correlated with the areas where the bubbles get trapped in the multiphase simulations. Hence, this view is surely a great tool for quick evaluation of a cooling plate design in terms of degassing efficiency, allowing a clear visualization of features in the geometry that cause recirculation zones and therefore entrapment of air.

Figure 5.7: Linear Integral Convolution of velocity in a section in the vertical direction, colored by velocity magnitude.

Figure 5.8 shows the areas in the domain with low velocity magnitude colored by velocity magnitude, specifically lower than 5e−4 m/s and higher than 0 to exclude walls for correct visualization. The resulting low velocity zones correlate really closely with the areas where there is air presence in the multiphase simulations.

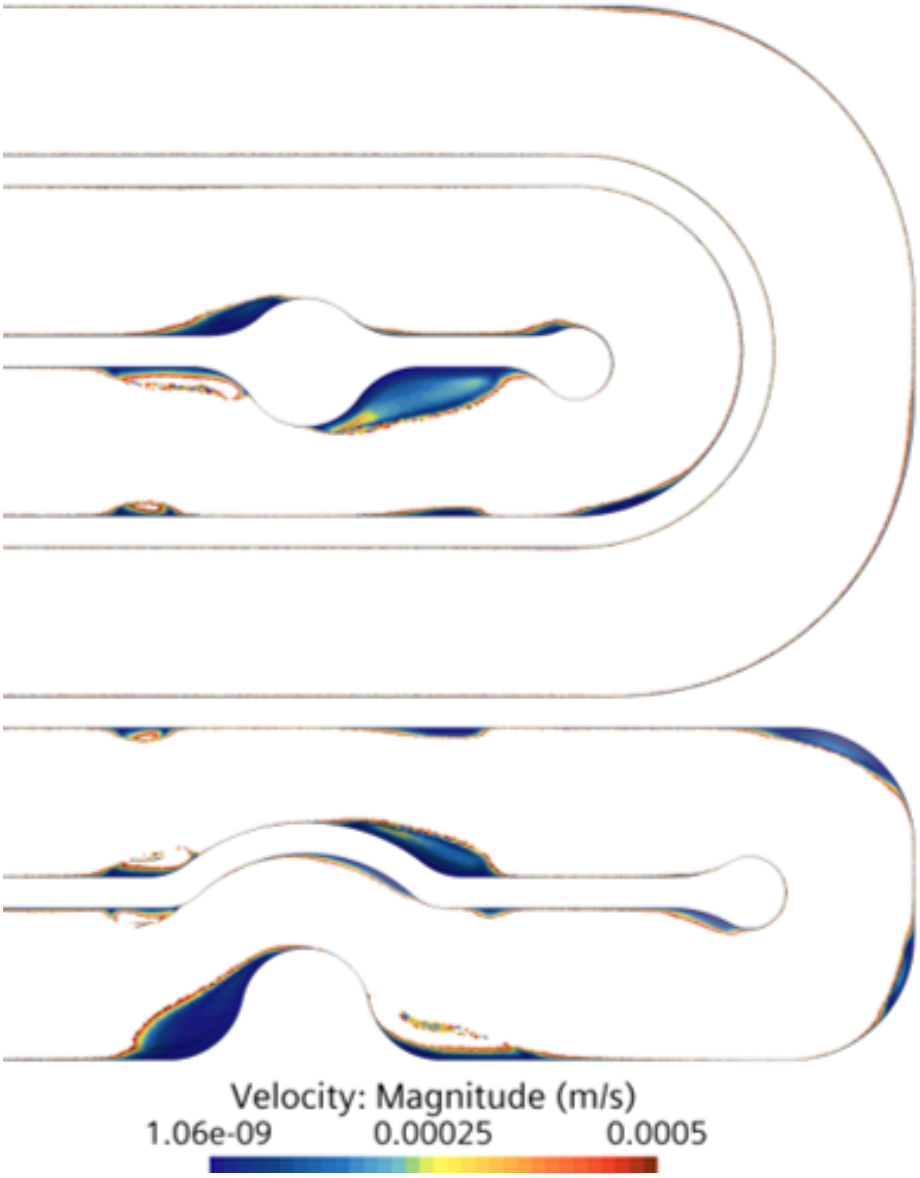

Figure 5.8: Surface of threshold of velocity magnitude in the domain colored by velocity magnitude.

Figure 5.9 reports the results of air volume fraction threshold in the multiphase simulation for better comparison with Figure 5.8

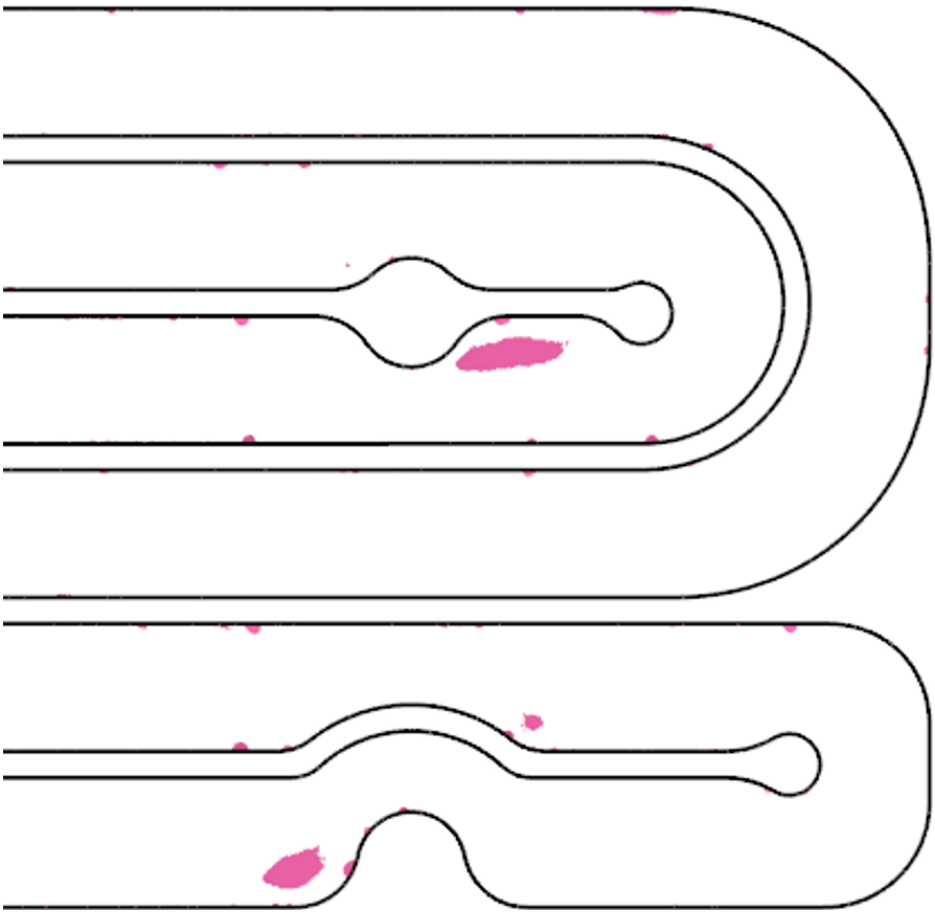

Figure 5.9: Surface of threshold of air volume fraction in the domain in the multiphase simulation.

In single-phase simulations, velocity serves as an effective indicator of problematic features in cooling plate geometries, in terms of air entrapment, thereby suggesting its potential as a parameter for consideration in the automated optimization of cooling plate designs for degassing. Additionally, low velocity areas are also detrimental for cooling power purposes in the plate.

In simpler geometries, it would be feasible to analyze different components of velocity; for instance, in a simple channel oriented along the x-direction, recirculation areas could be identified by low values of the x-component of velocity. This component could then be maximized to mitigate the presence of recirculation areas in various geometric configurations. However, in the cooling plate's typical layout, where flow directions vary across different passages, the velocity component changes sign with the geometry, rendering a single velocity component ineffective for identifying recirculation areas.

5.3.2 Vorticity

Vorticity, defined as the curl of the velocity field, quantifies the local rotation of fluid elements:

$$\boldsymbol{\omega} = \nabla \times \mathbf{u} \tag{5.1}$$

Monitoring vorticity helps identify such rotational regions.

Figure 5.10 shows a section of the cooling plate on the vertical direction z, colored by the magnitude of vorticity. The figure shows that in the areas where the air pockets form in the multiphase simulation, corresponds low values of vorticity magnitude. This is expected when considering the nature of the vorticity of being the curl of velocity, in recirculation zones the velocity magnitude is very low and therefore, the vorticity magnitude also results low. In the figure it is also notable the sudden change in vorticity magnitude where there is a sudden change in height in the channel.

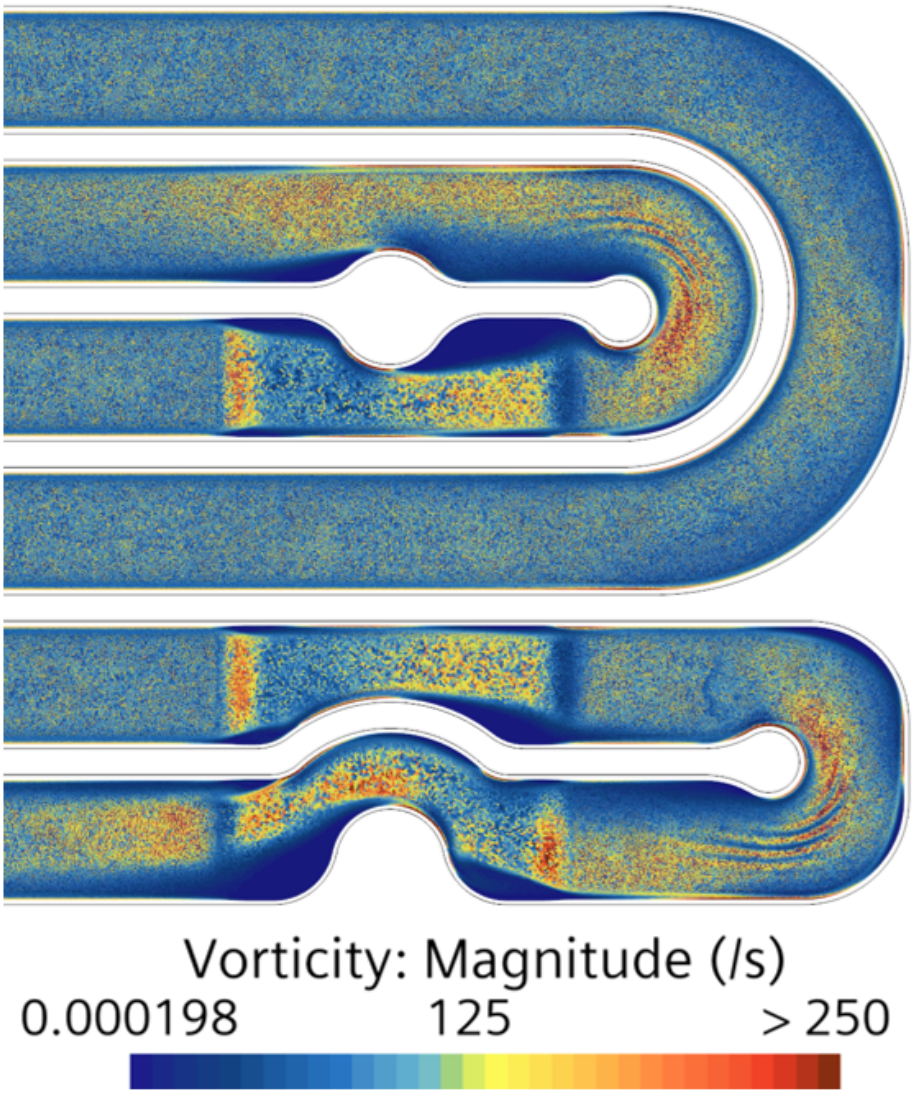

Figure 5.10: Section on the vertical direction of the cooling plate, colored by vorticity magnitude.

Figure 5.11 shows the surface of a threshold of the vorticity, illustrating the areas in the domain where this property is lower than 2. The figure shows a good correlation between the large low vorticity zones and the bubbles' entrapment areas, it is also visible that throughout the domain, the areas where in the flow there is lower rotation are also characterized by low vorticity.

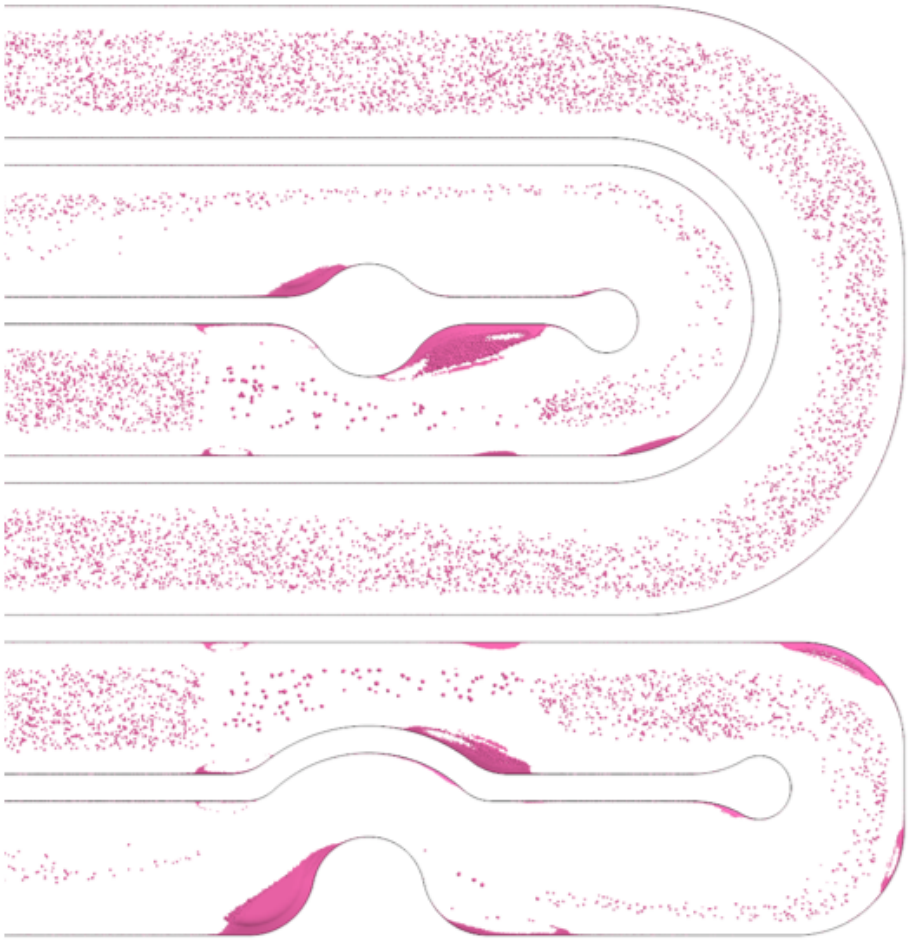

Figure 5.11: Threshold of low vorticity in the domain.

Considering these results, low vorticity magnitude areas can be a valuable indicator of bubble entrapment areas, but this appears to be mostly an effect of the dependency of vorticity magnitude to velocity magnitude. Furthermore, considering the high amount of areas where the vorticity magnitude is low because of low rotation of the flow, unrelated to the bubble entrapment, the vorticity appears to be an inferior indicator compared to velocity.

5.3.3 Pressure

Pressure gradients influence bubble dynamics significantly. Low-pressure regions can attract and trap air bubbles. Identifying these zones is essential for understanding bubble behavior.

Figure 5.12 shows a section of the cooling plate on the vertical direction z, colored by static pressure. From the figure, it is clear that the pressure loss along the main flow direction is dominant in comparison to the change in pressure, effectively not showing any clear position of trapped air coherent with the multiphase simulations.

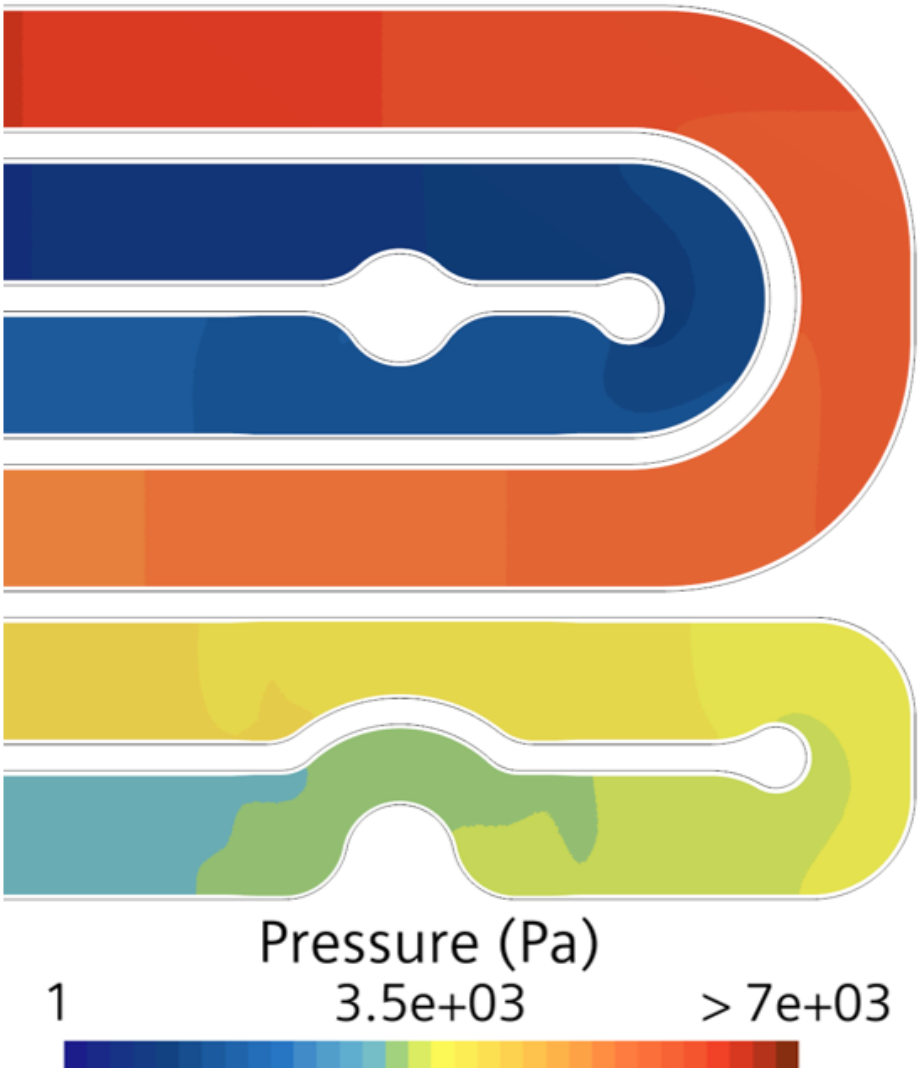

Figure 5.12: Section on the vertical direction of the cooling plate, colored by static pressure.

Considering the absence of clear correlation between the pressure changes and air entrapment zones in the multiphase simulations, the pressure is discarded as a possible indicator of problematic areas for degassing in single phase simulations.

5.3.4 Q-Criterion

The Q-criterion distinguishes rotational motion from shear by evaluating the balance between the rate of rotation and the rate of strain:

$$Q = \frac{1}{2}\left(\|\mathbf{\Omega}\|^2 - \|\mathbf{S}\|^2\right) \tag{5.2}$$

where $\mathbf{\Omega}$ is the antisymmetric part (vorticity tensor) and $\mathbf{S}$ is the symmetric part (strain rate tensor) of the velocity gradient tensor. Positive Q values indicate dominance of rotation, helping identify vortex cores.

Figure 5.13 shows a section of the cooling plate on the vertical direction z, colored by Q-criterion. The figure illustrates a poor correlation between the Q-Criterion values and

the bubble entrapment areas, it should be otherwise noted that the features guilty of trapping the bubbles created areas of high Q-criterion even if not in the exact locations where the bubbles would be trapped.

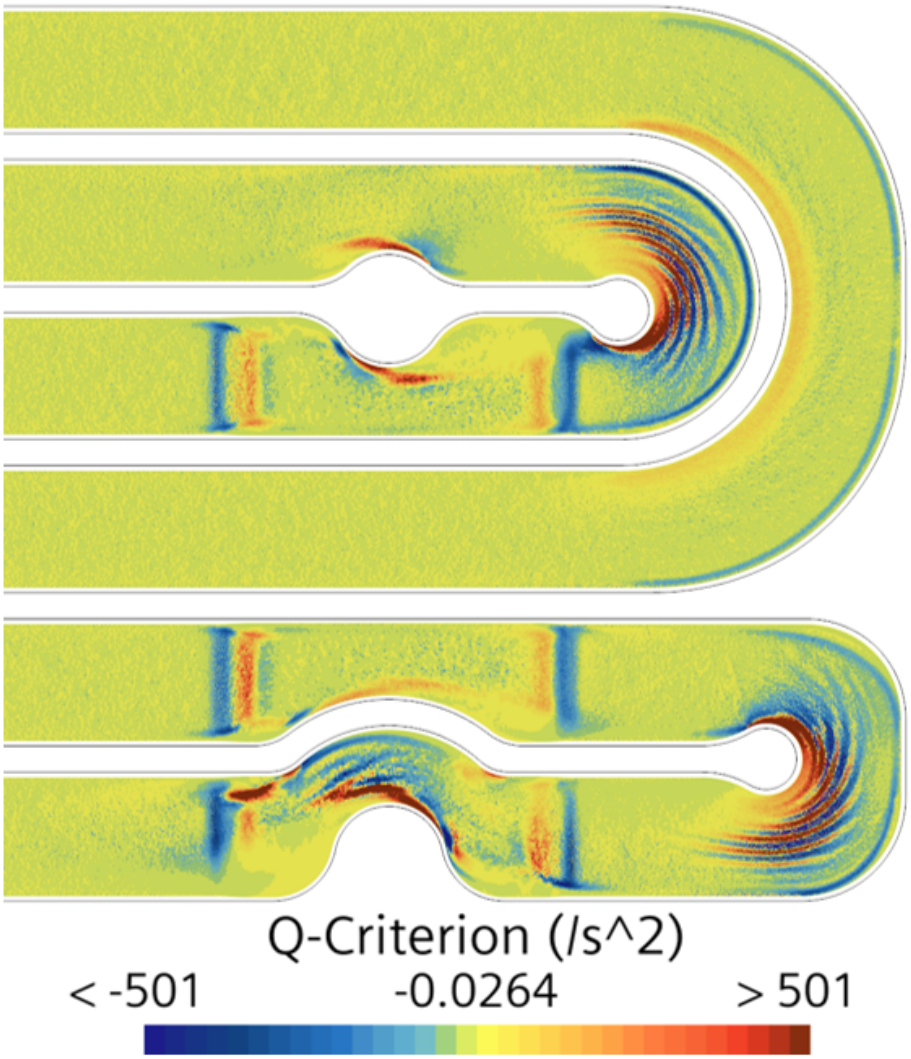

Figure 5.13: Section on the vertical direction of the cooling plate, colored by Q-criterion.

Considering these results, the Q-criterion is discarded as efficient indicator of bubble formation from one phase simulations.

5.3.5 Lambda 2 Criterion

The Lambda 2 criterion identifies vortex cores by analyzing the eigenvalues of the sum of squares of the symmetric and antisymmetric parts of the velocity gradient tensor. A region is considered a vortex core if the second-largest eigenvalue (λ_2) is negative:

$$\lambda_2 < 0 \tag{5.3}$$

This method effectively captures coherent vortical structures that may trap air bubbles.

Figure 5.13 shows a section of the cooling plate on the vertical direction z, colored by Lambda 2 criterion. The figure illustrates a moderate correlation between the bubble entrapment areas and the zones where the Lambda 2 criterion is close to 0.

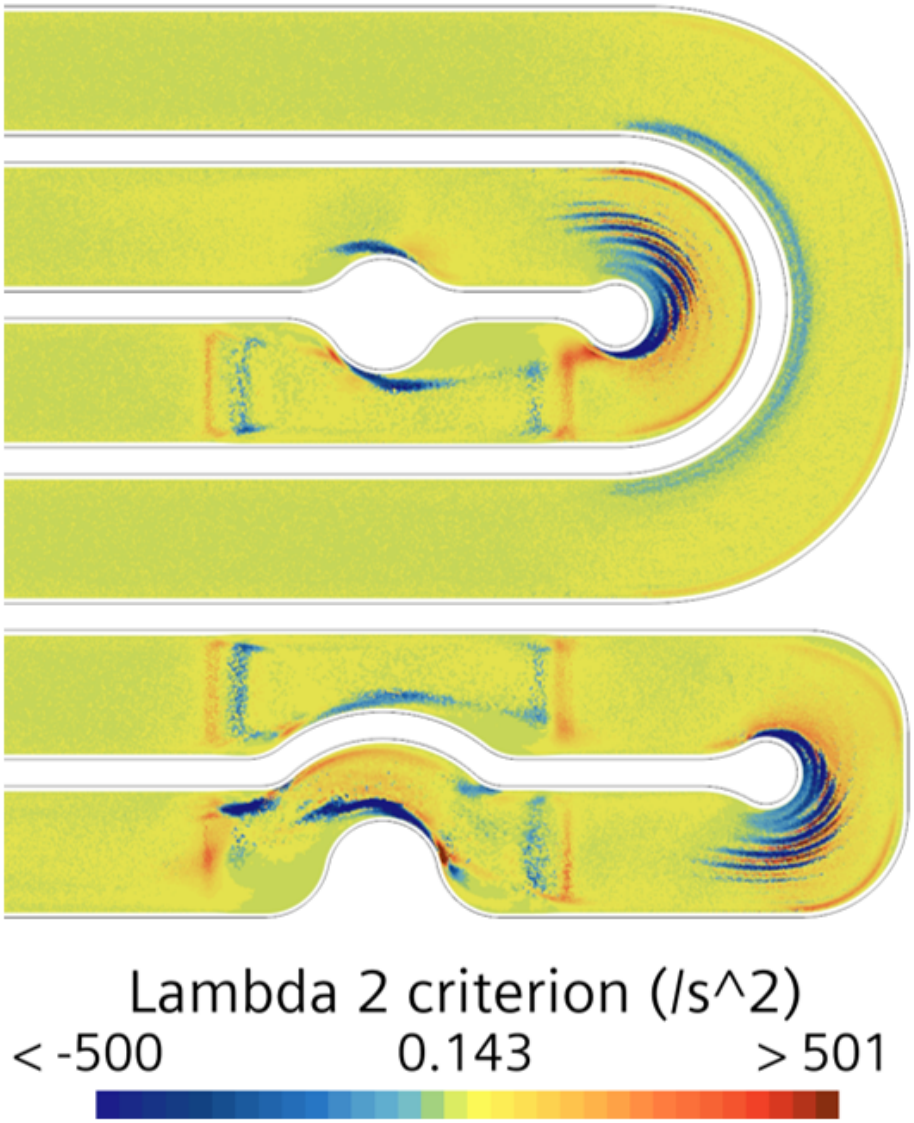

Figure 5.14: Section on the vertical direction of the cooling plate, colored by Lambda 2 criterion.

Considering these results, the Lambda 2 criterion might be a valid indicator of bubble entrapment in cooling plates, but appears to be a less clear indicator compared to velocity and vorticity.

5.3.6 Resulting Indicator Proposal

The results shown highlight the opportunity of making use of single phase simulation to have a preliminary assessment of entrapment areas in a cooling plate geometry in a reduced time compared to a multiphase simulation.

The evaluation of various potential indicators for identifying zones of air entrapment con-

cluded that velocity magnitude is the most appropriate indicator. Areas of low velocity are associated with recirculation zones where bubbles become trapped. Consequently, velocity magnitude can be utilized as a parameter within a multi-objective optimization framework when analyzing different geometrical configurations to mitigate air pockets present in the cooling plate.

It should be noted that it might be more difficult to recognize in a single phase simulation bubbles that become trapped due to buoyancy, as shown in an example in Figure 5.15, showing the volume fraction of air of an example section with a sudden increase in height of a channel followed by a sudden decrease in height. A bubble would remain trapped in this situation as a result of the difference in density between coolant and air, with the latter having a lower density and therefore, tending to be pushed on the top of the channels, requiring thus, a less low velocity for the bubble to be trapped compared to other directions not affected by buoyancy.

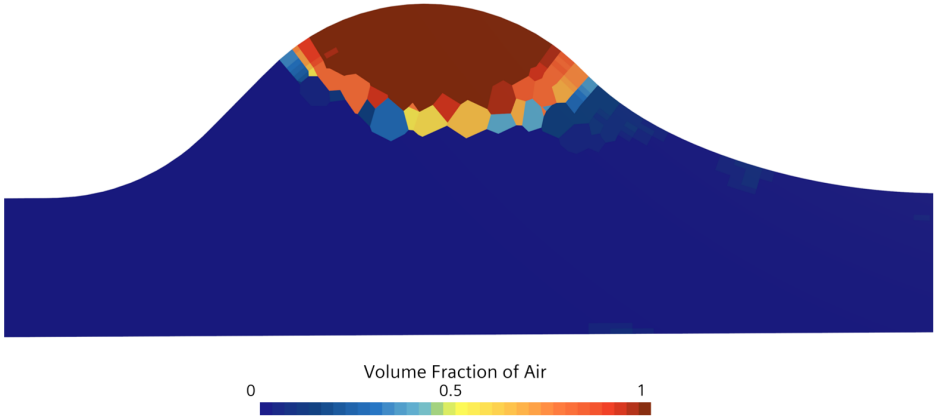

Figure 5.15: Example of sudden height increase followed by sudden height decrease, colored by volume fraction of air.

Bubbles in similar geometrical conditions to this one would not be captured by a too low threshold on velocity in a single phase simulation, but would still be visible by looking at recirculation areas in the domain, as see in Figure 5.16.

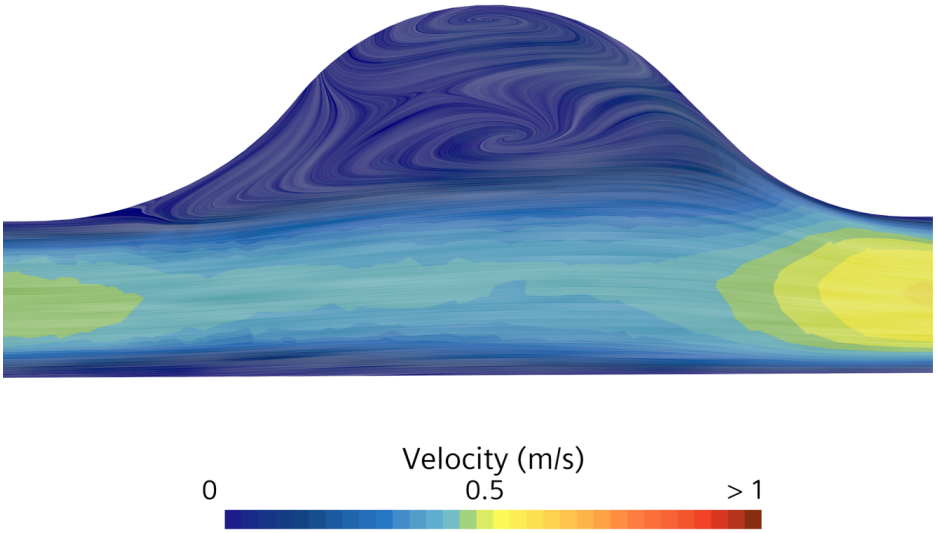

Figure 5.16: Example of sudden height increase followed by sudden height decrease, colored by velocity magnitude with LIC of velocity.

This situation can be compared to the use of a degas bottle mentioned in 1.3, which makes use of the density difference between the fluids to provide a prescribed location for the air to be trapped.

In consideration of avoidance of trapped air in the geometry, a sudden height increase followed by sudden height decrease should be avoided in cooling plate geometries, but this would not be recognized in a single phase simulation where effects of density differences would stay unknown.

Figure 5.17 shows a section of the cooling plate on the vertical direction z, highlighting streamlines in terms of linear integral convolution of velocity and colored by velocity magnitude in the single phase simulation, overlaid by the air surface in the multiphase simulation, resulting in strong correlation between the two simulations.

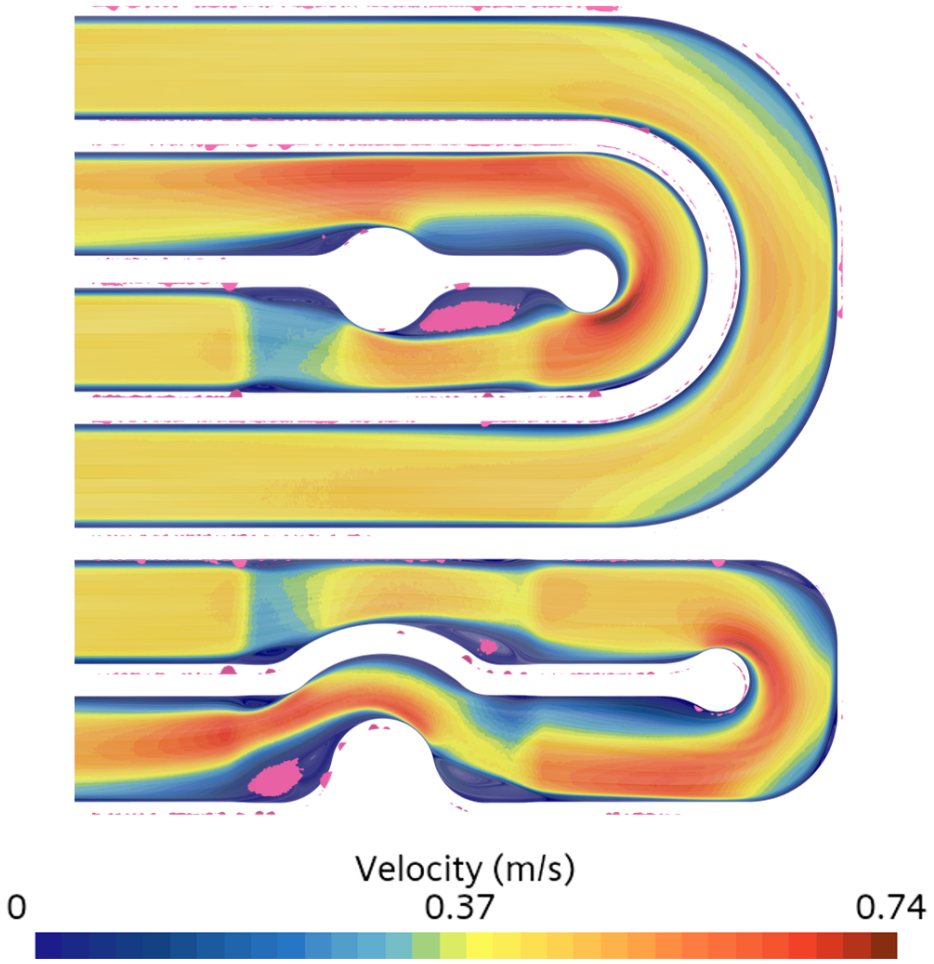

Figure 5.17: Linear Integral Convolution of velocity in a section in the vertical direction in the single-phase simulation, colored by velocity magnitude, overlaid by air surface in multiphase simulation.

The computational savings from performing single phase simulations are evident, in this work the same conditions of mesh, machine, time-step and solver options were used. Considering that a single-phase simulation is characterized by a much shorter fully transient phase of few seconds, it was possible to obtain significant results in about 1h effectively reducing the requirement of computational time of over 90%. It should be further considered that a coarser mesh would be acceptable for single-phase simulations, as well as a larger time step and the use of a steady simulation making use of the RANS turbulence modeling approach; these could significantly further reduce the computational time required for the single phase simulations.

Chapter 6

Analysis of Alternative Geometries

This chapter presents the degassing analysis on two other different geometries, where one is an improved prototype to the main cooling plate studied in this work, and the other is a completely different concept of design.

6.1 Improved Design

This section presents the results of the analysis of identification of entrapment of air pocket in a cooling plate geometry similar to the main one analyzed in this study but specifically improved for degassing.

Specifically, in this design, the curves are more slender to reduce the impact of sudden obstacles for the flow that would cause recirculation zones.

Figure 6.1 shows a top view of the cooling plate colored by air volume fraction for the improved geometry. The figure highlights the absence of air in this design at the end of the degassing process, showcasing the significant impact of specific geometrical features on the entrapment of air in cooling plates.

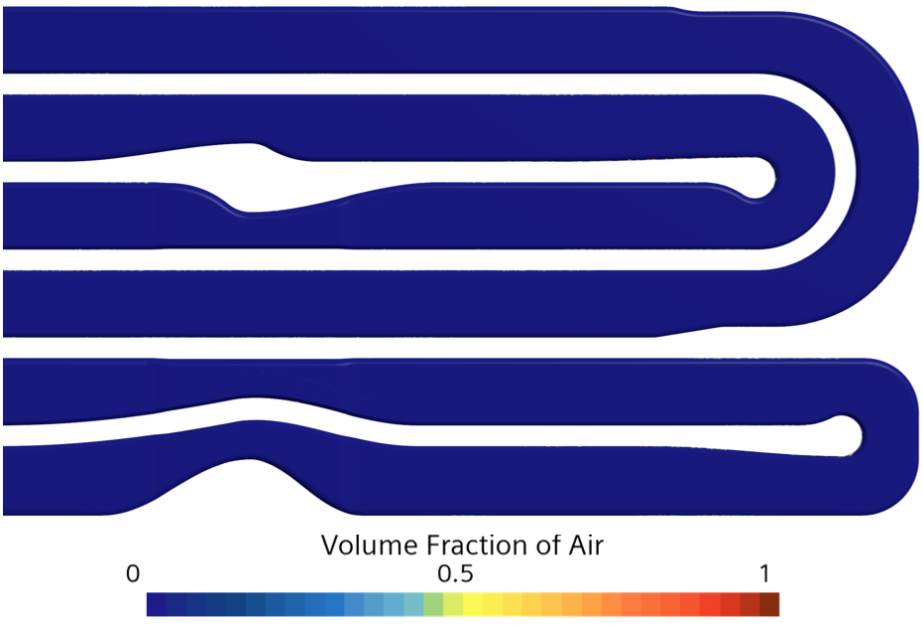

Figure 6.1: Top view of the cooling plate colored by air volume fraction.

Figure 6.2 shows a section of the cooling plate on the vertical direction z, highlighting streamlines, in terms of linear integral convolution of velocity and colored by velocity magnitude. The figure highlights the reduced dimensions of recirculation areas in all the features that previously presented them.

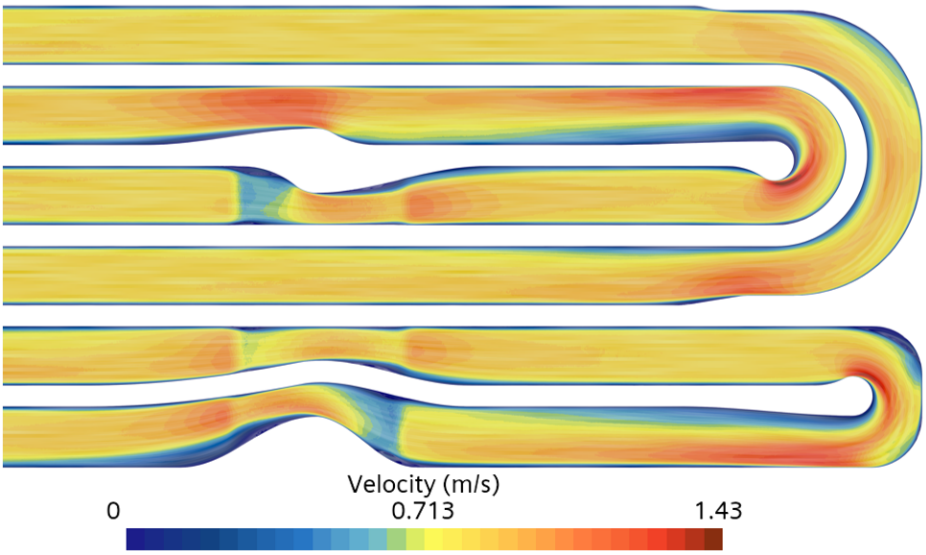

Figure 6.2: Linear Integral Convolution of velocity on a section on the vertical direction of the cooling plate colored by velocity magnitude.

It should be noted that this geometry is not completely free of air pockets in its entirety, as in one area not shown here for confidentiality, a small bubble is trapped, highlighting the room for further improvement in the geometry. The resulting GLR in this component is 5.366e−7, showcasing a reduction of 70% from the first prototype.

6.2 Different Concept

In this section, the results of the analysis of identification of entrapment of air pocket in a different concept of cooling plate geometry are presented, showcasing the functionality of the simulation model different type of geometries.

The figure present a small part of the analyzed cooling plate. the entirety of the domain is not shown for confidentiality purposes. The simulation is performed with analogous conditions of time step and boundary conditions to the main simulations in this study.

Figure 6.3 shows a top view of the cooling plate colored by air volume fraction for a different cooling plate concept, with arrows indicating the flow direction. The figure illustrates few small bubbles on the top of the cooling plate, entirely along the borders of the structure and specifically along some of the corners.

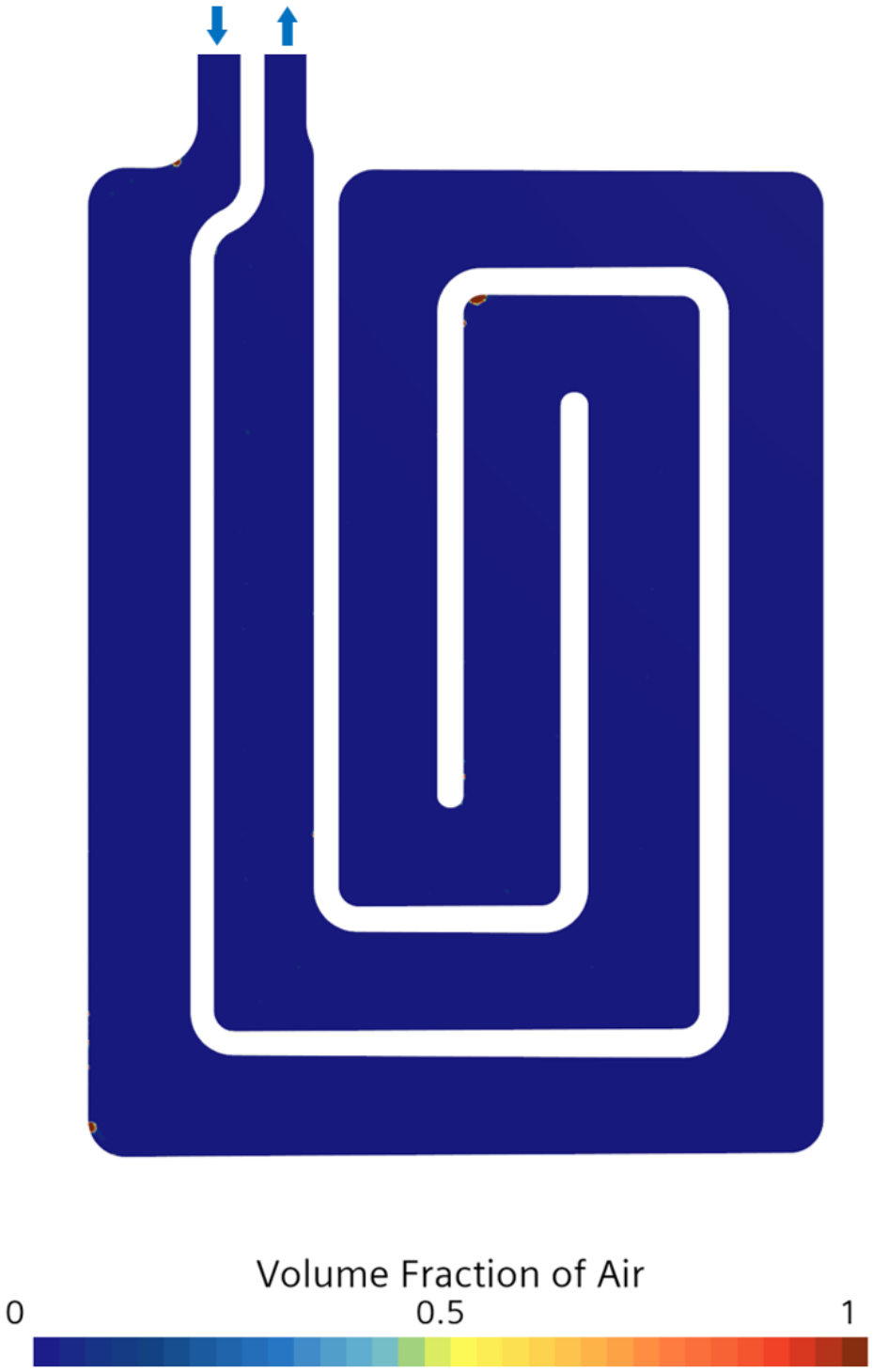

Figure 6.3: Top view of the cooling plate, colored by air volume fraction.

Figure 6.4 shows the areas of air presence in the domain through a threshold in air volume fraction. This figure further highlights the locations of entrapment of air in this cooling plate.

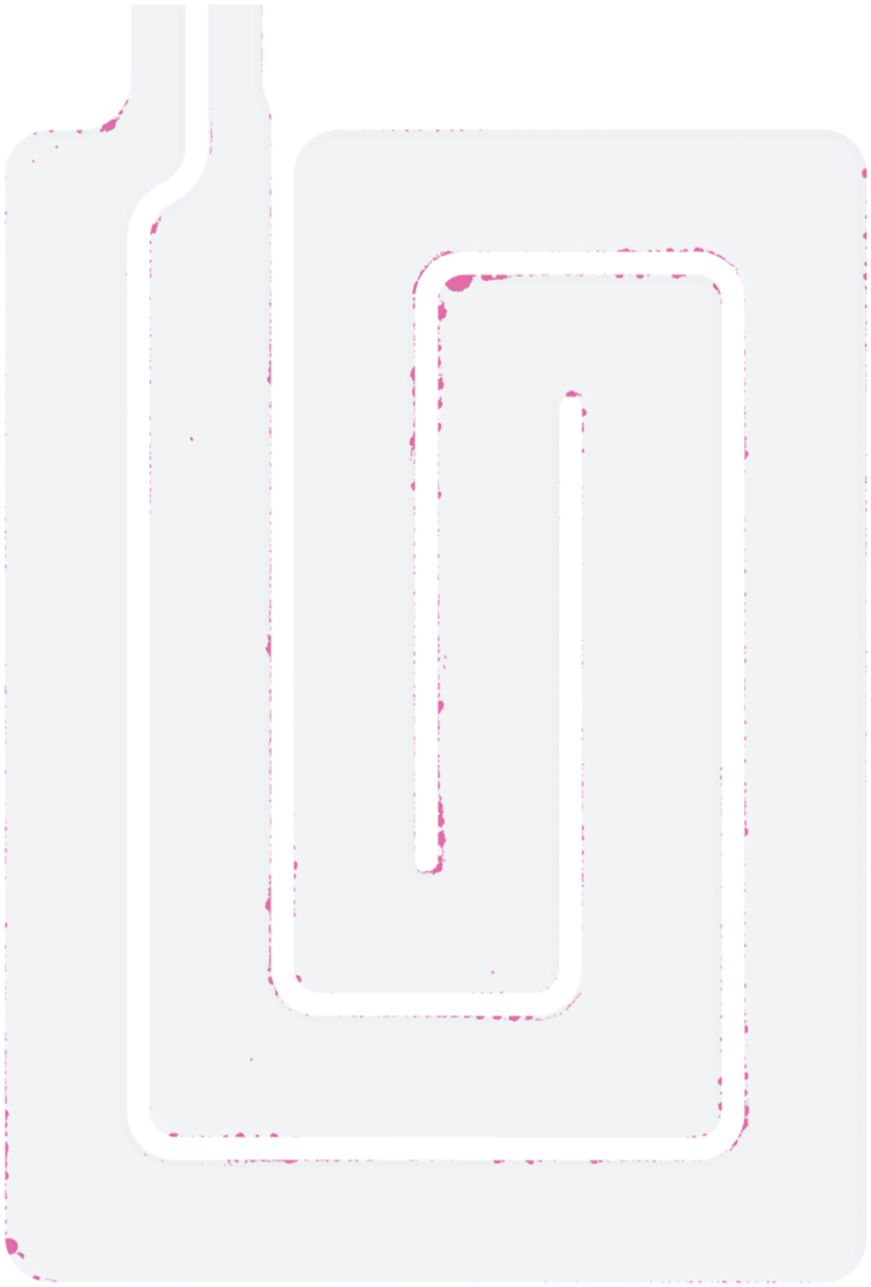

Figure 6.4: Surface of air presence in the domain through air volume fraction threshold.

To further prove that one phase simulations can be a good indicator of features that would cause air pockets, a single phase simulation has been performed on this geometry to analyze if the proposed indicator, velocity magnitude, is a valid tool for design assessment in a different geometry.

Figure 6.5 shows a section of the cooling plate on the vertical direction z, highlighting streamlines, in terms of linear integral convolution of velocity and colored by velocity magnitude in the single phase simulation. The figure shows very few clear recirculation areas of very small entity, specifically close to the inlet to this specific passage, where the flow abruptly changes direction. It is also visible the presence of low velocity zones in all

the corners of the structure.

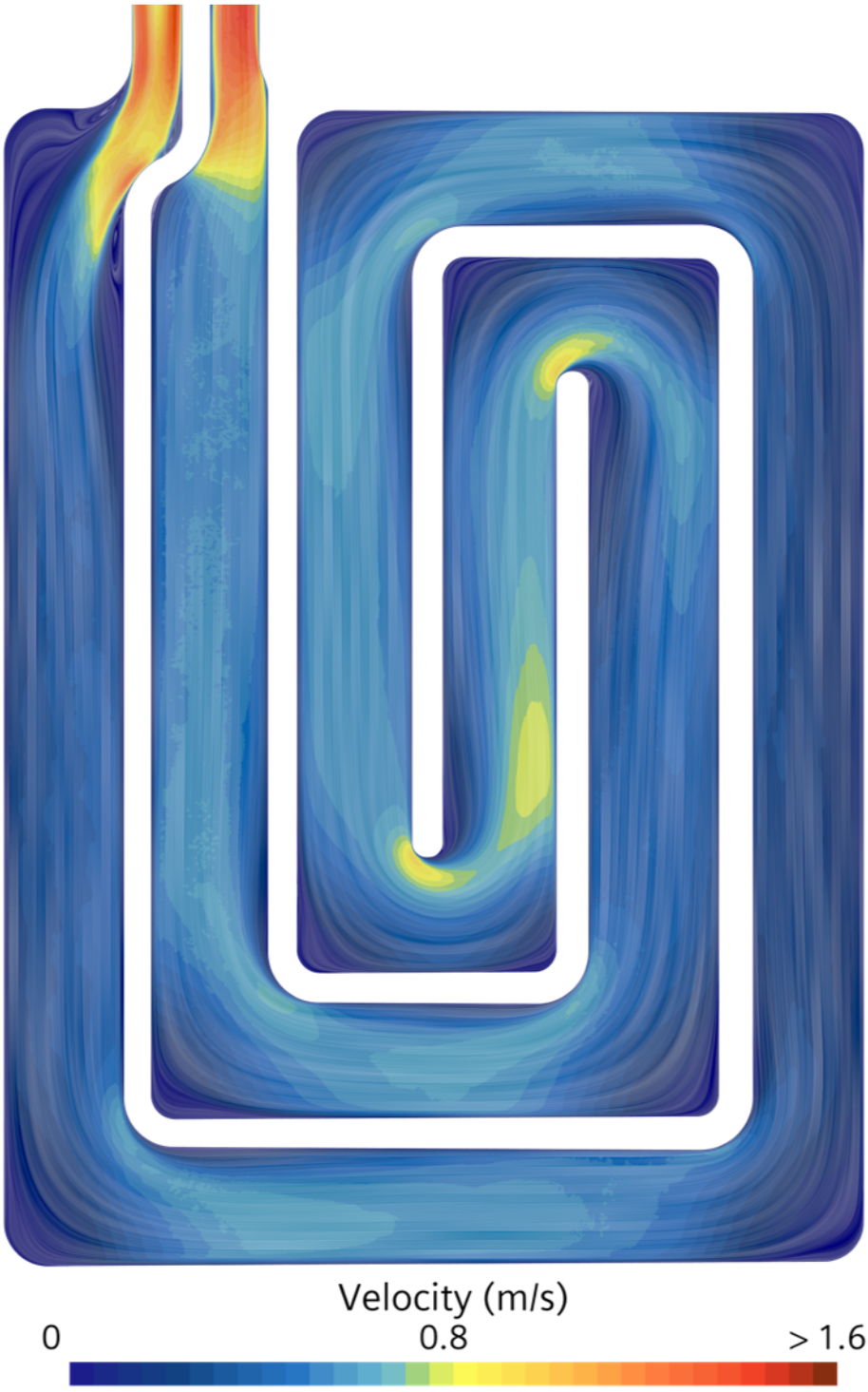

Figure 6.5: Linear Integral Convolution of velocity on a section on the vertical direction of the cooling plate, colored by velocity magnitude.

Figure 6.6 shows the areas in the domain with low velocity magnitude colored by velocity magnitude, specifically lower than $5e4$ m/s and higher than 0 m/s to exclude walls for correct visualization. The figure highlighted areas of low velocity strongly correlate with

the areas occupied by air in the multiphase simulation, further suggesting that the velocity magnitude can be a good indicator of air entrapment from single phase simulations.

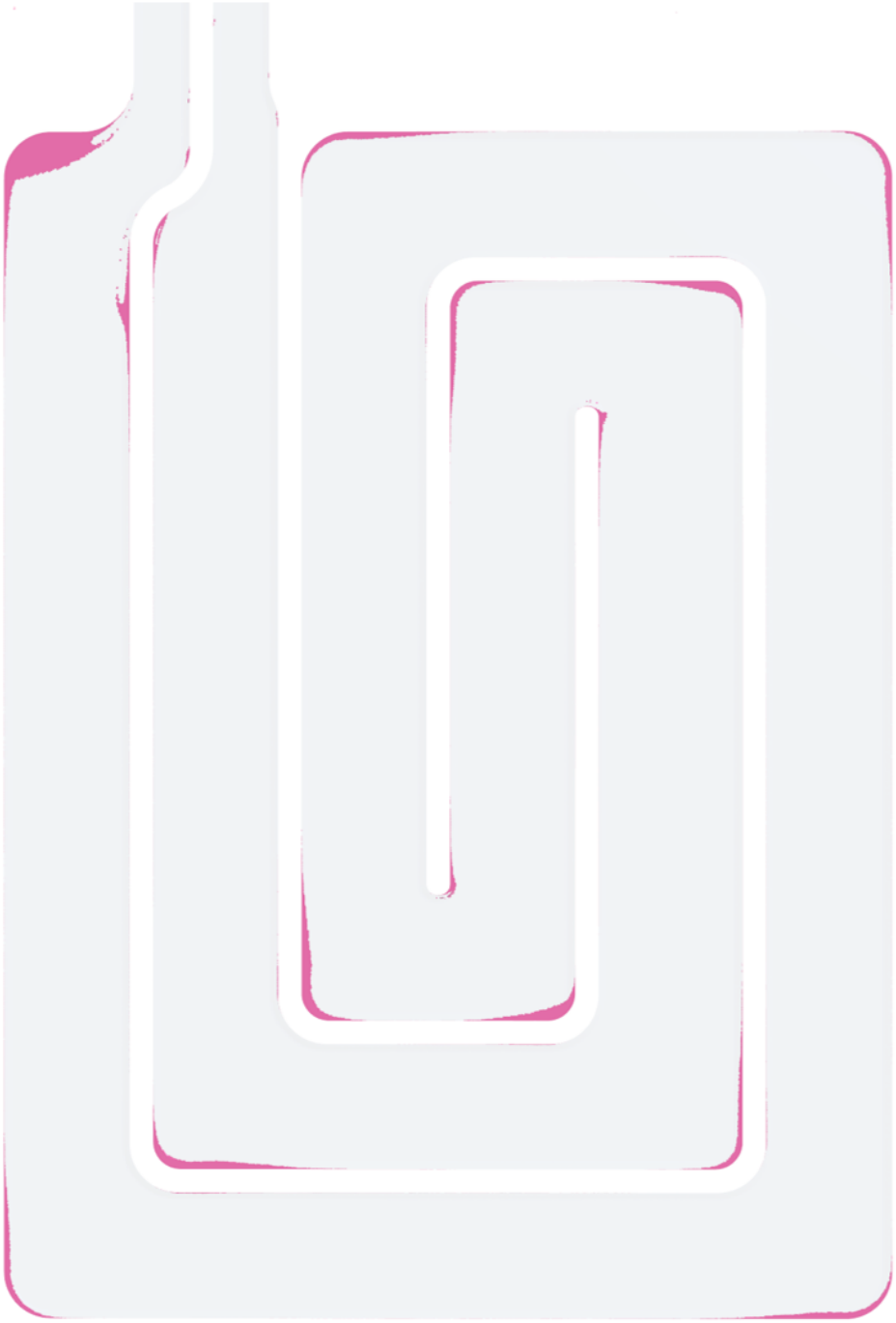

Figure 6.6: Surface of threshold of velocity magnitude in the domain.

Looking at the results of this analysis, for this portion of the cooling plate, a proposed design modification could be to increase the fillet radius in the corners to ensure smaller areas of low velocity in the domain. It should always be taken in consideration the high amount of constraints in these type of applications, given from the presence of the other components in the EVs, which limit the design freedom, as well as manufacturing constraints.

Chapter 7

Discussion

This chapter critically examines the key modeling decisions and results of this study, offering insights into their implications and limitations.

The experimental validation was constrained by the use of a single transparent prototype, which could not be reused due to physical damage. Consequently, the experimental dataset could not be statistically expanded, limiting its ability to capture broader variability. Additionally, factors such as low image resolution, light reflections, and camera vibrations introduced measurement noise. Despite these limitations, the validation showed remarkable agreement with simulation results in terms of bubble location and size, thereby confirming the robustness of the model for design evaluation purposes.

The study evaluated three turbulence models—URANS, LES, and DES—on an identical, finely resolved mesh. The predicted air entrapment locations were consistent across all models, and surprisingly, so was the computational time required. This suggests that the dominant source of computational cost and model sensitivity stemmed from interface tracking via the VOF method rather than turbulence resolution. The LES model, supported by resolved turbulence fraction analysis (with $f_{\text{resolved}} \approx 0.82$), confirmed the suitability of the selected mesh resolution.

Adaptive Mesh Refinement (AMR) was tested as a means to reduce computational cost while maintaining accuracy. The implementation of AMR demonstrated localized improvements in resolving complex flow structures near the interface without significantly increasing overall cell count. However, the overhead introduced by dynamic grid updates marginally reduced the efficiency gains expected. Nevertheless, AMR remains a promising direction, especially for applications that require a sharp interface solution.

Among the single-phase flow indicators evaluated, the velocity magnitude emerged as the most practical and reliable for identifying potential air entrapment regions. While indicators like vorticity, pressure gradient, Q-criterion, and λ_2 showed limited or indirect correlation, velocity-based metrics provided a simple and computationally inexpensive method. This has significant implications for early-stage geometry assessment and optimization, enabling rapid iteration without full multiphase simulations.

The improved design of the main cooling plate demonstrated a clear reduction in air entrapment, underlining the effectiveness of design modifications. Additionally, the analysis of a completely different geometry confirmed the generalizability of the velocity indicator and underscored the air entrapment conditions posed by stagnation zones, especially in corner regions.

The multiphase CFD simulations were computationally intensive due to the fine mesh, small time steps, and interface tracking requirements. Despite exploring various model-

ing strategies, the primary computational bottleneck remained the VOF solver. The use of Java macros to initialize air bubble distributions and automate boundary conditions helped streamline the workflow and reduced runtime significantly.

The initialization of air pockets played a role in the final simulation outcomes, particularly near the inlet, where the results showed sensitivity to air fraction. However, a sensitivity study confirmed that most air entrapment locations were not significantly affected by variations in initial air distribution, suggesting that the final degassing pattern is primarily geometry-driven rather than strongly initial-condition-dependent. This justifies the use of a practical initialization strategy for simulating late-stage filling behavior.

Chapter 8

Conclusion

This thesis investigated the degassing behavior in electric vehicle (EV) battery cooling plates through numerical modeling, with a focus on identifying and mitigating air entrapment using Computational Fluid Dynamics (CFD) methods. The study was conducted in collaboration with Volvo Cars, and addressed the challenge of residual air pockets that impair heat transfer efficiency and compromise battery system reliability.

A Volume of Fluid (VOF) multiphase approach was implemented, with an emphasis on resolving gas-liquid interactions during the degassing phase. Three turbulence models: Unsteady Reynolds-Averaged Navier-Stokes (URANS), Large Eddy Simulation (LES), and Detached Eddy Simulation (DES) were tested on a high-resolution mesh of 40 million cells. All turbulence models delivered comparable results in terms of air entrapment prediction, ans suprisingly in terms of computational time, suggesting that the multiphase solver and interface tracking dominated computational costs and outcome fidelity.

The simulation results demonstrated strong agreement with experimental observations, validated through bubble size and position comparisons using image processing. The GLR-based termination criterion proved effective in identifying the quasi-steady end state of the degassing process. Quantitative validation showed a deviation of less than 0.001% in total air volume between simulation and experiment, reinforcing the model's predictive capability, even though, discrepancies in the model and simulations results were still present.

Furthermore, the study assessed the predictive potential of single-phase indicators for identifying high-risk air entrapment zones. Among the evaluated indicators: velocity magnitude, vorticity, pressure gradient, Q-criterion, and λ_2 criterion; the velocity magnitude proved to be the most reliable. It strongly correlated with bubble entrapment locations observed in multiphase simulations, making it a practical tool for preliminary design assessment without incurring the high computational cost of full multiphase simulations, reducing the computational time of more than 90%.

The analysis was extended to two additional geometries: an improved version of the main cooling plate and a different concept of design. The improved geometry showed near-complete elimination of air pockets, validating the design modifications and the use of the proposed single-phase indicator. The different concept design confirmed the model's adaptability to different geometrical configurations, and highlighted how low-velocity regions near corners are consistently problematic.

In conclusion, the thesis successfully addressed the research objective: to develop and validate a reliable numerical framework for the prediction and analysis of degassing in EV cooling plates. The validated CFD model, supported by experimental data and enhanced by a proposed single-phase indicator, provides a strong foundation for future optimization and innovation in EV battery thermal management systems.

Chapter 9

Future Work

While the present study provides a validated and computationally efficient framework for simulating degassing in EV cooling plates, several avenues remain open for further exploration.

To improve the confidence in model predictions, additional experimental datasets are required. Future experiments should employ higher-resolution imaging systems, optimized lighting conditions, and vibration-isolated mounting to reduce measurement uncertainty. Additionally, using multiple prototype geometries and capturing more statistical repetitions would support a more robust validation of the simulation framework.

The initial condition was approximated using a custom air-bubble initialization strategy. While effective, this bypasses the actual filling dynamics. Simulating the complete filling process would provide a more comprehensive understanding of the physical time required to perform the operations of filling and degassing.

Given the high computational cost of full multiphase simulations, a promising direction lies in the development of surrogate models. These could include machine learning techniques trained on high-fidelity simulation data to predict bubble entrapment regions from geometry and flow features. This would further accelerate design iterations and integrate well into digital twin frameworks.

While this thesis focused on high-flow degassing, future work could explore other strategies, including the impact of channel inclination, passive degassing chamber placement, or the use of hydrophobic/hydrophilic coatings. Understanding how such design features interact with the flow field could open new avenues for passive air removal optimization.

The integration of electrochemical performance models or structural stress simulations with the degassing framework would provide a holistic understanding of how residual air pockets influence battery performance and safety. In particular, coupling degassing results with cell degradation models could link air entrapment directly to long-term battery reliability.

The implementation of acoustic analogies could provide more information about the disturbing noise generated from the bubbles in the cooling plates.

The validated CFD tool could be integrated into automated multi-objective optimization loops, using algorithms like genetic optimization or Bayesian optimization. Coupled with single-phase indicators, this would enable rapid screening of candidate geometries and support automated design workflows, for multiple factors such as cooling power and pressure loss.

In conclusion, while this thesis provides a solid foundation for degassing simulation and analysis, its full potential lies in future extensions that further improve physical accuracy, computational efficiency, and integration with design and validation pipelines.

Bibliography

Brackbill, J., Kothe, D., and Zemach, C. (1992). A continuum method for modeling surface tension. *Journal of Computational Physics*, 100(2):335–354.

Brahmasani, L., Solomon, S., and Khan, P. (2014). A secondary de-aeration circuit for an engine cooling system with atmospheric recovery bottle to improve de-aeration.

Celik, I. B., Ghia, U., Roache, P. J., Freitas, C. J., Coleman, H., and Raad, P. E. (2008). Procedure for Estimation and Reporting of Uncertainty Due to Discretization in CFD Applications. *Journal of Fluids Engineering*, 130(7):078001.

Chen, H., Lu, Z., Cheng, Y., Drioli, E., Wang, Z., Zhang, F., and Cui, Z. (2023). Development and emerging application of membrane degassing technology. *Advanced Membranes*, 3:100076.

Deng, Y., Feng, C., E, J., Zhu, H., Chen, J., Wen, M., and Yin, H. (2018). Effects of different coolants and cooling strategies on the cooling performance of the power lithium ion battery system: A review. *Applied Thermal Engineering*, 142:10–29.

Deng, Y., Li, B., and Li, Z. (2022). Quantification of motion characteristics of vertically ascending bubbles in nacl solution via image processing. *International Journal of Chemical Reactor Engineering*, 21.

Eskin, D. (2015). *Ultrasonic degassing of liquids*, pages 611–631.

European Council (2022). Fit for 55: why the eu is toughening co2 emission standards for cars and vans. https://www.consilium.europa.eu/en/infographics/fit-for-55-emissions-cars-and-vans/.

Fujimoto, H., Shiotani, Y., Tong, A., Hama, T., and Takuda, H. (2007). Three-dimensional numerical analysis of the deformation behavior of droplets impinging onto a solid substrate. *International Journal of Multiphase Flow*, 33:317–332.

Gu, J., Kim, H.-K., and Jang, S. (2025). Study of cooling performance of liquid-cooled ev battery module according to the tim compression ratio. *International Journal of Automotive Technology*, 26(2):359–373.

Han, B., Sun, Z., Zhu, J., Fu, Z., Kong, X., and Barghi, S. (2022). Bubble dynamics in 2-d gas–solid fluidized bed with geldart a or geldart b particles by image processing method. *The Canadian Journal of Chemical Engineering*, 100(12):3588–3599.

Hirt, C. and Nichols, B. (1981). Volume of fluid (vof) method for the dynamics of free boundaries. *Journal of Computational Physics*, 39(1):201–225.

Jensen, A. L., Sørensen, H., Rosendahl, L., and and, P. U. T. (2018). Characterisation of textile shape and position upstream of a wastewater pump under different part load conditions. *Urban Water Journal*, 15(2):132–137.

Lesieur, M. and Metais, O. (1996). New trends in large-eddy simulations of turbulence. *Annual review of fluid mechanics*, 28(1):45–82.

lin Yan, S., bao Zhang, X., and hong Luo, Z. (2025). Adaptive mesh refinement for vof modeling gas-liquid two-phase flow: A summary of some algorithms and applications. *Chemical Engineering Science*, 306:121291.

Liu, H., Wei, Z., He, W., and Zhao, J. (2017). Thermal issues about li-ion batteries and recent progress in battery thermal management systems: A review. *Energy Conversion and Management*, 150:304–330.

Luo, M., Lin, X., Feng, J., Ling, Z., Zhang, Z., and Fang, X. (2023). Fast self-preheating system and energy conversion model for lithium-ion batteries under low-temperature conditions. *Journal of Power Sources*, 565:232897.

Manceau, R. (2002). Elliptic blending model: A new near-wall reynolds-stress turbulence closure. *Physics of Fluids, 14 (2), 2002 ; doi:10.1063/1.1432693*, 14.

Mikko, M., Taivassalo, V., and Kallio, S. (1996). On the mixture model for multiphase flow. *VTT Publications*, 288.

Mulbah, C., Kang, C., Mao, N., Zhang, W., Shaikh, A. R., and Teng, S. (2022). A review of vof methods for simulating bubble dynamics. *Progress in Nuclear Energy*, 154:104478.

Muzaferija, S. and Peri'c, M. (1999). *Computation of free-surface flows using interface-tracking and interface-capturing methods.*, pages 59–100.

NASA (2021). Examining spatial (grid) convergence. `https://www.grc.nasa.gov/www/wind/valid/tutorial/spatconv.html`.

Neugebauer, M., Żebrowski, A., and Esmer, O. (2022). Cumulative emissions of co2 for electric and combustion cars: A case study on specific models. *Energies*, 15(7).

Nicoud, F. and Ducros, F. (1999). Subgrid-scale stress modelling based on the square of the velocity gradient tensor. *Flow, turbulence and combustion*, 62(3):183–200.

Nilsson, E. J. K. and Ahlberg Tidblad, A. (2024). Gas emissions from lithium-ion batteries: A review of experimental results and methodologies. *Batteries*, 10(12).

Norouzi, H. R., Zarghami, R., Sotudeh-Gharebagh, R., and Mostoufi, N. (2016). *Coupled CFD-DEM modeling: formulation, implementation and application to multiphase flows*. John Wiley & Sons.

Oh, K.-Y., Siegel, J. B., Secondo, L., Kim, S. U., Samad, N. A., Qin, J., Anderson, D., Garikipati, K., Knobloch, A., Epureanu, B. I., Monroe, C. W., and Stefanopoulou, A. (2014). Rate dependence of swelling in lithium-ion cells. *Journal of Power Sources*, 267:197–202.

Revell, A., Benhamadouche, S., Craft, T., and Laurence, D. (2006). A stress–strain lag eddy viscosity model for unsteady mean flow. *International Journal of Heat and Fluid Flow*, 27(5):821–830. Special issue of the 6th International Symposium on Engineering Turbulence Modelling and Measurements – ETMM6.

Shirsikar, A., Khatik, P., and nagaraja, C. (2021). Performance evaluation of degas tank.

Spalart, P., Jou, W.-H., Strelets, M., and Allmaras, S. (1997). Comments on the feasibility of les for wings, and on a hybrid rans/les approach.

Sun, H. and Dixon, R. (2014). Development of cooling strategy for an air cooled lithium-ion battery pack. *Journal of Power Sources*, 272:404–414.

Sun, J., Li, J., Zhou, T., Yang, K., Wei, S., Tang, N., Dang, N., Li, H., Qiu, X., and Chen, L. (2016). Toxicity, a serious concern of thermal runaway from commercial li-ion battery. *Nano Energy*, 27:313–319.

Tao, M., Slike, J., Bhagat, M., Srinivasan, C., Zhang, Y., and Motin, A. (2022). Numerical modelling of coolant filling and de-aeration in a battery electric vehicle cooling system. *SAE International Journal of Advances and Current Practices in Mobility*, 5.

Ubale, D. and Ubale, P. (2022). A critical review on recent developments in battery thermal management system of electric vehicles. *Materials Today: Proceedings*, 68:2613–2621. 4th International Conference on Advances in Mechanical Engineering.

Volvo Cars (2022). Powertrain - battery electric vehicle. https://www.media.volvocars.com/global/en-gb/media/photos/325196/powertrain.

Wang, X., Xie, Y., Day, R., Wu, H., Hu, Z., Zhu, J., and Wen, D. (2018). Performance analysis of a novel thermal management system with composite phase change material for a lithium-ion battery pack. *Energy*, 156:154–168.

Yan, J., Wang, Q., Li, K., and Sun, J. (2016). Numerical study on the thermal performance of a composite board in battery thermal management system. *Applied Thermal Engineering*, 106.

Yao, M., Gan, Y., Liang, J., Dong, D., Ma, L., Liu, J., Luo, Q., and Li, Y. (2021). Performance simulation of a heat pipe and refrigerant-based lithium-ion battery thermal management system coupled with electric vehicle air-conditioning. *Applied Thermal Engineering*, 191:116878.

Zhou, W., Miwa, S., Tsujimura, R., Nguyen, T.-B., Okawa, T., and Okamoto, K. (2023). Bubble feature extraction in subcooled flow boiling using ai-based object detection and tracking techniques. Bubble detection;Condensation bubble;Engineering applications;Features extraction;Heat transfer systems;Object detection and tracking;Scientific engineering;Scientific investigation;Subcooled flow boiling;Tracking techniques;.